國立臺灣大學工學院土木工程學系

博士論文

Department of Civil Engineering

College of Engineering

National Taiwan University

Doctoral Dissertation

鋼纖維混凝土修正壓力場及軟化壓拉桿模型發展研究

Development of Modified Compression Field Theory (MCFT) and Softened Strut-and-Tie (SST) Model for Steel Fiber Reinforced Concrete (SFRC)

汪亞施

Suyash Kishor Wagh

指導教授：廖文正 博士

Advisor : Wen-Cheng Liao, Ph.D.

中華民國 113 年 8 月

August, 2024

doi:10.6342/NTU202403952

國立臺灣大學博士學位論文
口試委員會審定書
National Taiwan University
Doctoral Dissertation Acceptance Certificate

鋼纖維混凝土修正壓力場及軟化壓拉桿模型發展研究

Development of Modified Compression Field Theory (MCFT) and Softened Strut-and-Tie (SST) Model for Steel Fiber Reinforced Concrete (SFRC)

本論文係 Wagh Suyash Kishor 君 (D08521030) 在國立臺灣大學土木工程學系完成之博士學位論文，於民國2024年7月15日承下列考試委員審查通過及口試及格，特此證明

This is to certify that this Doctoral Dissertation is completed by Wagh Suyash Kishor (D08521030) during his/her studying in Department of Civil Engineering at National Taiwan University, and that the oral defense of this thesis/dissertation is passed on 2024/7/15 in accordance with decision of following committee members:

口試委員 Oral Defense Committee members：

Wen-Cheng Liao 廖文正
（指導教授 Advisor）
Yin-Wen Chan 詹穎雯
Min-Yuan Cheng 鄭敏元
Yu-Chen Ou 歐昱辰
Shyh-Jiann Hwang 黃世建

系主任、所長 葛宇甯 （簽名Signature）
(Department Chair/Program Director)

doi:10.6342/NTU202403952

Acknowledgement

I would like to begin by expressing my deepest gratitude to my PhD advisor, Professor Liao Wen-Cheng, for his invaluable guidance and unwavering support. His constant encouragement to think critically, push research boundaries, and develop independent thinking has been a source of inspiration. I am particularly grateful for his constructive feedback and patience, which made him a true mentor and a source of support, especially when I felt far from home.

I would also like to thank the dissertation committee members for their time and effort in reviewing my thesis and attending my defense. Their insightful suggestions for improvement were invaluable.

My sincere gratitude extends to CECI Engineering Consultants, Inc., Taiwan, for their generous one-year scholarship. This financial assistance allowed me to begun my PhD studies at the Department of Civil Engineering, National Taiwan University. Their belief in my potential has had a lasting impact on my career.

I am grateful to my senior, Dr. Wisena Perceka, for his guidance and the time he dedicated to fruitful discussions about my research. I also want to thank Dr. Nguyen Doan Binh and my 812 lab mates for their help and kindness throughout every step of my research. Additionally, I am thankful to my friends from the NTU India Association, especially Amali Gitanjali, Dr. Kalpana Shankhawar, Jones Joju, and Dalip Kumar, for their encouragement throughout my PhD journey. They celebrated my small victories, offered emotional support during challenging times like COVID, and helped me believe in myself.

doi:10.6342/NTU202403952

My appreciation extends to my friends outside of the university: Dr. Ku, Yao-Hua, Oscar Chien, Akash Rajbhandari, and Shubham Kolhe. Their companionship played a crucial role in my journey, helping me navigate through the highs and lows of my PhD. Whether it was through insightful discussions, sharing meals, or simply spending quality time together, their presence made Taiwan feel like a second home. I am truly grateful for their friendship.

Last but not least, my heartfelt gratitude goes to my sister, Ankita. She stood by my parents during challenging times, providing them with the support they needed while I was away. Her strength and resilience allowed me to focus on my studies. I am eternally grateful to my parents, Sujata and Kishor Wagh, for their unconditional love, belief in my abilities, endless support, and countless sacrifices. Despite the distance, their words of wisdom and comfort have been a constant source of strength and motivation for me.

Finally, to everyone who has been a part of this journey, directly or indirectly, your support and encouragement have been instrumental in my reaching this milestone. This achievement is a reflection of your belief in me as much as it is mine.

摘要

鋼纖維混凝土（SFRC）在現代建築中發揮了至關重要的作用，其優越的抗拉強度能提升結構的整體性和性能。SFRC 的主要優勢是能夠減少鋼筋的配置，降低橫向鋼筋的需求。鋼纖維的加入顯著改善了混凝土對開裂、剝落和剪力的抵抗力，確保了結構的安全與使用性。另外鋼纖維使荷載分佈更均勻和改善混凝土抗拉強度的能力，使其成為各種結構元件的理想材料。本研究探討了 SFRC 構件的剪力強度和為並擴展了兩個模型的應用：修正壓力場理論（MCFT）和軟化拉壓桿模型（SST）。

本研究第一部分主要著重於修正壓力場理論（MCFT）的開發，以預測 SFRC 構件受剪力之應力-應變結果。具體來說，本研究旨在通過在多倫多大學的平板測試機上進行的一系列平板測試，來理解高流動性應變硬化纖維混凝土（HF-SHFRC）的剪切行為。這些測試通過測量平板對剪切荷載的響應來捕捉 SFRC 在拉伸中的應變硬化行為，表明即使在初始開裂後，剪切應力仍然會增加。本研究所提出的分析程序利用這些平板測試的實驗數據來預測 SFRC 的剪切應力-應變響應。該分析程序與實驗結果相比後，顯示出其對 SFRC 響應的可靠預測能力。

本研究的第二部分擴展了軟化拉壓桿模型（SST）在 SFRC 孤立斜撐平板和 D 區域（如深梁和梁-柱接頭）的適用性。為了實現這一目標，本研究分析了一項受壓平板綜合實驗計劃的結果，這些測試顯示在受壓荷載下形成了孤立的瓶形斜撐。實驗研究了多種參數的影響，包括長寬比、鋼筋佈局、鋼筋比例、屈服強度和纖維體積比。根據應變數據的分析，確立了主應變的新限制。該模型的預測結果與

這些測試和文獻中獲得的實驗結果進行了驗證。此外，修改後的 SST 模型還應用於 D 區域，以評估其準確性。

在本研究中，通過開發和驗證的修正壓力場理論（MCFT）和軟化拉壓桿模型（SST），來檢查 SFRC 的剪切行為。這些模型提高了預測 SFRC 元件剪切強度和壓縮強度的準確性。

關鍵詞：鋼纖維混凝土、剪切承載力、修正壓力場理論、軟化拉壓桿模型、平板。

Abstract

Steel fiber-reinforced concrete (SFRC) plays a vital role in modern construction due to its superior tensile strength, which enhances structural integrity and performance. One of the key benefits of SFRC is its capacity to reduce reinforcement congestion by decreasing the need for transverse reinforcement. The inclusion of steel fibers significantly improves the concrete's resistance to cracking, spalling, and shear forces, ensuring greater longevity and reliability of structures. Its ability to distribute loads more evenly and its improved tensile strength make it an ideal material for various structural elements. This research investigates the shear strength and behavior of SFRC elements, extending the application of two models: the Modified Compression Field Theory (MCFT) and the Softened Strut-and-Tie (SST) model.

The first part of this thesis focuses on development of Modified Compression Field Theory (MCFT) to predict the shear stress-strain response of steel fiber-reinforced concrete (SFRC) elements. Specifically, the research aimed to understand the shear behavior of highly flowable strain-hardening fiber-reinforced concrete (HF-SHFRC) through a series of panel tests conducted at the University of Toronto's Panel Test Machine. These tests captured the strain-hardening behavior in tension of SFRC by measuring the panels' response to shear loading, as evidenced by the increase in shear stress even after initial cracking. The proposed analysis procedure utilizes experimental data from these panel tests to predict the shear stress-strain response for SFRC. This approach demonstrably yields reliable predictions of the SFRC response when compared to the experimental results.

The second part of this study extends the applicability of the Softened Strut-and-Tie (SST) model to SFRC isolated strut panels and D-region elements, such as deep beams

doi:10.6342/NTU202403952

and beam-column joints. To achieve this, the results of a comprehensive experimental program for panels under compression were analyzed. These tests indicated the formation of isolated bottle-shaped struts under compression loading. The experiment investigated the influence of various parameters, including aspect ratios, reinforcement layouts, reinforcement ratios, yield strengths, and fiber volume fractions. Based on the analysis of strain data, new limits for principal strains were established. The model's predictions were validated against the experimental results obtained from these tests and literature. Furthermore, the modified SST was applied to D-region elements to assess its accuracy.

In this study, the shear behavior of steel fiber-reinforced concrete (SFRC) is examined by developing and validating the Modified Compression Field Theory (MCFT) and Softened Strut-and-Tie (SST) model. These models enhance the accuracy of predicting the shear and compressive strength of SFRC elements.

Keywords: steel fiber reinforced concrete, shear capacity, Modified Compression Field Theory, Softened Strut-and-Tie model, panels.

Table of Contents

doi:10.6342/NTU202403952

doi:10.6342/NTU202403952

doi:10.6342/NTU202403952

doi:10.6342/NTU202403952

List of Figures

doi:10.6342/NTU202403952

doi:10.6342/NTU202403952

doi:10.6342/NTU202403952

List of Tables

doi:10.6342/NTU202403952

Abbreviations

A_s = cross-sectional area of the reinforcing bar

A_{sh}, A_{sv} = cross-sectional area of the reinforcing bar in horizontal and vertical direction

A_{str} = effective area on the nodal zone of the strut

A_{th}, A_{tv} = horizontal and vertical tie areas, respectively

a = maximum size of aggregate

a_p = half the width of loading plate

a_s = depth of the diagonal strut

b = width of the panel (along the transverse axis)

$C_{d,n}$ = compressive strength of the strut

d_b = bar diameter

d_f = diameter of steel fiber

E_c = modulus of elasticity of concrete

E_s = modulus of elasticity of steel bars

F_h, F_v = tension forces in the ties in horizontal and vertical direction, respectively

$\overline{F_h}$ = balanced amount of the horizontal tie force

$\overline{F_v}$ = balanced amount of the vertical tie force

F_{yh}, F_{yv} = yielding forces of the horizontal and vertical ties, respectively

f_h, f_v = stresses in reinforcing bars in h- and v-directions, respectively

f_{yh}, f_{yv} = yield strengths of the bare reinforcing bars in h- and v-directions, respectively

doi:10.6342/NTU202403952

f_s = average stress in the steel reinforcing bar

f_u = ultimate tensile strength of bare reinforcing bar

f_x = stress applied to an element in the *x*-direction

f_y = stress applied to an element in the *y*-direction

f_{c1} = principal tensile stress in concrete

f_{c2} = principal compressive stress in concrete

f_{c2max} = maximum principal compressive stress in crack concrete

f_{cx} = stress in concrete in the *x*-direction

f_{cy} = stress in concrete in the *y*-direction

f_{sx} = stress in steel reinforcement in the *x*-direction

f_{sy} = stress in steel reinforcement in the *y*-direction

f_{yx} = yield stress of *x*-reinforcement

f_{yy} = yield stress of *y*-reinforcement

f_{sxcr} = stress in *x*-direction steel reinforcement at the crack location

f_c' = cylinder strength of concrete

f_{ci} = compressive stress on the crack surface

HSC = High Strength Concrete

h_c = depth of the column

K = strut-and-tie index

K_h = approximated horizontal tie index

K_v = approximated vertical tie index

$\overline{K_h}$ = horizontal tie index

$\overline{K_v}$ = vertical tie index

l = length of the panel (along the longitudinal axis)

l_f = length of steel fiber

l_h, l_v = horizontal and vertical lever arm

l_s = length of the strut

MCFT = Modified Compression Field Theory

NSC = Normal Strength Concrete

P_u = peak compressive load (experimental)

P_{cal} = calculated peak compressive load

R_h, R_v, R_d = ratios of the diagonal compression resisted by the horizontal, vertical, and diagonal mechanisms, respectively

SMM = Softened Membrane Model

SST = Softened strut-and-Tie Model

STM = Strut-and-Tie Model

s_{mx} = the average spacing of cracks perpendicular to *x*-reinforcement

s_{my} = the average spacing of cracks perpendicular to *y*-reinforcement

t = thickness of the panel or RC member

V_f = volume content of steel fibers

V_u = experimental shear force

V_{ucal} = calculated shear force

v_{ci} = shear stress across the crack surface

v_{cr} = applied shear stress at the onset of cracking

v_{cimax} = maximum resistance to shear for a given width of the crack

v_{xy} = shear stress on element relative to *x*, *y* axes

v_u = maximum shear stress element can resist

v_{uexp} = experimental shear strength

v_{umodel} = estimated shear strength

W_f = steel fiber index

w = crack width

α = factors equal to the product of several coefficients for considering average stress, random distribution, and fiber orientation

λ = factors equal to the product of several coefficients for considering average pull-out length, group reduction, and orientation effect

ϵ_1 or ε_r = principal tensile strain in concrete (*1*- or *r*- direction)

ϵ_2 or ε_d = principal compressive strain in concrete (*2*- or *d*- direction)

$\varepsilon_{r(SFRC)}$ = average principal strain for SFRC in *r*-direction

ϵ_{cc} = strain at first cracking

ε_{cx} = Strain in concrete in *x*-direction

ε_{cy} = Strain in concrete in *y*-direction

ε_h, ε_v = average normal strains in the h- and v-directions, respectively

ϵ_{pc} = maximum strain

ε_s = strain in the steel reinforcing bar

ε_{sx} = Strain in reinforcing steel in *x*-direction

ε_{sy} = Strain in reinforcing steel in *y*-direction

ϵ_x = strain in *x*-direction

ϵ_y = strain in *y*-direction

ϵ_c' or ε_o = strain in a concrete cylinder at peak stress f_c'

ϵ_{cr} = strain at cracking of the concrete

γ_h = fraction of the forces transferred by the horizontal tie in the absence of a vertical tie

γ_v = fraction of the forces transferred by the vertical tie in the absence of a horizontal tie

γ_{xy} = shear strain relative to *x*, *y* axes

θ = the angle of inclination of compression strut (for MCFT: with respect to *x*-axis, for SST: with respect to h-axis)

ζ = softening co-efficient of concrete

ρ_{sx} = reinforcement ratio in the *x*-direction

ρ_{sy} = reinforcement ratio in the *y*-direction

σ_d = principal compressive stress in concrete (negative quantity)

σ_{cc} = first cracking strength

σ_{pc} = post cracking strength

σ_{mu} = tensile strength of the matrix

τ_{eq} = equivalent bond strength

doi:10.6342/NTU202403952

Chapter 1 Introduction

1.1 Background

Concrete is a widely used construction material which is composed of cement, aggregate (Fine and coarse) and water, in the construction industry because of its durability (resistance to extreme weather conditions), affordability and versatility. Because of its durable nature, it has been used for centuries and continued to be a preferred choice in construction due to its abundance. The quality of concrete is depends upon the use of water to cement ratio, aggregate to cement ratio, curing conditions, the use of superplasticizers and other admixtures. Based on the compressive strength of the concrete, according to ACI 363-2005 [1] concrete can be classified as high strength concrete (Strength > 55 MPa) or normal strength concrete (Strength < 55MPa). According to the purpose, Normal Strength Concrete (NSC) is often used for wide range of construction projects such as residential homes or commercial buildings; on the other hand, High Strength Concrete (HSC) is used in structures that requires exceptional load bearing capacity, such as high rise buildings and bridges.

Concrete's strength in tension is weak and its brittleness increases as its compressive strength increases and this weakness lead to development of the reinforced concrete (RC) [2]. Steel reinforcing bar, in the form of continuous discrete reinforcement mesh, enhances the tensile properties of concrete. This combination of materials allows for the compressive strength of concrete to be supplemented by the tensile strength of steel.

Since 2009, Taiwan's new RC project has been using HSC and high-strength rebars to reduce the size of structural members and save on material consumption. However, the inherent brittleness of high-strength concrete creates significant concerns, particularly in areas requiring high shear strength or areas where the stresses and strains are disturbed and irregular (D-Regions). Disturbed region (D-Region) is also refereed as local or discontinuity region [3,4], which include end region of beam and column, beam column joints, corbels, the region adjacent to concentrated load, etc. These D-regions are areas where shear failures are more common due to force and geometric discontinuities.

To address this shear failure in D-region and brittle behavior of HSC, design codes require increased shear reinforcement, which leads to steel congestion and construction challenges. To avoid these construction difficulties and tackle the brittleness associated with HSC, fiber-reinforced cement (FRC) composites have emerged as a promising solution to improve the tensile strength of concrete by reducing the requirement of transverse reinforcement [5–8]. FRC composites consist of fibers, such as steel, glass, carbon, polymers, or synthetic materials, embedded randomly within the concrete matrix. These fibers enhance the structural performance of concrete by improving its tensile strength, shear strength, and crack resistance.

1.2 Steel Fiber Reinforced Concrete

Steel fiber-reinforced concrete (SFRC) is a composite material that demonstrates remarkable properties, including enhanced tensile, flexural, and shear strengths, as well as improved crack resistance and toughness [6,7]. The dispersed and randomly oriented steel fibers in concrete also exhibit a non-brittle behavior at the onset of cracking, toughness, and ductility of the composite [5,9–12]. Furthermore, SFRC demonstrates ductile behavior after cracking because the steel fibers effectively bridge cracks, enhancing its attractiveness in the construction industry. Today, SFRC is widely used in constructing beam elements, tunnel linings, and road pavements. Due to its brittle nature, concrete can fail abruptly in shear without warning shortly after the first crack forms when

doi:10.6342/NTU202403952

the principal tensile stress exceeds the tensile strength of concrete within the shear span of a reinforced concrete (RC) element [13]. The incorporation of fibers addresses these issues by enhancing crack control characteristics and resistance to large crack widths. The use of steel fibers in high-strength concrete (HSC) elements can reduce or potentially eliminate the need for conventional transverse reinforcement, improving construction workability, decreasing reinforcement congestion, and leading to more efficient designs. Therefore, a comprehensive analysis of the shear behavior of SFRC, considering all factors affecting shear strength, is essential.

1.3 Shear Theory

The following two models, intended specifically for the local discontinuity regions (D-regions) in concrete structures, are detailed below along with the basic principles on which they are formulated. The Modified Compression Field Theory (MCFT) can generate a complete shear stress-strain curve, while the Softened Strut-and-Tie (SST) model can predict the ultimate shear strength. The rationale for selecting these models for modification is elaborated upon below:

1) The Modified Compression Field Theory (MCFT) is a method developed by Vecchio and Collins [14] to address the shear problems of reinforced concrete elements. It incorporates equilibrium, compatibility, and constitutive relationships to predict the response of RC panels under in-plane shear and axial stresses. Many design codes now base shear design on MCFT, which is also adapted in finite element analysis software. In addition, MCFT is utilized in advanced research fields like dynamic analysis for blast and impact loads, fire analysis, and fatigue analysis [15]. Therefore, understanding the applicability of MCFT for predicting the shear behavior of SFRC elements is crucial.

doi:10.6342/NTU202403952

2) The Softened Strut-and-Tie (SST) model developed by Hwang & Lee [16], is an advanced approach that addresses the limitations of traditional STM by incorporating the softening effects of concrete. The SST model considers force equilibrium, strain compatibility, and the constitutive laws of materials, along with various mechanisms (diagonal, horizontal, vertical, and complete) that contribute to shear resistance. The application of the softened strut-and-tie model can be found in deep beams, squat walls, beep beams, corbels, knee joints, interior and exterior beam-column joints, and pile caps [16–22]. This model has proven instrumental in predicting diagonal compression, shear, and flexural strength (in case of pile caps). The present work aims to extend the application of the SST by accounting for the contribution of fibers and also modifying the formulations based on the experimental results for isolated panels.

1.4 Objectives and scope of the research

This research investigates the shear capacity and behavior of SFRC, specifically using high-strength steel fiber reinforced concrete.

Developed by Vecchio and Collins [14], Modified Compression Field Theory (MCFT), is used to analyze the shear response of SFRC panels tested under pure shear. Since MCFT was found inadequate for predicting the shear stress-strain response of SFRC, modifications were made. The modified MCFT is applied to predict the shear stress-strain curves of SFRC panels available in the literature, subjected to shear loading.

This study also presents an improved analytical model using Softened Strut-and-Tie (SST) approach, originally developed by Hwang & Lee [16], to reliably predict the compressive strength of bottle-shaped struts. The model takes into account the variations in specimen geometry, reinforcement ratios, and steel fiber volume fractions, independent of the layout of reinforcements. This model takes into account the cumulative effects of concrete and reinforcement, including realistic constitutive laws of SFRC, particularly strain hardening and peak stress softening. The gathered data for RC/SFRC panels under compression form the literature were used to predict the compressive strength of bottle-shaped strut by using the proposed SST. Accordingly, this enables a deeper understanding of the behavior of bottle-shaped struts in SFRC elements under in-plane compressive forces.

The Modified SST for SFRC is further used to predict the shear strength of D-Region elements, such as deep beams and beam-column joints, using the data sets assembled from published research.

1.5 Organization of the Dissertation

The organization of dissertation is as follows:

Chapter 1 explains the background of the research, the importance of incorporating steel fibers in structural concrete (SFRC), the objectives and scope of the research, and the organization of the dissertation.

Chapter 2 presents a review of previous studies related to steel fiber-reinforced concrete and constitutive models for SFRC. It covers the mechanical properties of fiber-reinforced concrete and steel fiber pull-out behavior, as well as previous research on shear strength prediction equations for SFRC deep beams and beam-column joints. Furthermore, shear analysis procedures such as the Modified Compression Field Theory (MCFT), Softened Strut-and-Tie (SST) Model, and Softened Membrane Model (SMM) will be discussed.

Chapter 3 specifies an experimental method for examining HF-SHFRC panels and introduces MCFT, an analytical model for predicting the ultimate shear stress of SFRC panels (or MCFT for SFRC). The model's validity is confirmed by predicting the shear stress of SFRC shear panels based on data collected from the literature (Appendix A). A sample calculation is included. The organization of Chapter 3 is depicted in Figure 1-1.

Chapter 4 presents the experimental findings for RC and SFRC panels under compression, discussing the formation of bottle-shaped struts. After analyzing the strain data and incorporating realistic constitutive laws for SFRC, a shear strength prediction model formulated upon SST (SST for SFRC) is proposed to determine the compressive strength of the bottle-shaped strut in both RC and SFRC panels. Sample calculation is provided, and the data collected for these panels is found in Appendix B. The methodology followed in developing Modified SST for SFRC is given in Figure 1-2.

Chapter 5, the variability of different parameters, such as volume fraction of fibers, ratio of the reinforcement, and shear span to effective depth ratio (for deep beams) and vertical to horizontal lever arm ratio (for beam-column joints), affecting the shear strength are studied and compared with other shear strength prediction equations.

Chapter 6 demonstrates the application of the Modified SST to SFRC deep beams, validating its applicability and accuracy. A comparison is made with previously suggested shear strength prediction equations. Sample calculation is provided, and the collected data for the deep beams can be found in Appendix (C). Chapter 6 also represents the application of Modified SST for SFRC Beam-Column joint to verify their validity and applicability. Sample calculation is included for reference.

doi:10.6342/NTU202403952

Chapter 7 summarizes the overall conclusions of the present study with suggestions for potential future research.

The structure of this dissertation is outlined in the flowchart presented in Figure 1-3.

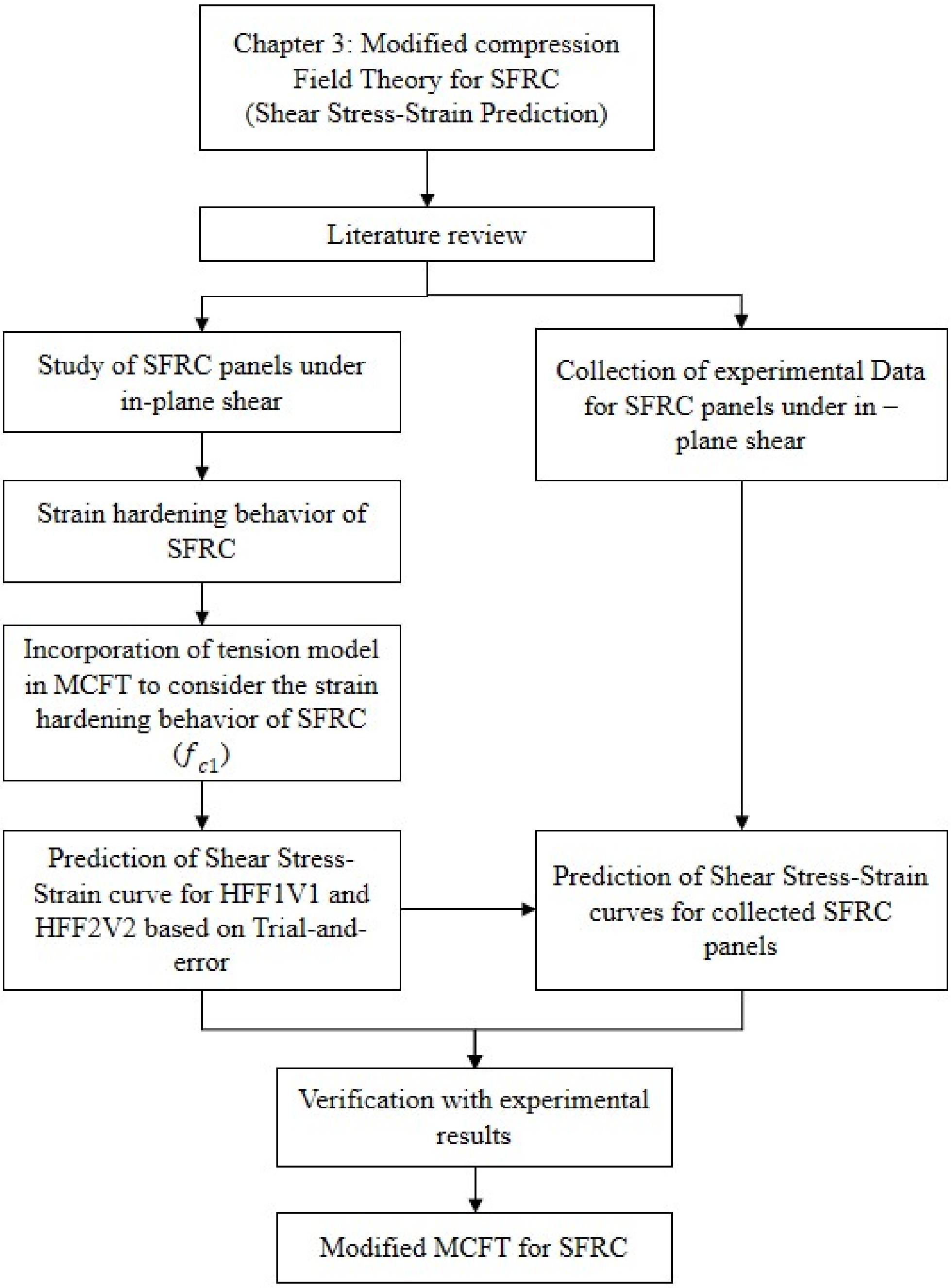

Figure 1-1 Organization of Chapter 3

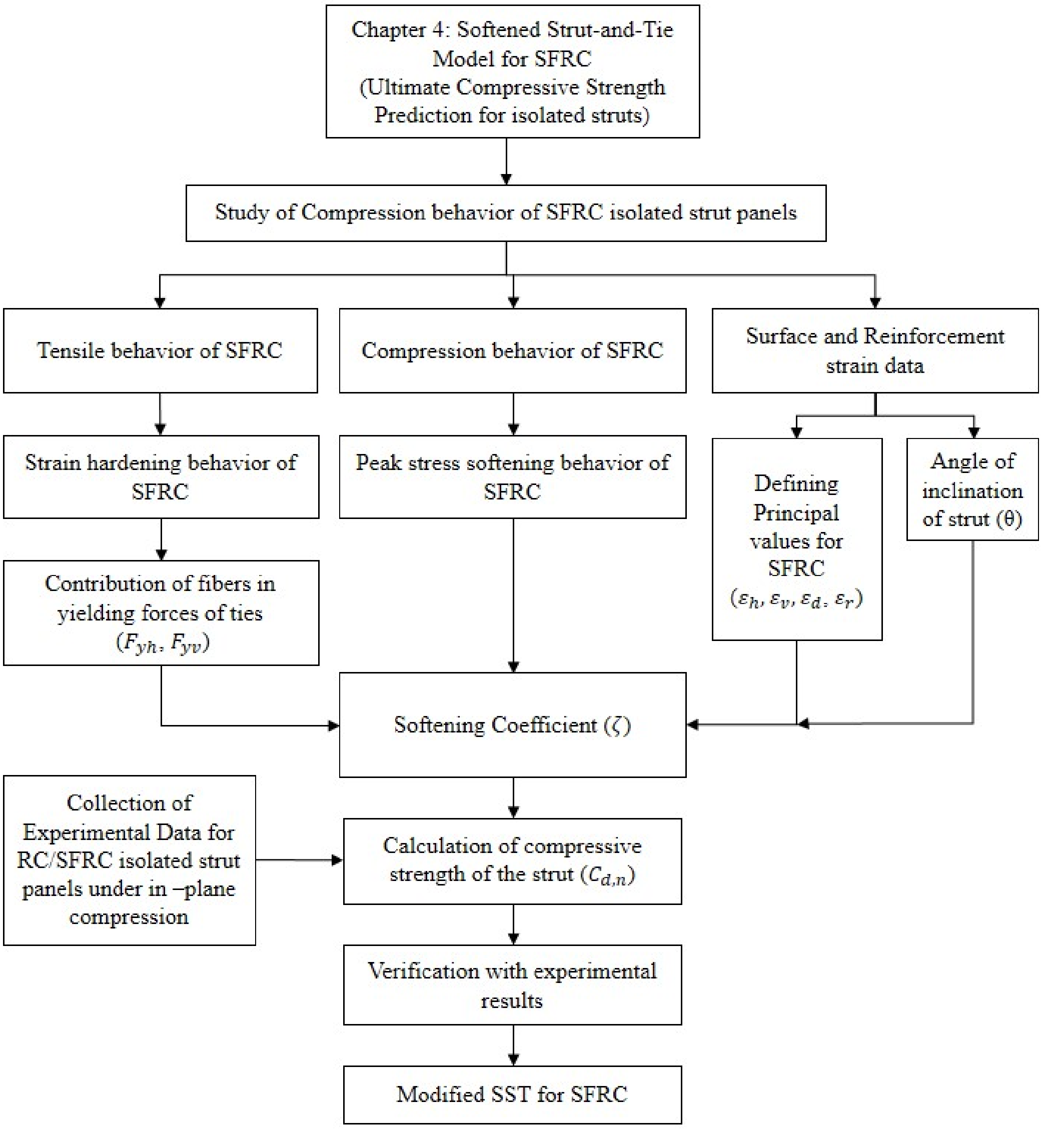

Figure 1-2 Organization of Chapter 4

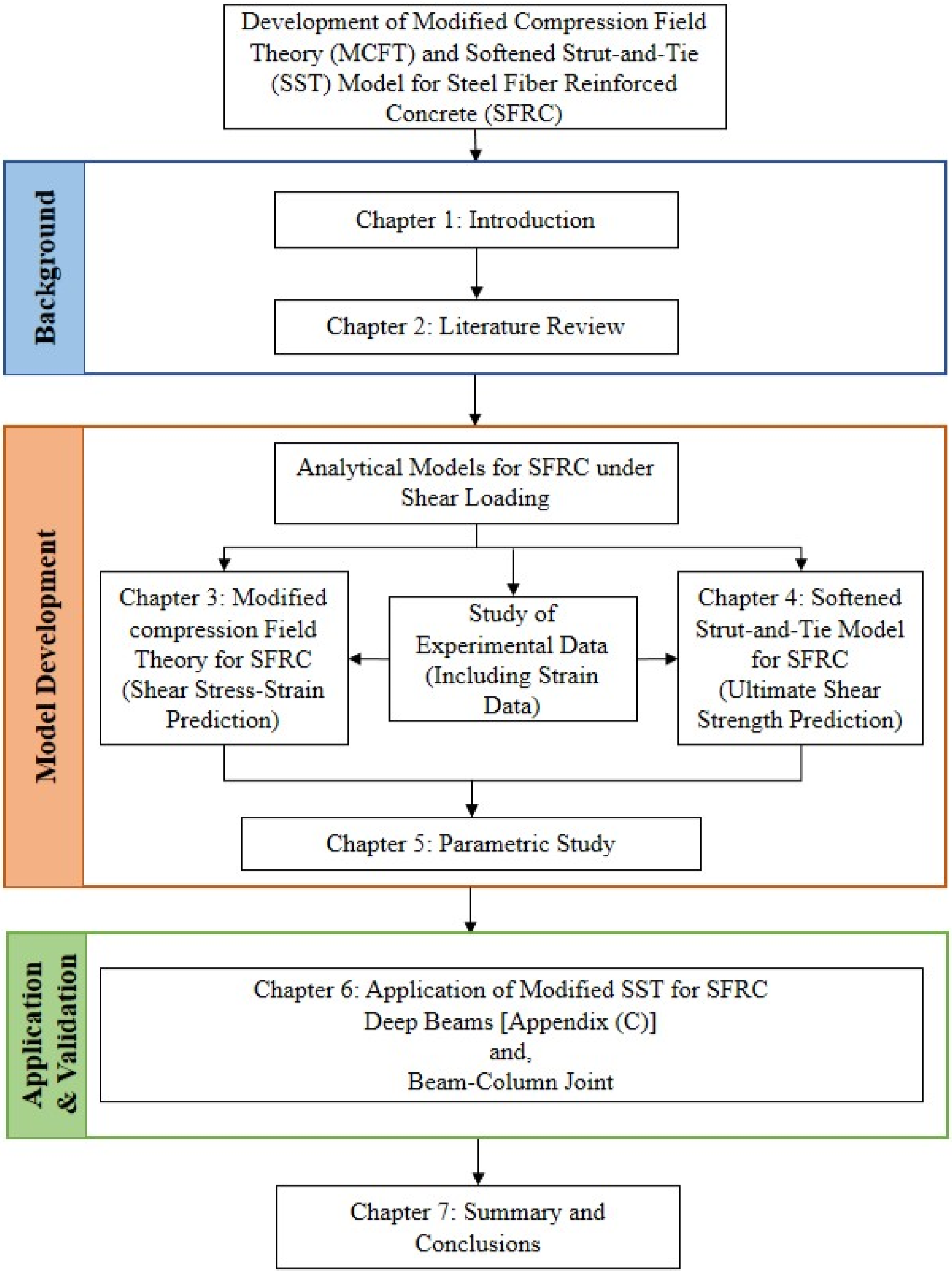

Figure 1-3 Structure of the Dissertation

doi:10.6342/NTU202403952

Chapter 2 Literature Review

2.1 Normal Concrete and Fiber-Reinforced Concrete (FRC) under Compression and Tension

2.1.1 Behavior of normal concrete (without fibers)

Under compression, normal concrete without fiber reinforcement exhibits complex behavior under compressive loading, characterized by its brittle nature, especially in high-strength formulations. The stress-strain relationship in compression is initially linear-elastic up to about 30-40% of the ultimate strength. Beyond this point, the behavior becomes increasingly non-linear as microcracks begin to form, primarily at the interfaces between the cement paste and aggregates.

As the load approaches the peak strength, these microcracks propagate and merge, leading to the formation of larger cracks. The peak compressive strength represents the maximum load-carrying capacity of the concrete. In high-strength concrete (HSC), this peak is typically higher than in normal-strength concrete, but the post-peak behavior is markedly different. After reaching the peak strength, normal concrete, and particularly HSC, experiences a rapid decrease in load-carrying capacity. This is represented by a steep descending branch on the stress-strain curve.

Under tension, normal concrete without fiber reinforcement exhibits significantly different behavior under tension compared to compression, characterized by much lower strength and even more pronounced brittleness. The tensile strength of concrete is typically only about 8-15% of its compressive strength, making it a critical weakness in many applications.

Under tensile loading, concrete initially behaves elastically, with a nearly linear stress-strain relationship. However, this elastic phase is limited. As the tensile stress increases, microcracks begin to form, primarily at the interfaces between the cement paste and aggregates, similar to the compression behavior but at much lower stress levels.

The key difference in tension is that once these microcracks begin to form, they propagate rapidly and form into larger cracks. This occurs because the tensile stress concentrates at the crack tips, leading to further crack growth. Unlike in compression, where the material can still carry load through aggregate interlock and friction, in tension, crack formation leads to an almost immediate loss of load-carrying capacity.

2.1.2 Behavior of Fiber Reinforced Concrete (FRC)

Under compression, the compressive stress-strain relationship reveals how concrete behaves under compression. Studies by Fanella and Naaman [23], Naaman and Homrich [24], and Hsu and Hsu [25] indicate that incorporating steel fibers changes this relationship of concrete. An increase in fiber content and/or fiber aspect ratio results in increase in strain. Figure 2-1 illustrates the varying behavior between plain concrete and steel fiber reinforced concrete (SFRC) based on fiber content and aspect ratio.

According to previous experiments, adding steel fibers did not significantly improve compressive strength. A study by Thomas and Ramaswamy [26] indicates that adding fibers increases compressive strength by only about 10% across various grades of concrete. Another study by Song and Hwang [27] shows that the improvement in compressive strength for high-strength steel fiber reinforced concrete ranges from 7.1% to 15.3% for volume fractions of 0.5% to 2%. However, a slight decrease in compressive strength was noted at a 2% volume fraction of fiber. Wafa and Ashour [28] also noted that increasing the steel fiber content from 0% to 1.5% raises the compressive strength of

doi:10.6342/NTU202403952

concrete by approximately 4.6%. Additionally, Fanella and Naaman [23] stated that the strain at peak stress increases with the presence of any type of fiber, and the strength improvement using steel fibers ranges from 0% to 15%. Similarly, Hsu and Hsu [25] concluded that the addition of steel fibers increases the strain corresponding to peak stress but does not result in significant changes in the compressive strength of concrete.

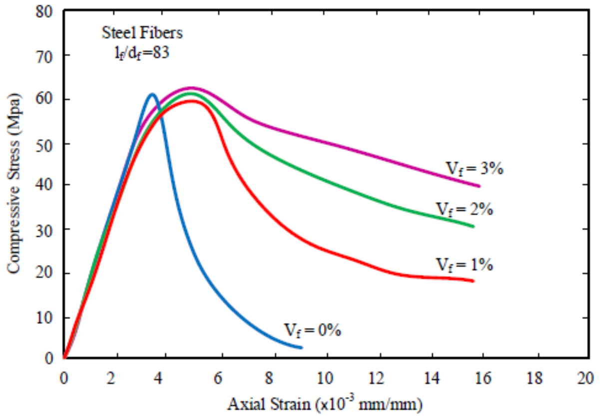

(a) Influence of Fiber Content

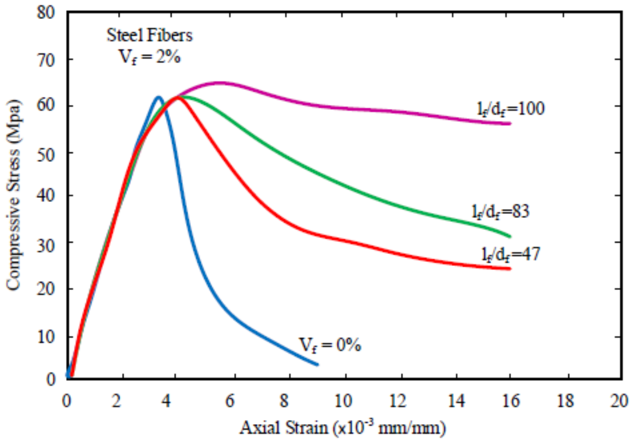

(b) Influence of Fiber Aspect Ratio

Figure 2-1 Compressive Stress-Strain Curve [23]

Under Tension, the exact tensile strength of SFRC remains undetermined due to the absence of a standardized direct tension test procedure. However, several studies have demonstrated that adding steel fibers greatly improves tensile strength. Splitting test results from Thomas and Ramaswamy [26] and Wafa and Ashour [28] indicated substantial improvements with the inclusion of steel fibers. Thomas and Ramaswamy [26] examined SFRC specimens with steel fiber volume fractions of 0%, 0.5%, and 1%, and compressive strengths of 35, 65, and 85 MPa, revealing that tensile strength could increase by up to 40%. Similarly, Wafa and Ashour [28] found that splitting strength correlated with the volume fraction of steel fibers, with a 1.5% volume fraction resulting in a 55.7% increase in splitting strength compared to specimens without steel fibers.

Further experimental results for the splitting tensile test conducted by Song and Hwang [27] are indicated in Figure 2-2. The test results also demonstrated that the strength of SFRC improves with increasing fiber volume fraction, starting at 19% for a 0.5% volume fraction and reaching 98.3% at a 2% volume fraction. Additionally, research by Yazici and Tabak [29] concluded that the split tensile strengths of SFRC are 11% to 54% higher than those of the control mixture and increase with the fiber volume.

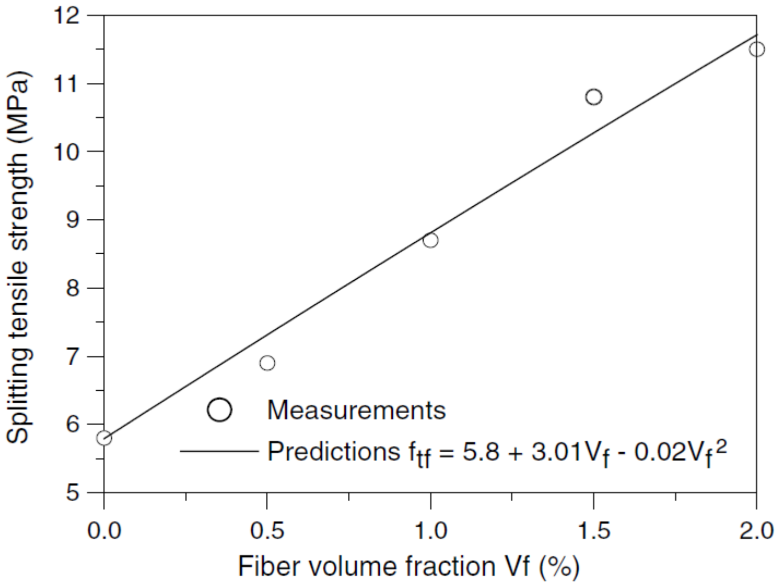

Figure 2-2 Effect of fiber addition on splitting tensile strength [27]

To accurately predict the behavior of reinforced concrete, a robust constitutive model for concrete in tension, particularly the post-cracking response, is essential. The average post-cracking tensile stress is determined as the maximum value of tensile stress resulting from both tension stiffening and tension softening. It is well known that after cracking occurs, the concrete between cracks continues to carry tensile forces, thereby stiffening the response of a reinforced concrete member under tension. This effect, known as tension stiffening, also enhances the rigidity of a reinforced concrete member before the reinforcement yields. While plain concrete is assumed to carry tension only between cracks, steel fiber reinforced concrete (SFRC) can carry significant tensile forces at the crack itself, in addition to the tension between cracks [30].

Evans and Marathe [31] reported that direct tensile test results for plain concrete can reach a maximum tensile strain of approximately 0.7% for certain mix designs. Similarly, Liao et al. [32] conducted direct tensile tests on HPFRCC containing 1.5% fiber and found that the maximum tensile strain was also 0.7%, as illustrated in Figure 2-3. This indicates that the maximum tensile strain for both plain concrete and SFRC is nearly identical. Therefore, using 0.7% as a conservative estimate for the maximum tensile strain is appropriate for both plain concrete and SFRC.

doi:10.6342/NTU202403952

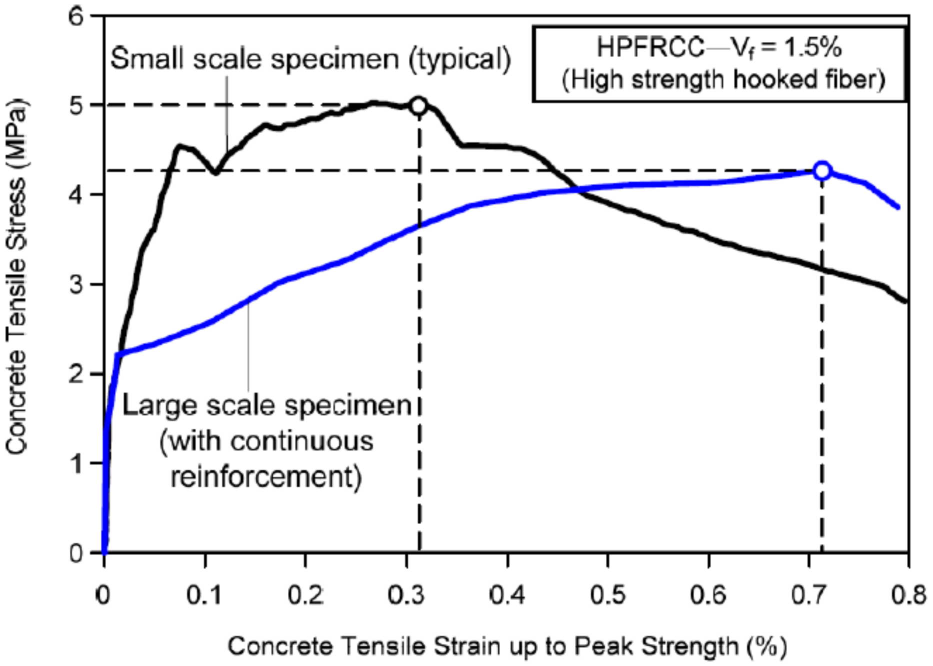

Figure 2-3 Stress - Strain responses for small and large scale specimens using HPFRCC mixture [32]

2.1.3 Mechanical behavior of steel fiber reinforced concrete under tension

Tensile tests by Naaman [33] demonstrated the impact of steel fibers on behavior of concrete. In plain concrete (curve A, Figure 2-4), cracking under tension leads to rapid crack growth and a significant drop in tensile strength, resulting in brittle failure. The peak strength represents the cracking strength.

For conventional FRC (curve B) exhibits similar behavior initially, with a sharp decrease in strength after cracking. However, unlike plain concrete, the strength reduction slows down in the later stage due to strain softening. This indicates that reinforced concrete can sustain some tensile strain after reaching peak strength, exhibiting improved toughness.

However, high performance fiber reinforced cement composites (curve C) shows a distinct response. The presence of fibers allows the material to bridge cracks, leading to continued strength gain after initial cracking. This phenomenon, known as strain hardening, results in a higher ultimate tensile strength compared to the cracking strength. Eventually, strain softening sets in, and the material fails after reaching its peak strength.

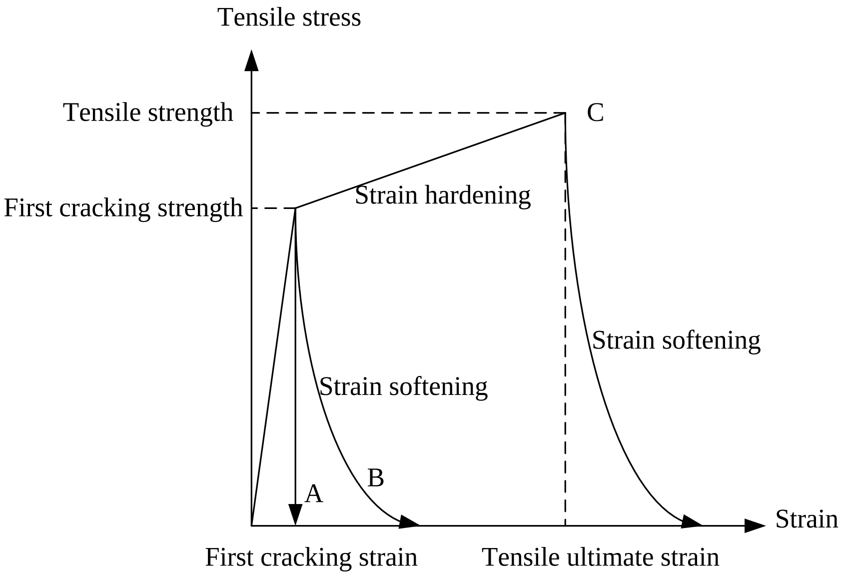

Figure 2-4 Behavior of SFRC under Direct Tension [33]

Figure 2-5 further illustrates the distinction between strain-hardening and strain-softening of steel fiber concrete. The key difference lies in the segment following the cracking stress (segment AB in the curves). For strain-hardening concrete (before crack opening stage), the ultimate stress continues to increase beyond the cracking stress.

doi:10.6342/NTU202403952

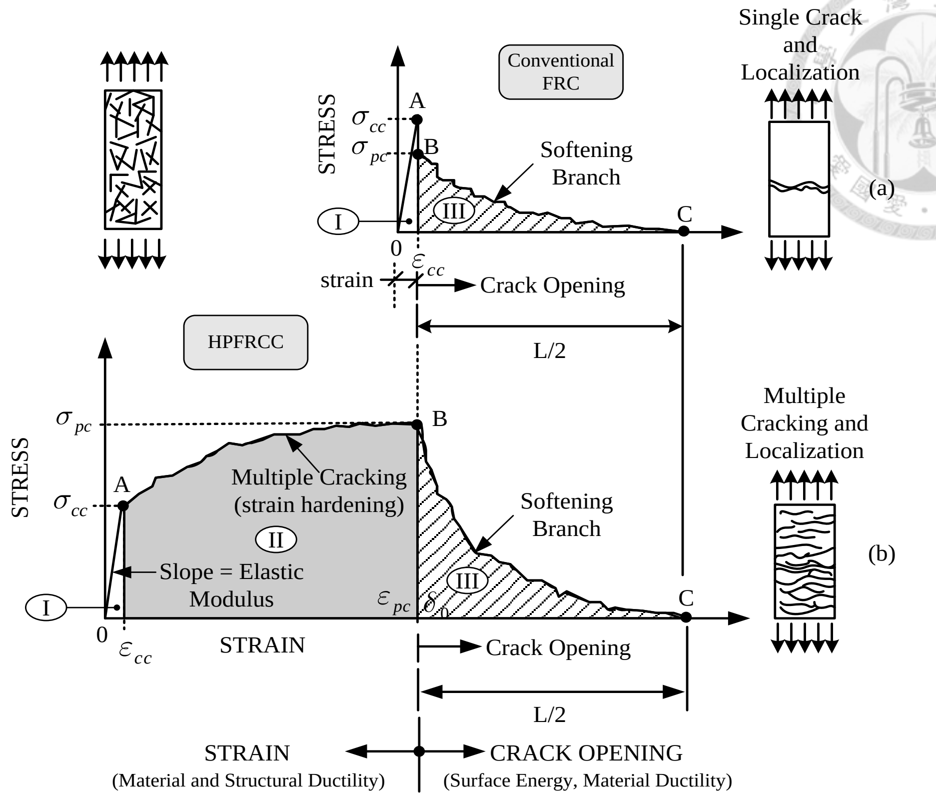

Figure 2-5 Strain Hardening and Strain Softening behavior of SFRC [33]

Fantilli et al. [34] investigated the cracking strength of steel fiber concrete (SFRC) under tension. The scenario where cracks develop perpendicular to the direction of loading and assumed a three-dimensional, random distribution of circular steel fibers within the cracked section. Based on the ultimate tensile strength of plain concrete, the bond strength between steel fibers and the surrounding mortar, and the influence of fiber type and content, they proposed a prediction formula for SFRC cracking strength. The Eq. (2-1) is presented below:

$$\sigma_{cc} = \sigma_{mu}(1-V_f) + \alpha_1\alpha_2\alpha_3\tau V_f \frac{L_f}{d_f} \tag{2-1}$$

Where,

σ_{cc} : cracking strength of SFRC

σ_{mu} : ultimate tensile strength of mortar

V_f : fiber volume fraction

L_f & d_f : length and diameter of fiber

$\alpha_1\alpha_2\alpha_3$: Reduction coefficient account for bond ($\alpha_1\alpha_3$), fiber orientation (α_2), (Chapter 4 provides additional details).

τ: bond strength of steel fiber and cement matrix

For strain-hardened steel fiber concrete (SH-SFRC), the author focused on the post cracking tensile strength and proposed prediction Eq. 2-2 and 2-3 based on the following assumptions:

1. **Pull-out failure:** Steel fibers fail by being pulled out of the surrounding concrete matrix.
2. **Perpendicular cracks:** Cracks develop perpendicular to the direction of the applied tensile stress.
3. **Post-cracking behavior:** After initial cracking, only the pull-out force between the steel fibers and the cement mortar contributes to the tensile strength.

$$\sigma_{pc} = \lambda_1\lambda_2\lambda_3\lambda_5\tau V_f \frac{L_f}{d_f} \tag{2-2}$$

$$\lambda_2 = 4\alpha_2\lambda_4 \tag{2-3}$$

σ_{pc}: post-cracking strength

$\lambda_1\lambda_2\lambda_3\lambda_4\lambda_5$: reduction factor equals to product of several coefficients considering fiber orientation effect, pull out length, and group reduction factor. More details are in Chapter 4.

doi:10.6342/NTU202403952

2.2 Mechanical Properties of SFRC

2.2.1 Crack Controlling

According to Narayanan and Darwish [13], the crack patterns of SFRC beams loaded under shear are similar to those of plain concrete beams with transverse reinforcement. Additionally, the use of fibers reduces the crack spacing in SFRC beams to one-fifth of that in plain concrete beams without transverse reinforcement. The more consistent distribution of stresses in the fiber-reinforced concrete beams accounts for this reduction. Other research on SFRC panels tested under shear loading by Susetyo et al. [7], also concludes that the addition of fibers leads to better control of crack widths.

2.2.2 Toughness

Another key mechanical property is toughness, which is measured by the area under the stress-strain curve. The toughness index quantifies the toughness of a fiber-reinforced matrix compared to a non-reinforced matrix. Fanella and Naaman [23] found that the toughness index typically improves in correlation with the volume proportion of fibers. Sahoo et al. [12] made similar observations for SFRC isolated strut panels using normal strength steel and concrete and different volume of fibers.

2.2.3 Bond Strength

Experimental studies on the bonding capability of SFRC show that the inclusion of fibers significantly enhances the bond strength between concrete and reinforcing bars, especially in cases of splitting bond failure [35,36]. Additionally, Hota and Naaman [37] found that fibers slow down the post-peak degradation, thereby increasing the ductility of the pull-out response. Moreover, an increase in the fiber volume percentage enhances the bonding strength between reinforcing bars and concrete [35–37].

2.3 Softening effect on cracked SFRC

When an RC element experiences vertical compression and horizontal tension, the compressive strength of the concrete is significantly reduced compared to that of a standard concrete cylinder, as demonstrated in Figure 2-6. This softening effect was first identified by Robinson [38] in the year 1961 during the analysis of thin-walled RC beams. Since then, it has been extensively studied using RC panel elements under monotonic loading [14,39–41]. This so called softening phenomenon, affects both compressive strength and strain. According to Belarbi & Hsu [39], the softening effect can be described by:

$$\sigma_d = \zeta f_c' \left[2\left(\frac{\varepsilon_d}{\zeta\varepsilon_0}\right) - \left(\frac{\varepsilon_d}{\zeta\varepsilon_0}\right)^2 \right] \text{ for } \frac{\varepsilon_d}{\zeta\varepsilon_0} \leq 1 \quad (2\text{-}4)$$

$$\sigma_d = \zeta f_c' \left[1 - \left(\frac{\varepsilon_d/\zeta\varepsilon_0}{4/\zeta - 1}\right) \right] \text{ for } \frac{\varepsilon_d}{\zeta\varepsilon_0} > 1 \quad (2\text{-}5)$$

The softening coefficient ζ in proportional loading is given by,

$$\zeta = \frac{0.9}{\sqrt{1 + 400\varepsilon_r}} \quad (2\text{-}6)$$

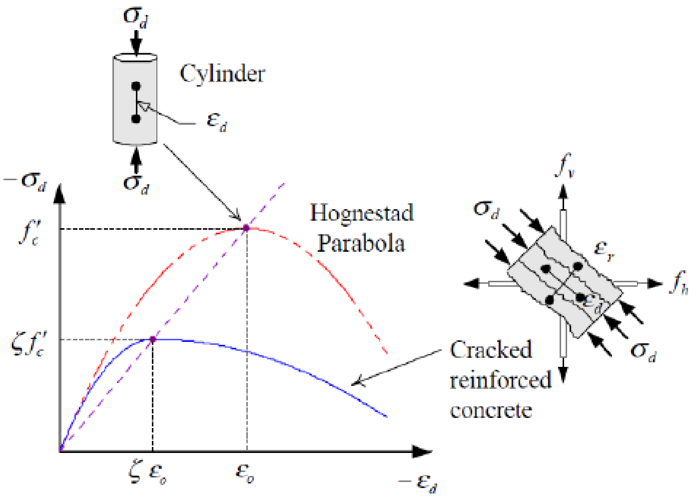

Figure 2-6 Softened compressive stress-strain curve due to transverse tensile strain [42]

doi:10.6342/NTU202403952

Nevertheless, because high-strength concrete is brittle, the descending branch of the stress-strain curve is considerably sharp compared to normal-strength concrete. Consequently, the ζ prediction utilized for concrete with normal strength is not suitable for concrete high-strength concrete [40]. Thus, Zhang & Hsu [40] provide a modified prediction for ζ in high strength concrete by substituting the constant 0.9 with the factor $R(f_c')$, which is inversely proportional to $\sqrt{f_c'}$ as given below:

$$R(f_c') = \frac{C}{\sqrt{f_c'}} \tag{2-7}$$

Where, f_c' is in MPa, and the value of C is taken as 5.8, based on the experimental data. Conclusively, the softening coefficient $\zeta$is revised to be

$$\zeta = min\left(\frac{5.8}{\sqrt{f_c'}}, 0.9\right) \times \frac{1}{\sqrt{1 + 400\varepsilon_r}} \tag{2-8}$$

2.4 Steel fiber pull out behavior

2.4.1 Steel fiber pull out mechanism

The pull-out work refers to the work done by the pull-out load when the fiber disintegrates from the matrix, as explained by Alwan et al. [43]. It is presumed that the tensile stress acting on the fiber surpasses the fiber's maximum strength, indicating that the fibers will not yield or fracture, even when significant cracks develop in the material during later stages of loading. The fiber pull-out process has a substantial impact on the overall energy usage during the cracking process in this phase. The pull-out curve can be anticipated by considering the bond shear stress and slip, and it is separated into three distinct zones.

1) Pre-critical region

The pre-critical region refers to the phase where the fiber is assumed to be elastically bonded to the matrix. During this period, the bond between the concrete and steel fiber is formed through the inter-hydration process after the paste is poured.

2) The partial debonding region

The partial debonding zone refers to a phase in which only a portion of the fiber is bonded. Its behavior is primarily influenced by the maximal elastic bonded shear stress and the initial frictional shear stress. During this stage, the concrete becomes unable to withstand external tensile stress and begins to crack. The steel fibers situated between the bridged cracks continue to transfer tensile stress, preventing rapid crack expansion.

3) The pull out region

The fiber becomes completely debonded, and the kinematic mechanism of pull-out becomes predominant. During this phase, the deformation of the matrix can be disregarded, and the relative slip between the fiber and matrix is roughly equivalent to the end displacement of the fiber. Meanwhile, as the external tensile load continues to increase, the anchoring region will be compromised, causing the fibers to straighten and slide. Throughout this process, the fibers absorb energy and convert it into strain energy.

FRC composites exhibit strain-hardening characteristics under tension, which is accompanied by the occurrence of several cracks. In order to exhibit strain-hardening and multiple cracking behavior, the post-cracking strength of the composites needs to surpass their initial cracking strength [44,45]. Additionally, slip-hardening in single fiber pull-out behavior is crucial for the strain-hardening properties of the composite. The pull-out behavior of hooked fibers is illustrated in Figure 2-7.

doi:10.6342/NTU202403952

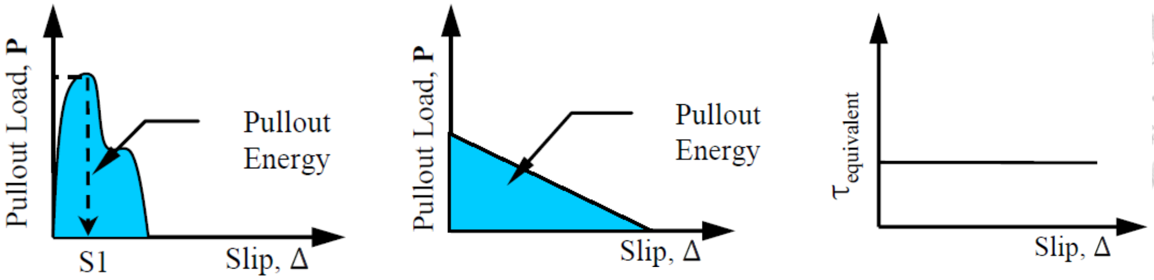

(a) Real $P-\Delta$ curve (b) Equivalent $P-\Delta$ curve (c) Equivalent $\tau-\Delta$ Curve

Figure 2-7 Hooked Fiber Pull-Out Behavior [46]

To demonstrate strain-hardening behavior, the maximum strength after cracking must exceed the strength at the point of initial cracking. The post-cracking strength depends on the average bond strength at the interface, which is assumed to remain stable within a limited range of slip [46]. The equivalent bond strength can be determined by applying the following equations:

$$E_{pullout} = \frac{P\Delta}{2} = \frac{(\pi d_f \tau_{eq} \frac{L_f}{2})(\frac{L_f}{2})}{2} = \frac{\pi d_f L_f^2}{8} \tag{2-9}$$

Where,

$E_{pullout}$: Steel fiber pullout energy

P : Steel fiber pull out force

Δ : slip

τ_{eq} : equivalent bond strength

L_f and d_f: Length and diameters of fiber

After rearranging the terms, τ_{eq} can be given as follows:

$$\tau_{eq} = \frac{8E_{pullout}}{\pi d_f L_f^2} \tag{2-10}$$

The specimen in this research utilized hooked-end steel fibers. These fibers have hooks at both ends, as indicated by their name. Figure 2-8 illustrates the detailed geometry of the hooked-end steel fiber. The arched segment connecting the main straight fiber with the inclined straight segment is labeled C_2, while the other arched segment is labeled C_1. The total lengths of these segments at the ends are denoted as l_{h1} and l_{h2}, respectively.

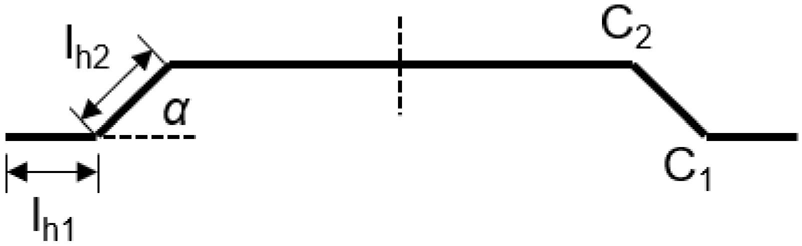

Figure 2-8 Detail Geometry of Steel Fiber Hooked End [47]

According to Xu et al. [47], have identified three different phases in the pullout process of a hooked-end steel fiber. During the initial phase, when the force P is exerted, the hooked end components $lh1$ and $lh2$ undergo a progressive deformation and pass through the arched segments C1 and C2. During the subsequent phase, only the $lh1$ component undergoes deformation and successfully traverses C2. During the last phase, the hooked end is fully extracted from the channels, causing the hooked-end steel fiber to exhibit similar characteristics to a straight steel fiber. Figure 2-9 displays the diagram illustrating the pullout process.

The micromechanical frictional pulley model can be employed to study the energy dissipation of a hooked-end steel fiber throughout pullout stages 1 to 3. This analysis can be done using the superposition method, as depicted in Figure 2-10. This principle is employed to compute the overall energy dissipation throughout the fiber pulling procedure. At first, the curved part of the steel fiber is assumed to be a straight fiber. Then, the plastic deformation of the curved part is taken into account without considering the friction with the surrounding material.

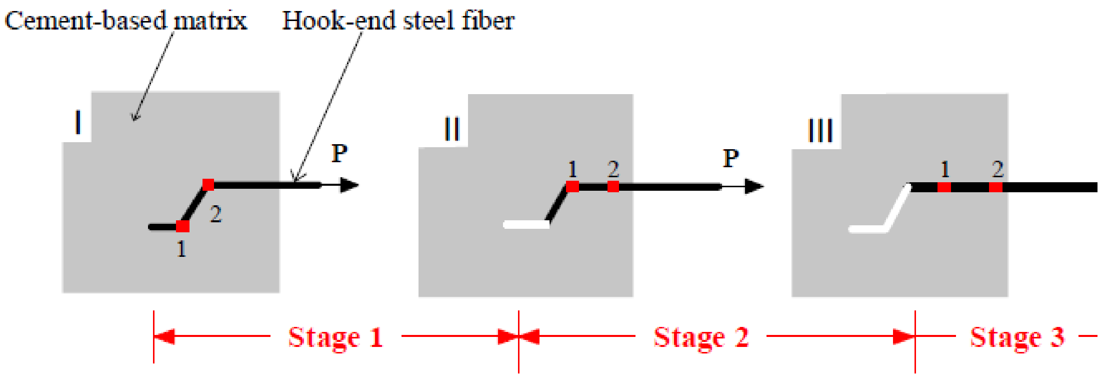

Figure 2-9 The Schematic of Steel Fiber Hooked-End Pullout Process [47]

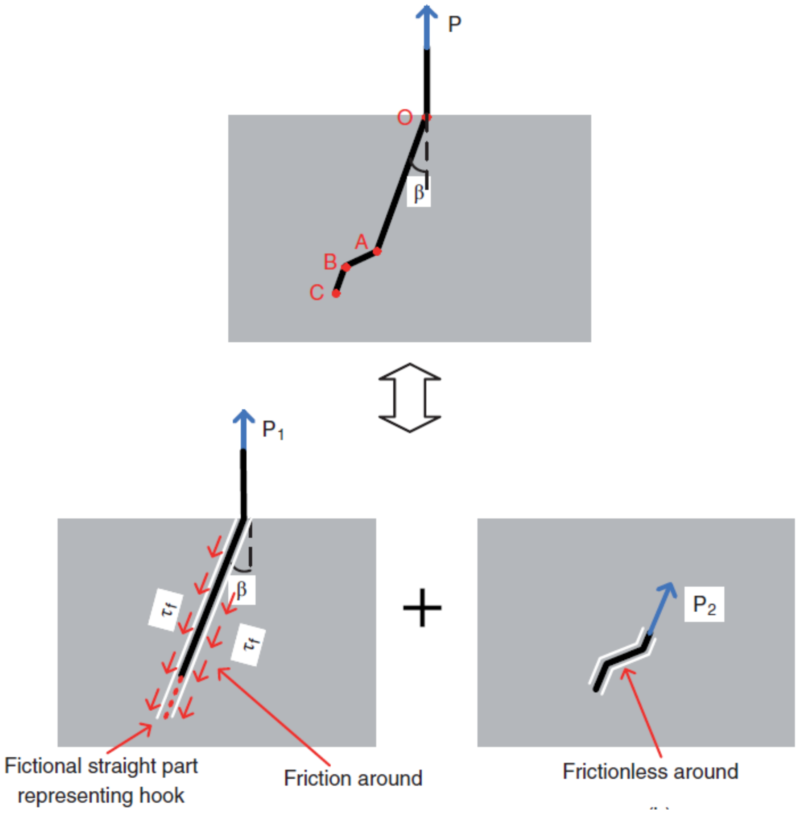

Figure 2-10 Analysis of Hooked-End Steel Fiber Pullout Energy by Superposition Principle [47]

doi:10.6342/NTU202403952

Li et al. [48] and Li [49] suggested that by assuming a uniform frictional stress between the straight fiber and the cement-based matrix, and ignoring the elastic stretching of the fiber during the pullout process, the relationship between the applied force (P) and the displacement (δ) during the frictional pullout stage can be calculated as follows:

$$P(\delta,\beta)=k\pi\tau_f d_f (l_e-\delta), 0\le\delta\le l_e \tag{2-11}$$

$$k=e^{f\beta}=\frac{2}{4+f^2}(1+e^{\frac{\pi f}{2}}) \tag{2-12}$$

Where,

P : Steel fiber pull out force

k : snubbing factor

τ_f : Friction between the contact surface of straight steel fiber and cement matrix

l_e : fiber embedded length

δ : fiber frictional sliding distance

β : fiber inclination angle

f : snubbing coefficient

Due to the presence of Coulomb friction between the hooked segments and the arched segments C_1 and C_2, a factor c_0 was introduced to account for this friction at the arched channels. The value of c_0 can be determined from the initial condition when $\delta = 0$ [47]:

$$c_0=\frac{P_{\max-f}}{\pi\tau_f d_f l_e} \tag{2-13}$$

Where P_{max-f} is the maximum frictional pullout force, which includes the surface friction force $P_{\delta=0}$= $\pi\tau f d_f l_e$ at $\delta=0$, and the Coulomb friction forces F_{f1} and F_{f2} at the arched segments C_1 and C_2. According to Alwan et al. [50], this can be calculated as:

$$F_{f1}=\frac{\mu\sigma_y\pi r_f^2\cos\varphi}{6\cos\alpha(1-\mu\cos\varphi)} \tag{2-14}$$

$$F_{f2}=\frac{\mu\sigma_y\pi r_f^2\cos\varphi(3-\mu\cos\varphi)}{6\cos\alpha(1-\mu\cos\varphi)^2} \tag{2-15}$$

$$\varphi=\frac{\pi-\alpha}{2}=\frac{3\pi}{8} \tag{2-16}$$

$$P_{\max-f}=F_{f1}+F_{f2}+P_{\delta=0}=\frac{\mu\sigma_y\pi r_f^2\cos\varphi(2-\mu\cos\varphi)}{3\cos\alpha(1-\mu\cos\varphi)^2}+\pi\tau_f d_f l_e \tag{2-17}$$

Where,

τ : coulomb friction coefficient

d_f : steel fiber radius

σ_y : steel fiber yield stress

Additionally, Alwan et al. [50] noted that both pulleys exhibit a rotational component F_r, which corresponds to the work needed to straighten the steel fiber at plastic hinges. Moreover, the frictional components $F_{f1}$and F_{f2} correspond to the work done by the Coulomb friction between the steel fiber and the matrix at segments C_1 and C_2. The micromechanical frictional pulley model developed by Alwan et al. [50] is depicted in Figure 2-11.

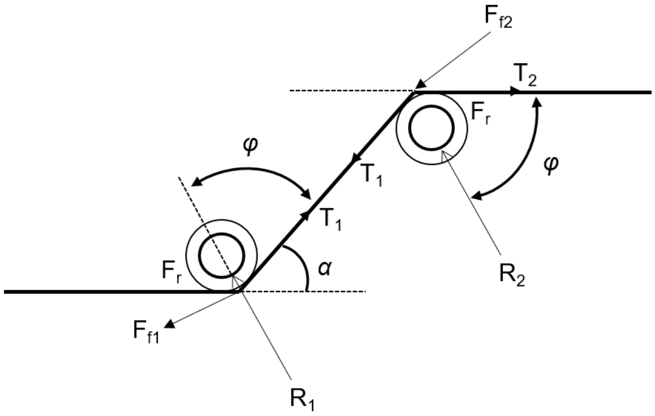

Figure 2-11 The Frictional Pulley Model of A Hooked-End Steel Fiber [50]

Finally, the frictional pullout energy of the hooked steel fiber can be determined by integrating the frictional force over the slipping displacement.

$$g_f(l_e,\delta,\beta)=\int_0^{\delta}Pd\delta=\int_0^{\delta}c_0\pi\tau_f d_f(l_e-\delta)e^{f\beta}d\delta=\frac{kP_{\max-f}}{l_e}(l_e\delta-\frac{\delta^2}{2}),\delta\le l_e \qquad (2\text{-}18)$$

2.4.2 The plastic deformation energy

Dong and Li [51] described the steel fiber pullout process as comprising three separate phases: elastic, elastic-plastic, and plastic. In order to calculate the energy associated with plastic deformation, it is assumed that the steel fiber represent as an elastic-perfectly plastic material. Additionally, the hooked end segment of the fiber is considered as a beam. Moreover, C1 and C2 are regarded as having consistent curvatures, and the correlation between the moment of the beam and curvature is defined as follows:

Elastic stage:

$$M=\frac{\pi E_f r_f^4}{4\rho} \qquad (2\text{-}19)$$

Elastic-plastic stage:
(Figure 2-12)

$$M=M_e+M_p=4\sigma_y r_f^3\left[\frac{1}{\sin\theta_e}(\frac{\theta_e}{8}-\frac{\sin(4\theta_e)}{32})+\frac{\cos^3\theta_e}{3}\right] \qquad (2\text{-}20)$$

Where, $\theta_e=\sin^{-1}\frac{\sigma_y\rho}{E_r r_f}$

Plastic stage:

$$M=\frac{4\sigma_y r_f^3}{3} \qquad (2\text{-}21)$$

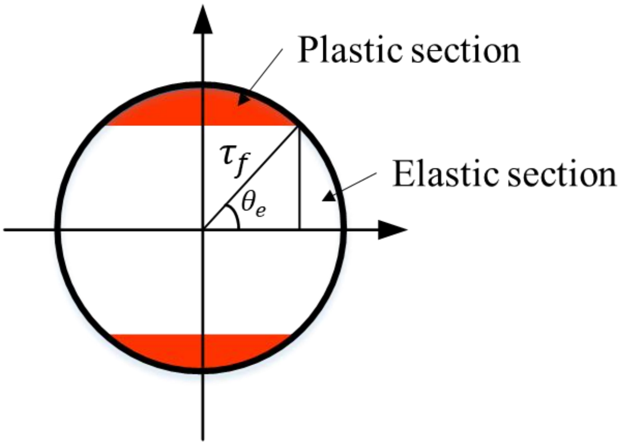

Figure 2-12 The Stress Distribution of the Hooked-End Segment in Elastic-Plastic Stage [51]

Figure 2-13 illustrates the plastic deformation energy of the hooked end segment within a slight slipping distance d_x and rearranged as

$$de_{pi}=\left[\int Md\left(\frac{1}{\rho}\right)\right]dx=(A_{i1}+A_{i2})dx \tag{2-22}$$

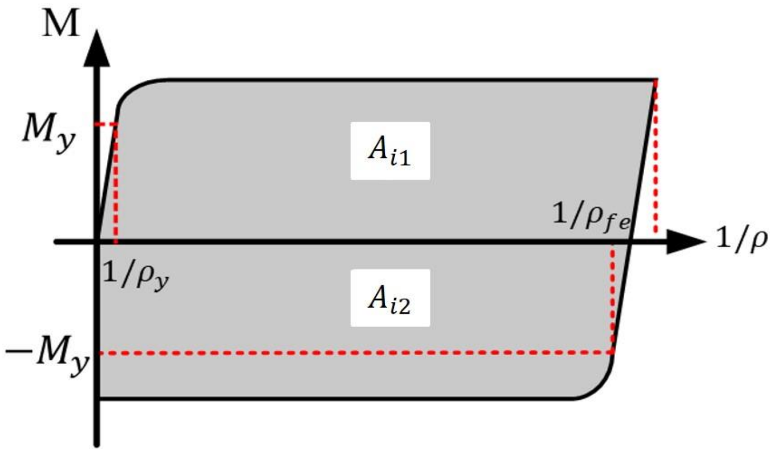

Figure 2-13 Schematic of the hooked segment slips in and out of the arched channel [47]

Here, the subscript i refers to the steel fiber passing through turning points 1 and 2. e_{p1} and e_{p2} are the plastic deformation energy of the steel fiber with a hooked end moving between these two turning points, respectively, and can be estimated as follows:

$$e_{P1} = A_{11} + A_{12} \tag{2-23}$$

$$e_{P2} = A_{21} + A_{22} \tag{2-24}$$

Based on the above equations and Figure 2-14, the relationship between the plastic deformation energy and the fiber sliding distance can be expressed as:

$$E_{P1}(\delta) = (e_{P1} + e_{P2})\delta, 0 \le \delta < l_{h1} \tag{2-25}$$

$$E_{P2}(\delta) = e_{P1} l_{h1} + e_{P2}\delta, l_{h1} \le \delta < l_{h2} \tag{2-26}$$

$$E_{P3}(\delta) = (e_{P1} + e_{P2}) l_{h1} + e_{P2} l_{h2}, l_{h1} + l_{h2} \le \delta < l_e \tag{2-27}$$

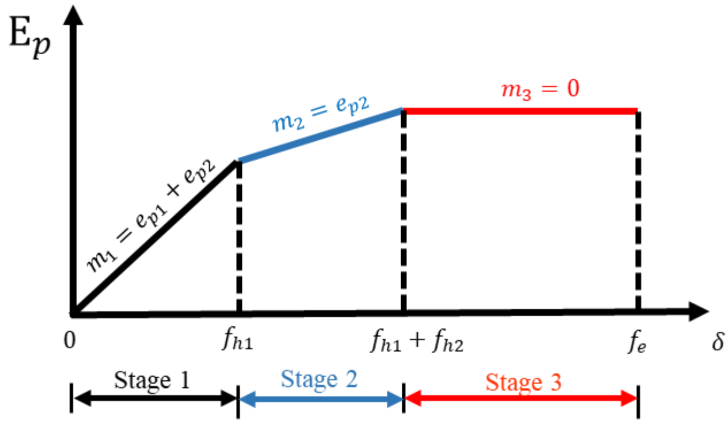

Figure 2-14 The E_P and δ relation during the fiber pullout process [47]

Total pullout energy can be calculated by the superposition principal as

$$g_{tP}(l_e, \delta, \beta) = g_f(l_e, \delta, \beta) + E_{Pi}(\delta) \tag{2-28}$$

Where the subscript i is the three stages of the pullout process.

2.5 Shear behavior of reinforced concrete

Shear behavior in reinforced concrete is a critical aspect of structural engineering that involves understanding how concrete structures resist and respond to shear forces. Proper reinforcement is necessary to manage shear stresses, control cracking, and prevent failure, ensuring the integrity and durability of concrete structures. Reinforced concrete members such as beam-column joint, deep beams, corbels, and shear walls are some of the examples.

2.5.1 Shear behavior of reinforced concrete deep beam

Reinforced concrete deep beams are structural elements with a small span-to-depth ratio. Due to this geometry, deep beams exhibit distinct shear behavior compared to slender beams. The pattern of failure in deep beams with and without fibers is shown in Figure 2-15.

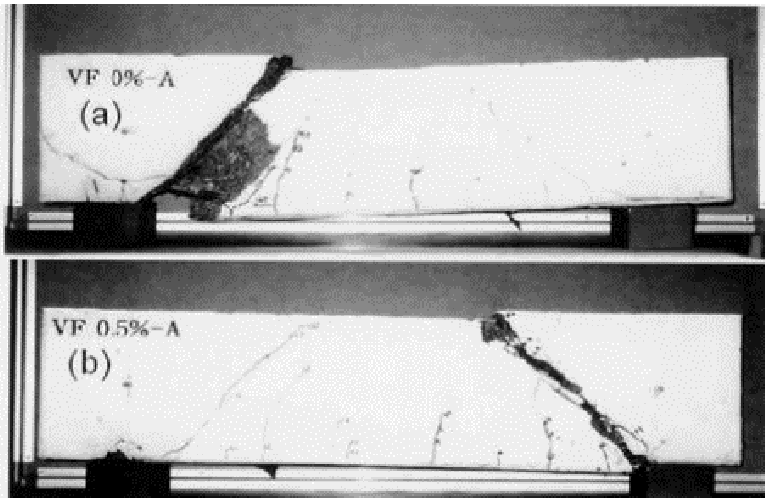

Deep beam failed in shear with 0% steel fibers (F30-0.0-13)

Deep beam failed in shear with 0.5% steel fibers (F30-0.5-13)

Figure 2-15 Failure pattern of RC and SFRC deep beams [52]

Apart from the traditional experimental ways for estimating the shear strength of reinforced concrete elements subjected to shear, some of the tests were carried out by using the panel element testing facility at the University of Toronto and suggested the Modified Compression Field Theory (MCFT) [14]. Moreover, the panel element testing facility was also used for assessing the SFRC panels to study their effectiveness as minimum shear reinforcement [7]. These panel test tests were conducted to understand the behavior of fiber-reinforced concrete (FRC) elements under pure shear loading and to facilitate the development of constitutive models that accurately characterize FRC shear behavior for improved design practices. This study also concluded that 1% of fibers are required to achieve satisfactory performance in shear. The pattern of failure of the RC panel with transverse reinforcement and SFRC panel with 0.5% fiber volume fraction without transverse reinforcement are indicated in Figure 2-16.

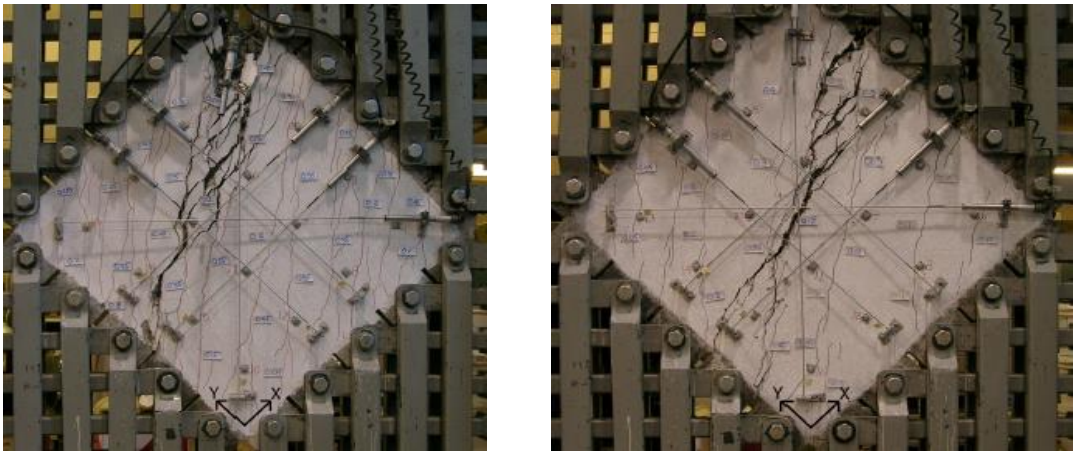

(a) RC Panels C1CR

(b) SFRC Panel C1F1V1 (0.5% steel fibers)

Figure 2-16 Failure crack pattern

2.5.2 The factors affecting the shear behavior of deep beams

According to the ACI-ASCE Committee, the shear strength of reinforced concrete beams is controlled by three factors: the strength of the concrete, the amount of longitudinal reinforcement, and the ratio of the shear span to the depth of the beam. These factors along with aggregate size and cross-sectional dimensions affecting the shear strength of RC beams are presented below.

doi:10.6342/NTU202403952

1. Compressive strength: The nominal shear strength of reinforced concrete is determined by the concrete compressive strength, the percentage of longitudinal reinforcement, and the shear-span-to-depth ratio. Consequently, an increase in the concrete's compressive strength results in an increase in its shear strength.
2. Steel reinforcement ratio: The impact of the steel reinforcement ratio on concrete shear strength is well established. A relatively high steel reinforcement ratio increases the shear strength due to enhanced dowel action and a deeper compression zone [53].
3. Aggregate size: It is commonly believed that using larger aggregate sizes in concrete enhances aggregate interlock. Aggregate interlock refers to the ability of a narrow, irregular crack to transfer load across the crack through contact between the exposed aggregate particles. Therefore, an increase in aggregate interlock leads to an increase in the shear strength of concrete.
4. Cross Section: Larger reinforced concrete cross-sections tend to develop more cracks, thereby reducing the concrete's shear strength. Minelli et al. [54] stated that incorporating steel fibers can mitigate this size effect on shear strength.
5. Shear span to effective depth ratio: The shear span-to-effective depth ratio has a considerable impact on the shear resistance of reinforced concrete beams. Literature shows that Beams with a lower shear span-to-depth ratio have the ability to withstand higher shear forces because of arch action. Arch action refers to the direct transmission of load to the support through a compressive strut [55].

2.6 D-Region Elements

The study of reinforced concrete (RC) structures under external loads, such as bending moments and shear forces, is based on three essential principles: force equilibrium, strain compatibility, and material constitutive laws. A common assumption in RC beam design is the applicability of the plane sections remain plane hypothesis for sections under bending. However, Saint-Venant's principle states that this assumption becomes invalid near points of concentrated loads, ends of column and beam, or abrupt change in geometry (Figure 2-17). In these "D-regions" (Disturbed or Discontinuity), the stresses and strain field becomes irregular (formation of bottle-shaped struts), and alternative analysis methods are required [4]. Conversely, in the surrounding "Bernoulli" regions (B-regions), the plane sections remain plane assumption remains valid.

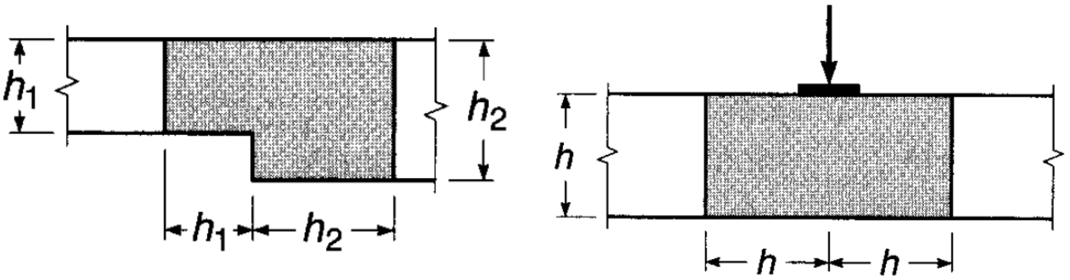

(a) Geometric discontinuity zone (b) Near concentrated load

Figure 2-17 Discontinuity regions in reinforced concrete [56]

2.6.1 Compression in Bottle-Shaped Struts

Several researchers have investigated the behavior of isolated bottle-shaped compression struts using direct compression tests on panel specimens [12,57–59]. These studies have provided valuable insights and recommendations on the aspect, such as the minimum amount of transverse steel reinforcement required for these struts to avoid splitting failure.

Sahoo et al. [58] developed a mathematical model to analyze dispersion of compression in a bottle-shaped strut. They used a square thin panel specimen with an aspect ratio of 1:1 and with varied concentration ratio (Different width of loading and supporting plate). Their model also considers the additional transverse tension generated in the bottle-shaped strut during the dispersion of compression. Based on the simplified linear distribution of transverse tensile stresses, the authors derived a formula to calculate this transverse tension. This formula is presented below:

$$m = \frac{P}{T'} = \frac{32}{15(1 - \frac{b}{a})} \tag{2-29}$$

m : slope of angle of dispersion of compression

P : applied in plane axial compression

T' : Transverse tensile force applied at the midpoint between the loaded and supported faces of the strut

b : width of the plate

a : total width of the specimen

Brown et al. [57] investigated the effect of transverse reinforcement on the compressive strength of bottle-shaped struts through testing square panel specimens (Figures 2-18 and 2-19). Figure 2-19 presents the reinforcement ratio on the horizontal axis, with higher ratios corresponding to the right side. The results also (Figure 2-19) demonstrate that the compressive strength of the struts did not exhibit a significant increase with increasing reinforcement ratio. In fact, some specimens even indicated a decrease in strength. Observations of the failure modes revealed crushing of the concrete near the loading or supporting plates in all specimens. Based on these findings, the authors suggest that increasing the transverse reinforcement ratio has minimal influence on the overall strength of the struts. The horizontal line in Figure 2-19 represents the design value for strut strength specified in Appendix A of ACI 318-02 [60]. It is evident that most tested specimens exceeded this minimum design value, suggesting that the current

doi:10.6342/NTU202403952

building code might provide conservative estimations for the compressive capacity of bottle-shaped struts.

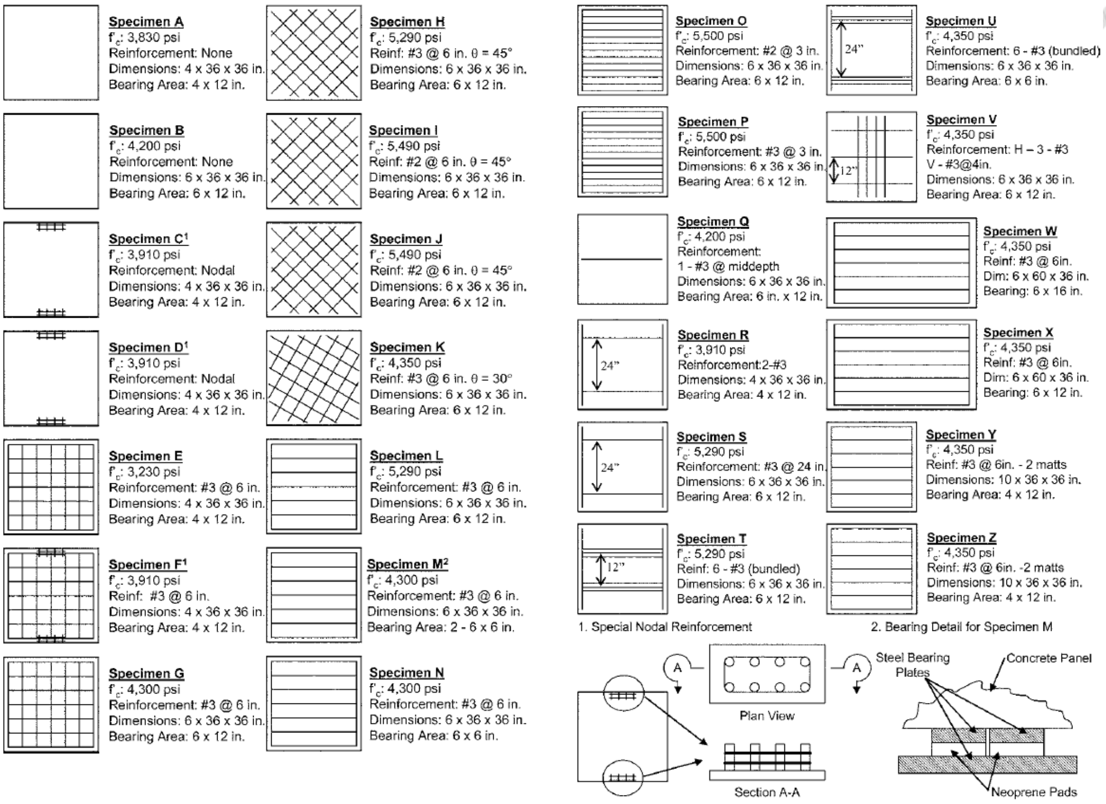

Figure 2-18 Panel Specimens with different reinforcement configuration [57]

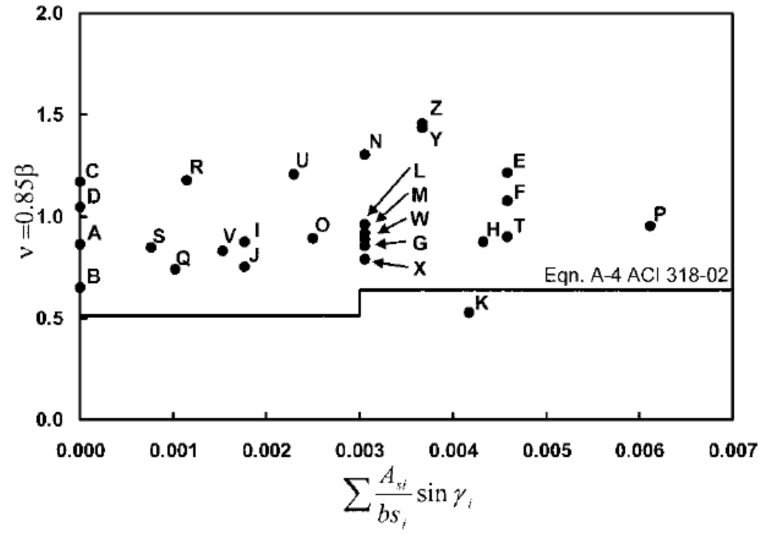

Figure 2-19 Comparison between isolated strut tests and ACI efficiency factor [57]

2.6.2 Strut-and-Tie Model

The strut-and-tie model (STM) effectively simulates the load transfer mechanism within D-regions, as illustrated in Figure 2-20. STM has become a tool to analyze the D-region, where shear deformations are dominant when compared with flexural deformations, and traditional Bernoulli-Euler beam theory is not valid. This model comprises three key components: compression struts, tension ties, and nodal zones [56]. Compression struts represent the flow of compressive forces within the concrete, while tension ties, typically composed of reinforcing steel bars, transmit tensile forces. These ties offer additional load paths for the member and contribute to confining the concrete. This confinement enhances the shear resistance of the concrete component.

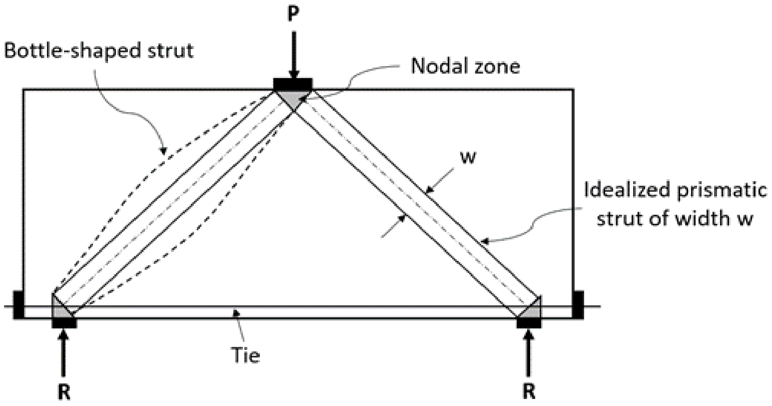

Figure 2-20 Representation of typical strut-and-tie model [56]

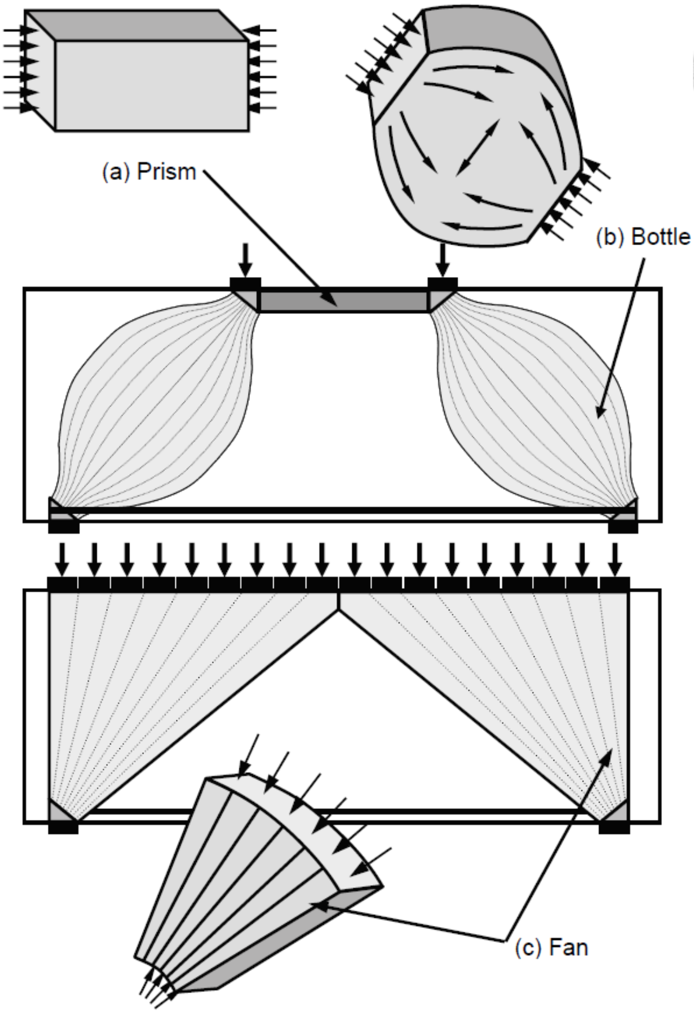

Figure 2-21 Types of struts [57]

Within the STM, the compression strut represents the path of compressive forces through the concrete. The direction of this strut aligns with the direction of the actual compressive stress field within the concrete member. The specific shape of the compression strut depends on the internal load transfer paths. An ideal case is a prismatic strut (Figure 2-21(a)), indicating a uniform distribution of compressive stress throughout the concrete. However, under the external loads on RC member, the actual distribution of stress field varies across the member's cross-section. This can lead to non-ideal shape of strut, such as a bottle-shaped strut (Figure 2-21(b)) where the stress field narrows towards

doi:10.6342/NTU202403952

the edges, or a fan-shaped strut (Figure 2-21(c)) where the stress field expands from a narrow section.

The bottle-shaped strut represents a compressive force path that concentrates towards the center of the member (Figure 2-21(b)). This concentration can induce lateral tensile forces perpendicular to the direction of compression, potentially causing splitting cracks in the central region. To mitigate these cracks, transverse reinforcing bars are typically placed within the center to resist the tensile forces. In contrast, Fan-shaped struts (Fig 2-21(c)) efficiently carry the load in members with uniform distribution, avoiding internal tensile stresses.

In a strut-and-tie model (STM), nodes represent the points where struts and ties intersect (Figure 2-22). The specific naming and behavior of a node depend on the types of struts and ties that intersect at the node. As shown in the Figure 2-22, 'C' represents a compression strut and 'T' represents a tension tie. However, regardless of the type of member (compression or tension) intersecting at the node, a state of static equilibrium has to be achieved on each load-bearing surface within the nodal zone.

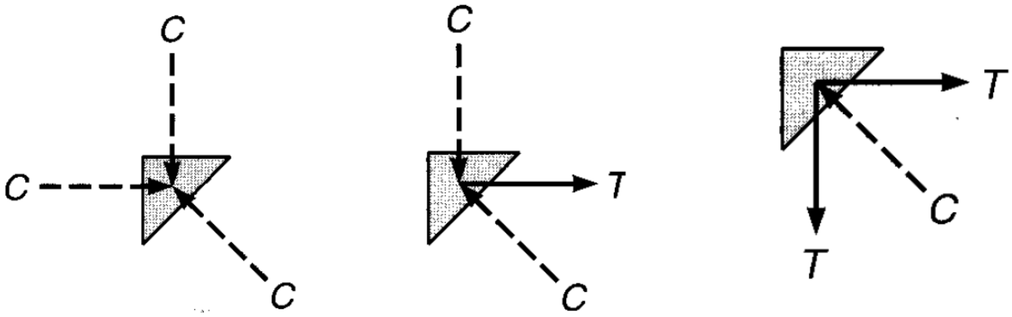

(a)C-C-C Node (b)C-C-T Node (c)C-T-T Node

Figure 2-22 Classification of Nodes [56]

doi:10.6342/NTU202403952

2.7 Review of shear analysis theories

2.7.1 Modified Compression Field Theory (MCFT)

The Modified Compression Theory effectively predicts the response of reinforced concrete panels subjected to in-plane shear and axial stresses [14]. Assuming the steel reinforcement has a perfect bond with the concrete, the compatibility criteria states that any deformation in the concrete must be equal to the deformation in the reinforcement. In simple terms, any alteration in the strain of the concrete will be accompanied by a proportional alteration in the strain of steel. Therefore:

$$\varepsilon_{sx} = \varepsilon_{cx} = \varepsilon_{x} \quad (2\text{-}30)$$

$$\varepsilon_{sy} = \varepsilon_{cy} = \varepsilon_{y} \quad (2\text{-}31)$$

The forces applied to a reinforced concrete element are resisted by the stresses in both the concrete and the reinforcement, which can be expressed as follows:

$$f_x = f_{cx} + \rho_{sx} f_{sx} \quad (2\text{-}32)$$

$$f_y = f_{cy} + \rho_{sy} f_{sy} \quad (2\text{-}33)$$

$$v_{xy} = v_{cx} - \rho_{sx} v_{sx} \quad (2\text{-}34)$$

$$v_{xy} = v_{cy} - \rho_{sy} v_{sy} \quad (2\text{-}35)$$

The relationship between the average principal tensile stress and the average principal tensile strain in concrete is nearly linear until cracking occurs, after which the principal tensile stress decreases. Thus, as indicated in Figure 2-23 the relationship before and after cracking is suggested as follows:

doi:10.6342/NTU202403952

$$f_{c1} = E_c \epsilon_1 \text{ for } \epsilon_1 \leq \epsilon_{cr} \text{ (Ascending Branch)} \tag{2-36}$$

$$f_{c1} = \frac{f_{cr}}{1+\sqrt{200\varepsilon_1}} \text{ for } \epsilon_1 > \epsilon_{cr} \text{ (Strain softening Branch)} \tag{2-37}$$

Where, $f_{cr} = 0.33\sqrt{f_c'}$ (MPa) (-ve for compression)

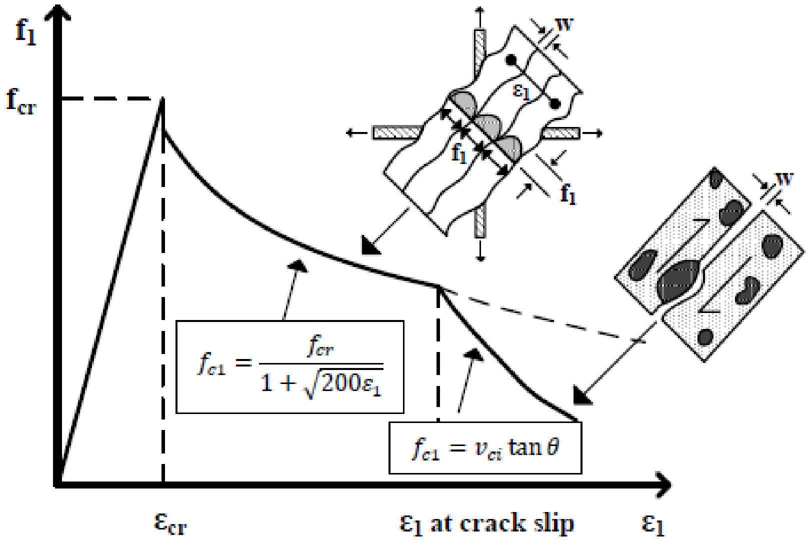

Figure 2-23 Average stress-strain relationship for cracked concrete in tension [61]

Vecchio and Collins [14] state that the tensile stresses in a steel bar are above average at a crack and below average between cracks. Conversely, the tensile stresses in the concrete are zero at a crack and above average between cracks. Figure 2-24 illustrates the difference between the calculated average stress and the actual local stresses at a crack.

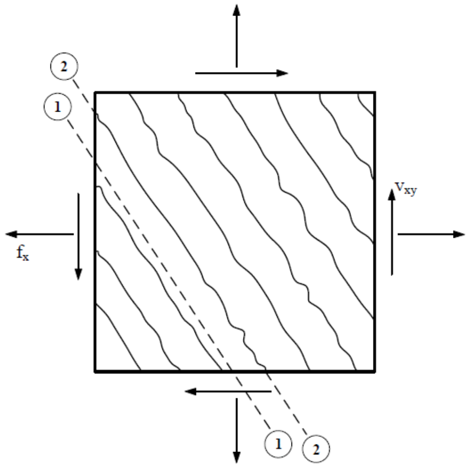

(a) Stress applied to cracked element

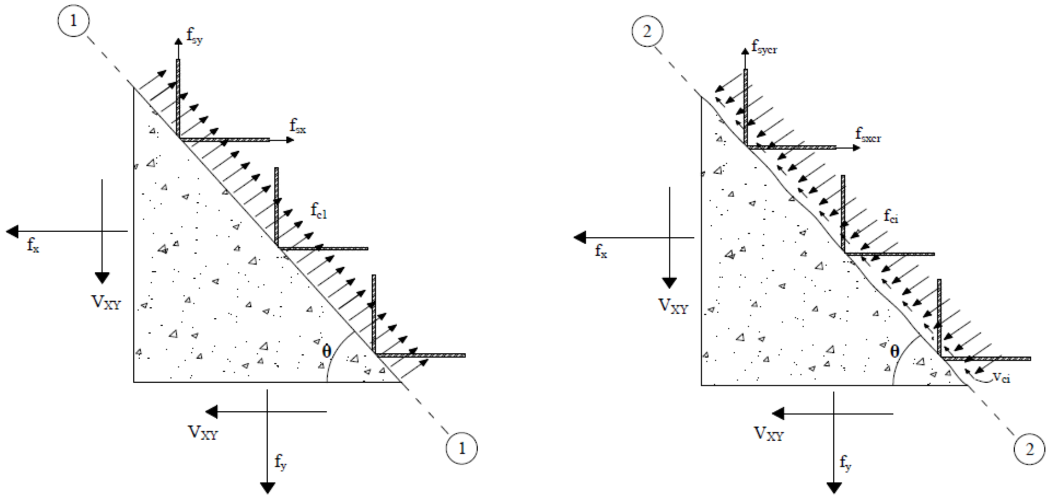

(b) Calculated average stresses (c) Local stresses at a crack

Figure 2-24 Comparison of Local Stresses at Crack with Calculated Average Stresses [14]

The applied stresses f_x, f_y, and v_{xy} are constant. The two sets of stresses in Figure 2-24 need to be statically equivalent. The condition for the two sets of stresses resulting in equal forces in the x and y directions, assuming a unit area for both plane 1 and plane 2, is:

$$\rho_{sx}(f_{sxcr} - f_{sx}) = f_{c1} + f_{ci} + v_{ci}/\tan\theta \tag{2-38}$$

$$\rho_{sy}\left(f_{sycr} - f_{sy}\right) = f_{c1} + f_{ci} + v_{ci}\tan\theta \tag{2-39}$$

However, the stress in the reinforcement at a crack cannot exceed the yield strength.

According to Walraven [62], the shear transfer along the crack because of the aggregate interlock is calculated as follows:

$$v_{ci} = 0.18v_{cimax} + 1.64f_{ci} - 0.82\frac{f_{ci}^2}{v_{cimax}} \tag{2-40}$$

$$v_{cimax} = \frac{\sqrt{-f_c'}}{0.31 + 24w/(a + 16)} \tag{2-41}$$

In MCFT, the softening of concrete is considered by the following equations

$$f_{c2} = f_{c2max}\left[\frac{2\epsilon_2}{\epsilon_c'} - \left(\frac{\epsilon_2}{\epsilon_c'}\right)^2\right] \tag{2-42}$$

Where, $$f_{c2max} = \frac{f_c'}{0.8 - 0.34\left({\epsilon_1}/{\epsilon_c'}\right)} \leq 1.0 \tag{2-43}$$

2.7.2 Softened Strut-and-Tie Model (SST)

1. Background

The Softened Strut-and-Tie Model (SST) is an advanced analytical approach used to predict the shear strength of reinforced concrete (RC) elements, especially in regions where complex stress distributions occur, such as near discontinuities (D-Regions) as shown in Figure 2-25. This model addresses the limitations of traditional strut-and-tie models in capturing the effects of concrete softening. The SST uses a truss analogy where concrete compressive members (struts) and steel tensile members (ties) are modeled as a network, interconnected at the nodes. SST is formulated upon force equilibrium, constitutive laws of materials and strain compatibility.

doi:10.6342/NTU202403952

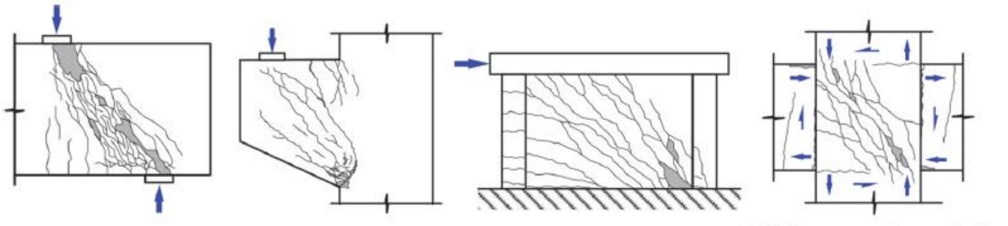
(a) Deep beam (b) Corbel (c) Squat wall (d) Beam-column joint

Figure 2-25 RC D-Region elements failing in Diagonal Compression [63]

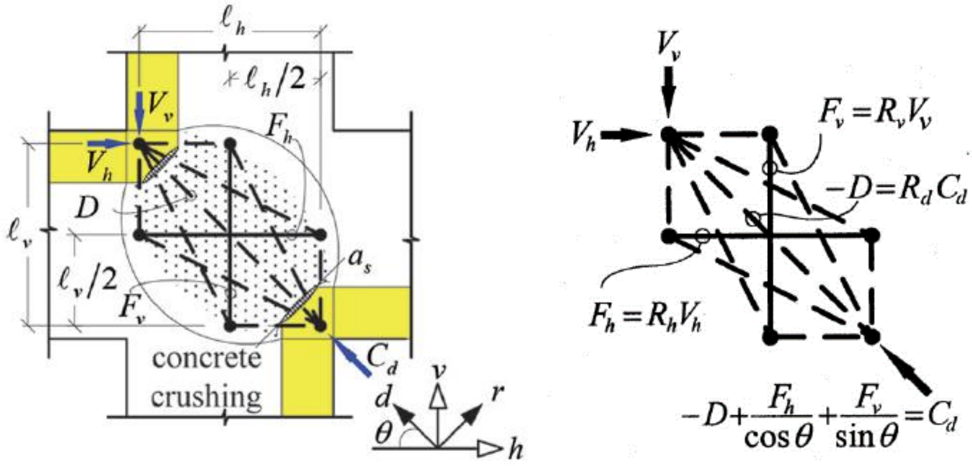

Figure 2-26 Demonstration of Softened Strut-and-Tie Model with its idealization [63,64]

Based on the demonstration of SST model in Figure 2-26 the angle of inclination of the diagonal compressive strut with respect to horizontal h axis is expressed as:

$$\theta = tan^{-1}\left(\frac{l_v}{l_h}\right) \tag{2-44}$$

2. Force Equilibrium

The diagonal compression, denoted as C_d, is determined by the compressive force in the diagonal strut (D, negative in compression) and the tensile forces in the horizontal and vertical ties F_h and F_v, as illustrated in Figure 2-26 Therefore, C_d can be represented as:

doi:10.6342/NTU202403952

$$C_d = -D + \frac{F_h}{\cos\theta} + \frac{F_v}{\sin\theta} \tag{2-45}$$

The compressive strength of diagonal strut is given by

$$C_{d,n} = K\zeta f_c' A_{str} \tag{2-46}$$

Therefore, to provide a clearer understanding of the proportions of each mechanism, the ratios for each mechanism are assumed to be

$$-D\colon \frac{F_h}{\cos\theta}\colon \frac{F_v}{\sin\theta} = R_d\colon R_h\colon R_v \tag{2-47}$$

Where R_d, R_h and R_v represent the ratios of diagonal compression that are resisted by the diagonal, horizontal, and vertical mechanisms, respectively. Furthermore, as stated by Schäfer [65] and Jennewein and Schäfer [66], the amount of the diagonal compression transmitted by the horizontal tie (γ_h) is defined as

$$\gamma_h = \frac{2\,tan\theta - 1}{3} \text{ for } 0 \le \gamma_h \le 1 \tag{2-48}$$

Similarly, the fraction of diagonal compression carried by the vertical tie is defined as

$$\gamma_v = \frac{2\,cot\theta - 1}{3} \text{ for } 0 \le \gamma_v \le 1 \tag{2-49}$$

The ratio between the horizontal and diagonal mechanisms, or vertical and diagonal mechanisms can be calculated as

$$R_h\colon R_d = \gamma_h\colon (1 - \gamma_h) \tag{2-50}$$

$$R_v\colon R_d = \gamma_v\colon (1 - \gamma_v) \tag{2-51}$$

Relative stiffness ratio can be evaluated as follows:

$$R_h = \frac{\gamma_h(1 - \gamma_v)}{1 - \gamma_h\gamma_v} \tag{2-52}$$

$$R_v = \frac{\gamma_v(1 - \gamma_h)}{1 - \gamma_h\gamma_v} \tag{2-53}$$

$$R_d = \frac{(1-\gamma_h)(1-\gamma_v)}{1-\gamma_h\gamma_v} \tag{2-54}$$

These ratios are evaluated after equaling their sum to unity i.e. $R_h + R_v + R_d = 1$. Based on the above equations the relationship between relative stiffness ratio and θ is described in the following Figure 2-27.

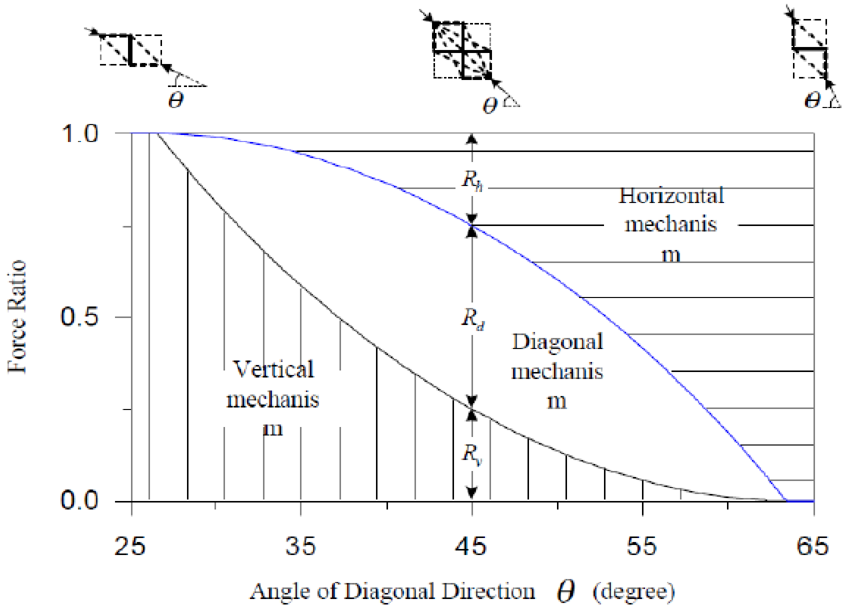

Figure 2-27 Distribution of force between R_h, R_v, R_d mechanisms [42]

By determining all the forces, the maximum compressive stress $\sigma_{d,max}$ (negative in compression), which serves an integral part in establishing the failure condition of a joint, can be derived by

$$-\sigma_{d,max} = \frac{1}{A_{str}}\left[-D + \frac{F_h}{\cos\theta_f}\cos\left(\theta-\theta_f\right) + \frac{F_v}{\sin\theta_s}\cos(\theta_s-\theta)\right] \tag{2-55}$$

Where, A_{str} is defined as $A_{str} = a_s \times b_s$.

Since, $2\tan\theta_f = \tan\theta$ and $\tan\theta_s = 2\tan\theta$, the above Eq. (2-55) becomes

$$-\sigma_{d,max} = \frac{1}{A_{str}}\left[-D + \frac{F_h}{\cos\theta}\left(1-\frac{sin^2\theta}{2}\right) + \frac{F_v}{\sin\theta}\left(1-\frac{cos^2\theta}{2}\right)\right] \tag{2-56}$$

Eq. (2-56) demonstrates the maximum compressive stress of diagonal strut as the combined result of the compressive resistance from diagonal strut and the fraction of the forces from tension ties. It is evident that horizontal ties and vertical ties provide another force flow to distribute the forces transferring to the diagonal strut.

3. Average principal tensile strain

To satisfy the compatibility, ε_r, the principal tensile strain, is determined by the equation of the first strain invariant Figure 2-28, that is

$$\varepsilon_r + \varepsilon_d = \varepsilon_h + \varepsilon_v \tag{2-57}$$

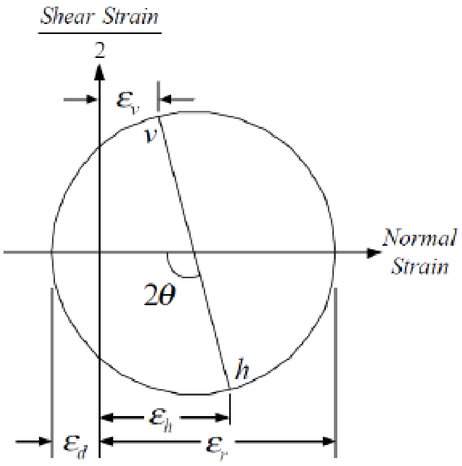

Figure 2-28 Mohr's Circle of average strains

Therefore, to maintain simplicity, it is assumed that ε_h and ε_v are both lower than the yielding strain of the reinforcement. However, in the absence of horizontal or vertical reinforcement, the concrete is responsible for withstanding the tensile stress until cracks form. Thus, ε_h and ε_v are taken to equal 0.002, which is the cracking strain of normal concrete. This conservative assumption is made to represent the average normal strains for joints, regardless of whether they have horizontal or vertical mechanisms. Furthermore, it is assumed that ε_d has a value of -0.001 when concrete undergoes failure due to crushing. Based on the factors described before, the value of ε_r can be simplified to 0.005.

4. Strut-and-tie index

With the presence of horizontal and vertical tie in the discontinuity region, ties will contribute to diagonal strut, which activates more concrete in shear resistance. This can be represented in strut-and-tie index (*K*) and can be defined as,

$$
\begin{aligned}
K &= \frac{C_d}{-\sigma_{d,\max} \times A_{\mathrm{str}}} \\
&= \frac{-D + \dfrac{F_h}{\cos\theta} + \dfrac{F_v}{\sin\theta}}{-D + \dfrac{F_h}{\cos\theta}\left(1 - \dfrac{\sin^2\theta}{2}\right) + \dfrac{F_v}{\sin\theta}\left(1 - \dfrac{\cos^2\theta}{2}\right)} \geqslant 1
\end{aligned}
\tag{2-58}
$$

Since there are four different combinations of resisting mechanisms in a joint, the strut-and-tie index *K* must be determined for each combination individually, as stated by Hwang & Lee [16,17]:

- **Diagonal Mechanism:** Diagonal compression is resisted only by the diagonal strut. Given this condition, the diagonal strut-and-tie index, represented as K_d

$$K_d = -D/-D \tag{2-59}$$

- **Diagonal plus horizontal mechanism:** With the presence of horizontal tie (Reinforcement), more flat sub-strut are formed, and the stresses are deviated away from the angle of inclination of the strut. For the condition where, the failure of diagonal compressive strut and yielding of the horizontal reinforcement occurs simultaneously, also referred as the balanced horizontal strut-and-tie index $\overline{K_h}$ is defined as

$$\overline{K_h} = \frac{(1-\gamma_h)+\gamma_h}{(1-\gamma_h)+\gamma_h(1-\frac{sin^2\theta}{2})} \geq 1 \qquad (2\text{-}60)$$

The balanced amount of tie force at which the horizontal tie reinforcement reaches yielding at failure can be calculated by the following Eq. (2-61) and Figure 2-29

$$\overline{F_h} = \gamma_h \times (\overline{K_h}\zeta f_c' A_{str}) \times cos\theta \qquad (2\text{-}61)$$

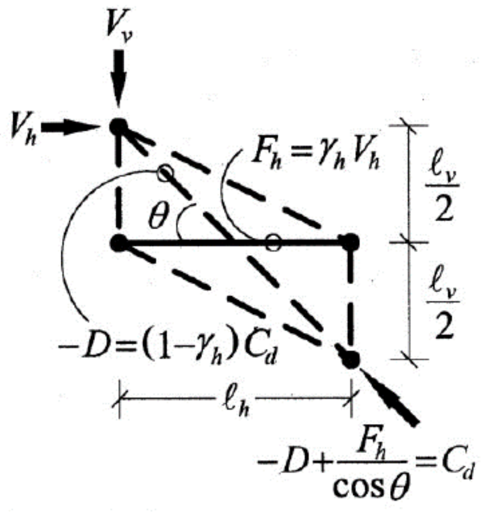

Figure 2-29 Joint shear resistance by diagonal and horizontal mechanism

By using the balanced amount of horizontal tie force, the horizontal tie index K_h for the under-reinforced case can be approximated by linear interpolation:

$$K_h = 1 + (\overline{K_h} - 1)\left(F_{yh}/\overline{F_h}\right) \leq \overline{K_h} \qquad (2\text{-}62)$$

Where F_{yh} is equal to $A_{th}f_y$, in which A_{th} is the amount of horizontal reinforcement.

- **Diagonal plus Vertical Mechanism:** On the same lines with the previous case, the strut-and-tie index $\overline{K_v}$, and the balanced amount of vertical tie force $\overline{F_v}$, and vertical tie index, can be estimated as follows:

$$\overline{K_v} = \frac{(1-\gamma_v)+\gamma_v}{(1-\gamma_v)+\gamma_v(1-\frac{cos^2\theta}{2})} \geq 1 \tag{2-63}$$

$$\overline{F_v} = \gamma_v \times (\overline{K_v}\zeta f_c' A_{str}) \times sin\theta \tag{2-64}$$

$$K_v = 1 + (\overline{K_v}-1)\left(F_{yv}/\overline{F_v}\right) \leq \overline{K_v} \tag{2-65}$$

- **Complete Mechanism:**

As indicated in Figure 2-26 with presence of both horizontal and vertical tie, more flatter and steeper struts are formed which deviates the flow of forces away from the axis of the diagonal strut. This makes concrete less susceptible to crushing. Therefore, the increase in shear strength resulting from the contribution of these tension ties can be determined by

$$\overline{K} = \frac{R_h + R_v + R_d}{R_d + \ R_h\left(1-\frac{sin^2\theta}{2}\right) + R_v\left(1-\frac{cos^2\theta}{2}\right)} \geq 1 \tag{2-66}$$

Where, $\overline{K}$ = is a strut-and-tie index with sufficient horizontal and vertical ties.

5. Simplified Softened Strut-and-Tie Model

Hwang and Lee [64] simplified the softened-strut-and tie model to maintain its distinct advantage of simplicity. Therefore, the balanced strut-and-tie index $(\overline{K})$, and strut-and-tie index (K) is simplified as:

$$\overline{K} = K_d + (\overline{K_h}-1) + (\overline{K_v}-1) = \overline{K_h} + \overline{K_v} - 1 \tag{2-67}$$

$$K = K_d + (K_h-1) + (K_v-1) = K_h + K_v - 1 \tag{2-68}$$

doi:10.6342/NTU202403952

2.7.3 Softened Membrane Model (SMM) by Hsu & Zhu (2002) and it's modification for UHPC by Shahin et al. (2024)

SMM is a rational theory which is based on Navier's three principles of mechanics of materials includes stress equilibrium, strain compatibility and material constitutive laws, to predict the entire shear behavior of membrane elements including post-peak response. Unlike MCFT which is a rotating angle shear theory, SMM is a fixed angle shear theory. This theory also considers the Poisson effect i.e. the effect of two normal strains which is characterized by Hsu/Zhu ratio.

1. **Strain compatibility equations**

Assuming the direction of principal stresses coincide with the direction of principal biaxial strain According to Pang & Hsu [67], the equations for strain compatibility are given as follows:

$$\overline{\varepsilon_l} = \overline{\varepsilon_1} cos^2\alpha_1 + \overline{\varepsilon_2} sin^2\alpha_1 - \frac{\gamma_{12}}{2} \times 2 \times \sin\alpha_1 \cos\alpha_1 \qquad (2\text{-}69)$$

$$\overline{\varepsilon_t} = \overline{\varepsilon_1} sin^2\alpha_1 + \overline{\varepsilon_2} cos^2\alpha_1 + \frac{\gamma_{12}}{2} \times 2 \times \sin\alpha_1 \cos\alpha_1 \qquad (2\text{-}70)$$

$$\frac{\gamma_{lt}}{2} = (\varepsilon_1 - \varepsilon_2) \sin\alpha_1 \cos\alpha_1 + \frac{\gamma_{12}}{2} (cos^2\alpha_1 - sin^2\alpha_1) \qquad (2\text{-}71)$$

Where the angle α_1 is indicated in the Figure 2-30

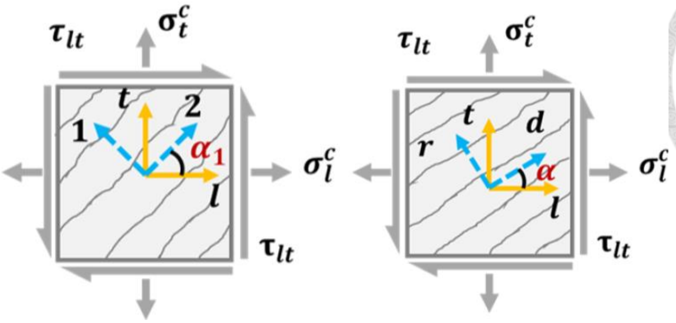

Figure 2-30 Transformation angle between *1-2* and *d-r* with *l-t* coordinate system [68]

2. Equilibrium stress state

Equilibrium equations for SMM are derived as follows, after the coordinate transformation of stresses and strains in concrete from *1-2* coordinate to *l-t* coordinate, using the angle α_1, as defined schematically in Figure 2-30

$$\sigma_l = \sigma_1^c cos^2\alpha_1 + \sigma_2^c sin^2\alpha_1 - \tau_{12}^c 2\ sin\alpha_1 cos\alpha_1 + \rho_l f_l \tag{2-72}$$

$$\sigma_t = \sigma_1^c sin^2\alpha_1 + \sigma_2^c cos^2\alpha_1 + \tau_{12}^c 2\ sin\alpha_1 cos\alpha_1 + \rho_t f_t \tag{2-73}$$

$$\tau_{lt} = (\sigma_1^c - \sigma_2^c) sin\alpha_1 cos\alpha_1 + \tau_{12}^c (cos^2\alpha_1 - sin^2\alpha_1) \tag{2-74}$$

3. Constitutive laws of materials

- **Concrete in compression**

Based on the average compressive stress-strain curve of concrete, the constitutive laws for concrete in compression are given as:

$$\sigma_2^c = \zeta f_c' \left[2\left(\frac{\bar{\varepsilon}_2}{\zeta\varepsilon_0}\right) - \left(\frac{\bar{\varepsilon}_2}{\zeta\varepsilon_0}\right)^2\right] \text{ for } \bar{\varepsilon}_2/\zeta\varepsilon_0 \le 1 \tag{2-75}$$

$$\sigma_2^c = \zeta f_c' \left[1 - \left(\frac{(\bar{\varepsilon}_2/\zeta\varepsilon_0) - 1}{(4/\zeta) - 1}\right)^2\right] \text{ for } \bar{\varepsilon}_2/\zeta\varepsilon_0 > 1 \tag{2-76}$$

$$\beta = \frac{1}{2}\tan^{-1}\left[\frac{\gamma_{12}}{\varepsilon_1 - \varepsilon_2}\right] \tag{2-77}$$

$$\zeta = min\left(\frac{5.8}{\sqrt{f_c'}}, 0.9\right) \times \frac{1}{\sqrt{1 + 400\overline{\varepsilon_1}}} \times \left(1 - \frac{|\beta|}{24°}\right) \tag{2-78}$$

Where, ζ representing softening coefficient in concrete to account for the biaxial stress state and β is the deviation angle between the *1-2* and *d-r* coordinate system.

- **Concrete in tension**

Based on average stress-strain curve of concrete in tension, Pang & Hus [67] proposed the following equations, the Eq. (2-79) indicate the initial linear ascending branch up to concrete cracking and followed by non-linear descending branch as indicated in Eq. (2-80) below,

$$\sigma_1^c = E_c\overline{\varepsilon_1} \text{ for } \overline{\varepsilon_1} \le \varepsilon_{cr} \tag{2-79}$$

$$\sigma_1^c = f_{cr}\left(\frac{\varepsilon_{cr}}{\overline{\varepsilon_1}}\right)^{0.4} \text{ for } \overline{\varepsilon_1} > \varepsilon_{cr} \tag{2-80}$$

- **Concrete in shear**

The Eq. (2-81) represents the analytical shear stress-strain representation of concrete. This relationship is formulated by assuming that the direction of principal tensile stress and strain in concrete coincide with each other.

$$\tau_{12}^c = \frac{\sigma_1^c - \sigma_1^c}{2(\overline{\varepsilon_1} - \overline{\varepsilon_2})}\gamma_{12} \tag{2-81}$$

- **Mild steel**

Derived from the typical stress-strain relationship of a mild steel bar that is embedded within concrete is formulated with Eq. (2-82) and (2-83). At the location of crack, stresses in the reinforcing bar are more as compared with the uncracked regions; and following equations considers this effect.

$$f_l = E_s \overline{\varepsilon_l} \text{ (Before Yielding)} \tag{2-82}$$

$$f_l = (0.93 - 2B) f_{ly} + (0.02 + 0.25B) E_l \overline{\varepsilon_l} \text{ (After Yielding)} \tag{2-83}$$

$$\text{Where, } B = \frac{1}{\rho_l} \left(\frac{f_{cr}}{f_{ly}} \right)^{1.5}$$

On the similar parameters, f_t can be calculated.

2.8 Shear Strength Prediction Formula for SFRC

2.8.1 Deep Beams

- **Narayanan and Darwish (1988)**

Narayanan and Darwish [13] proposed the shear strength prediction equation which consists of three terms. The first term accounts for the contribution of fiber concrete to the overall shear and is expressed in relation to the computed split cylinder strength, f_{spfc}.

$$f_{spfc} = \frac{F_{cuf}}{A} + B + C\sqrt{F} \tag{2-84}$$

Where,

A : a non-dimensional constant, A=20−$\sqrt{F}$

F : fiber factor, $F = \left(\frac{l_f}{d_f} \right) V_f \beta$

B: a dimensional constant, B=0.7 (MPa) for crimped and hooked end fibers

C: a dimensional constant, C=1 (MPa)

The second term takes into account the dowel action, which is determined by the quantity of tensile reinforcement and the shear span ratio. The final term consider the influence of the fiber pull-out stresses acting along the inclined crack. Hence Narayanan and Darwish [13] revealed the following formula to predict the ultimate shear strength of fiber reinforced concrete, where τ_f accounting for the bond factor and ρ_{st} considers the effect of longitudinal reinforcement ratio:

$$v_u = 2.8\frac{d}{a}\left(0.24f_{spfc} + 80\rho_{st}\frac{d}{a}\right) + 0.41\tau_f F\ (MPa) \tag{2-85}$$

- **Ashour et al. (1992)**

Ashour et al. [53] tested 18 beams of high strength fiber reinforced concrete. Based on the test result, two equations to predict the shear strength was proposed. The first equation was similar to Zsutty [69]. The modification of Zsutty [69] was made by include the extra strength provided by fibers represented as factor F:

$$v_u = \left(2.11\sqrt[3]{f_c'} + 7F\right)\left(\rho_{st}\frac{d}{a}\right)^{0.333}\quad (MPa)\ \frac{a}{d} > 2.5 \tag{2-86}$$

$$v_u = \left[\left(2.11\sqrt[3]{f_c'} + 7F\right)\left(\rho_{st}\frac{d}{a}\right)^{0.333}\right]\left(\frac{2.5}{a/d}\right) + v_b\left(2.5 - \frac{a}{d}\right)(MPa)\ \frac{a}{d} < 2.5 \tag{2-87}$$

For beams with depth $\frac{a}{d} < 2.5$, an additional resistive component v_b is included by the shear strength of the fiber, is added to the original strength. According to Ashour et al. [53], the additional strength component is considered in the overall strength calculation, and the increased strength resulting from a decreased shear-span to depth ratio is applied to the sum. The second equation was modification of the ACI Building Code equation. The equation was revised by including the influence of the shear-span/depth ratio on both the concrete and the longitudinal reinforcement.

$$v_u = \left(0.7\sqrt{f_c'} + 7\mathrm{F}\right)\frac{d}{a} + 17.2\rho_{st}\frac{d}{a}\ (MPa) \tag{2-88}$$

The fiber factor F is the same as other proposed equation uses. The multiplier of 0.7 reflects the behavior of high strength concrete.

- **Khuntia et al. (1990)**

Khuntia et al. [70], suggest that by analyzing the forces at a diagonal crack in SFRC without stirrups and assuming a 45° crack inclination, the total shear resistance of SFRC is the combined shear contributions from both the concrete and the fibers. The fiber contribution can be represented as:

$$V_{fr} = 0.9db_w \times \sigma_{pc} = 0.25F_1\sqrt{f_C'}b_w d \tag{2-89}$$

Where,

$F1$ =Fiber factor, $F_1 = \beta V_f\left(\frac{l_f}{d_f}\right)$

β = the factor for fiber shape and concrete type, is assigned a value of 1 for hooked or crimped steel fiber, 2/3 for plain or round steel fiber with normal concrete, 3/4 for hooked or crimped steel fibers with lightweight concrete.

In addition, the concrete contribution involves the resistance of compressed concrete, aggregate interlock, and dowel action of reinforcement, which were assumed to be equal ACI Building Code Equation:

$$V_c = 0.167\sqrt{f_C'}b_w d \tag{2-90}$$

Hence, in general the ultimate shear resistance of SFRC expressed as:

$$v_u = \left(0.418\frac{d}{a} + 0.25\,F\right)\sqrt{f_c'}\ \text{ when, } 0.5 < \frac{a}{d} < 2.5 \tag{2-91}$$

2.8.2 Beam-Column Joints

- **Shear Resistance Mechanism in SFRC Beam-Column Joint**

Jiuru et al. [71] introduced a model to predict the shear strength of SFRC joints. The model is based on the mechanism of shear resistance as depicted in Figure 2-31.

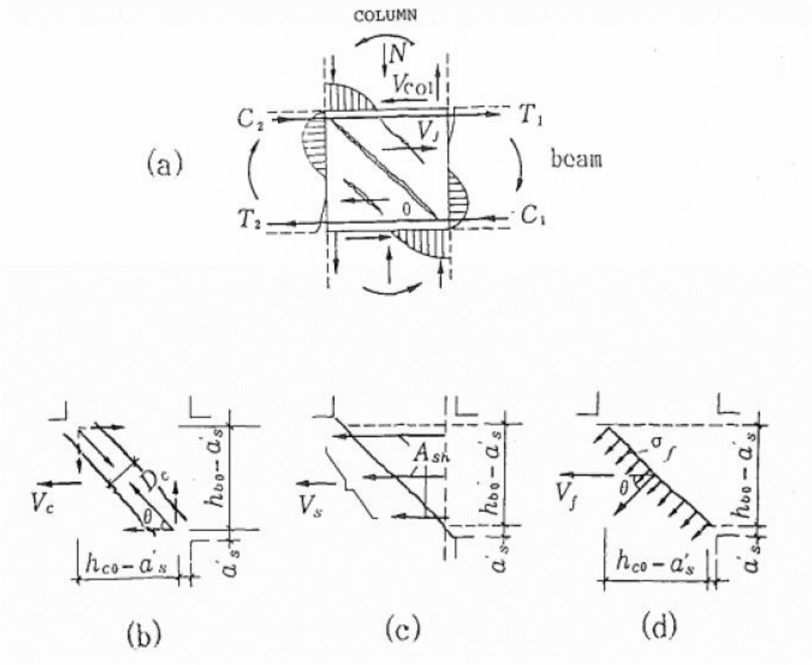

Figure 2-31 Shear resistance mechanism of SFRC joints [71]

The shear resistance offered by steel fiber concrete is denoted as V_{sf}. This is because steel fiber concrete retains a significant amount of tensile stress even after cracks have formed. This can be illustrated by a typical stress-displacement curve for steel fiber reinforced concrete (SFRC), as shown in Figure 2-32 [72]. The model incorporates the shear resistances from concrete, transverse reinforcement (stirrup), and steel fibers to determine the ultimate shear strength of SFRC joints, denoted as V_j.

$$V_j = V_c + V_{sf} + V_s \tag{2-92}$$

Where V_c is defined as

$$V_c = 0.1\left(1 + \frac{N}{b_c h_c f_c}\right) b_j h_j f_c' \tag{2-93}$$

And V_s is derived to be

$$V_s = f_y \frac{A_{sh}}{S}(h_o - a_s') \tag{2-94}$$

The equation represents the relationship between the spacing of stirrups S, the effective depth of the beam h_o, and the distance from the extreme compressive fiber to the centroid of the compressive reinforcement a_s'. In addition, based on the test findings obtained from the research, the value of V_{sf} is determined as

$$V_{sf} = 2\left(\frac{l_f}{d_f}\right)V_f b_j h_j \tag{2-95}$$

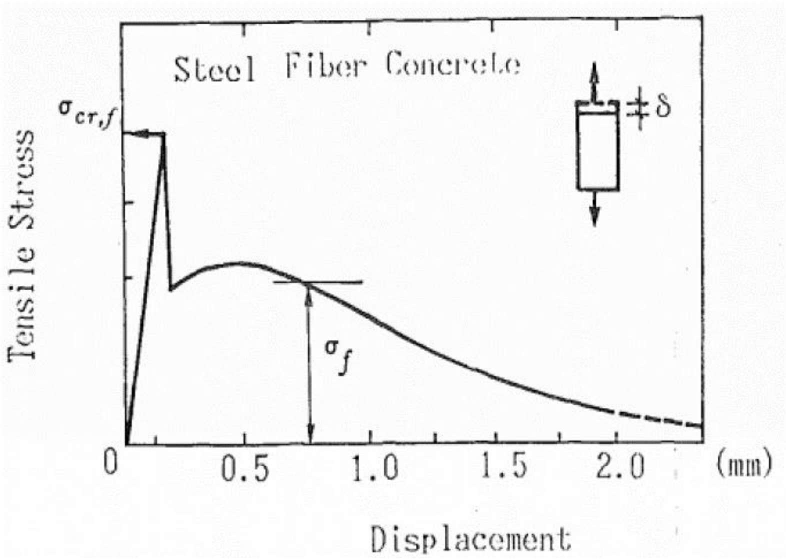

Figure 2-32 Typical tensile stress versus displacement curve of steel fiber concrete [72]

2.9 Summary of Literature Review

This literature review provides a comprehensive overview of the mechanical behavior and analysis methods for reinforced concrete (RC) and steel fiber reinforced concrete (SFRC) elements, particularly focusing on shear behavior and analysis of discontinuity regions.

The review begins by comparing the compressive and tensile behaviors of normal concrete and steel fiber reinforced concrete (SFRC). The inclusion of steel fibers does not significantly enhance compressive strength, typically resulting in only a 0-15% increase. However, it greatly improves tensile strength, and significantly enhances post-cracking performance. SFRC demonstrates superior toughness, ductility, bond strength, and crack control compared to plain concrete. Additionally, the steel fiber pull-out behavior and the softening effect in cracked reinforced concrete (RC) elements, both of which are crucial for understanding the post-cracking performance of SFRC, are addressed.

A significant portion of the review is dedicated to the behavior of discontinuity (D) regions in RC structures. The strut-and-tie model (STM) is presented as an effective tool for analyzing these regions. The literature review then focuses on analytical approaches for predicting the shear behavior of D-region elements, such as Modified Compression Field Theory (MCFT), Softened Strut-and-Tie Model (SST), and Softened Membrane Model (SMM). This chapter also discusses the detailed processes behind their development. It is evident that these models do not consider the influence of fiber addition. To address this limitation, this study modifies two existing analytical models: MCFT and SST. The development of Modified Compression Field Theory and Softened Strut-and-Tie Model for SFRC is discussed in the subsequent chapters.

doi:10.6342/NTU202403952

Chapter 3 Development of Modified compression Field Theory for SFRC

3.1 Introduction

Modified Compression Field Theory (MCFT) by Vecchio & Collins (1986) [14] was founded upon Compression Field Theory (CFT) by Collins, (1978) and Mitchell & Collins (1974) [73,74]; and was developed using the shear panel test facility at the University of Toronto. In order to develop it, several reinforced concrete panels are tested under different loading conditions like pure shear, uniaxial compression, or a combination of shear and biaxial stresses. With the key assumption that, in concrete, the direction of principal stress corresponds with the direction of principal strain. The MCFT is based on compatibility, equilibrium, and constitutive laws of materials. The fractured concrete is also taken into account by MCFT as a unique orthotropic material with special properties that have a significant impact on the predicted shear stress-strain response. A analysis method for computing this stress-strain response of the loaded elements is part of analysis based on MCFT.

Using modified compression field theory, the experimental and analytical responses of SFRC shear panel specimens is compared in this work. Normal concrete indicated strain softening behavior which is considered in in the formulation of MCFT. However, SFRC indicated strain hardening behavior which is taken into account in the proposed analysis method by changing the material constitutive laws. This main adjustment and a few other minor adjustments illustrated in subsequent sections will allow MCFT to estimate the shear strength of SFRC. In the subsequent sections, the experimental procedure and test results for the panels under in-plane shear loading are briefly discussed before deriving the analytical model.

doi:10.6342/NTU202403952

3.2 Review of the experiment on panels under In-Plane Shear Loading

3.2.1 Panel Specifications

Two normal-strength HF-SHFRC shear panels were tested at the University of Toronto using the Panel Element testing facility under monotonic in-plane pure shear stress conditions. Table 3-1 contains the details of the panel specimens.

Table 3-1 Details of Panel Specimens

Specimen ID	**Concrete Type**	f'_c	**Fiber Type**	V_f	**Longitudinal Steel**		**Transverse Steel**	
		(MPa)		**(%)**	ρ_{sx}	f_{yx}	ρ_{sy}	f_{yy}
					%	**MPa**	**%**	**MPa**
HFF1V1	Normal Strength	35	RC80/30-BP	1.5	2.47	552	-	-
HFF2V2		21	RC80/60-BN	0.75	2.47	552	-	-

A parametric study was conducted to understand the behavior of HF-SHFRC panels, comparing analysis results from Vecchio & Collins [14] and Susetyo [75]. Vecchio & Collins examined shear panels under various loading conditions, while Susetyo focused on SFRC panels with low transverse steel reinforcement, varying fiber types and content. Panels with both longitudinal and transverse reinforcement served as control panels. Details on the concrete mix, experimental procedures, and testing for panels PV6, PV13, C2C, and C2F2V3 are available in Vecchio and Susetyo's respective studies and the summary of these panels is given in Table 3-2 for comparison.

Table 3-2 Test Sets

Specimen ID	**Concrete Type**	f'_c	**Fiber Type**	V_f	**Longitudinal Steel**		**Transverse Steel**	
		(MPa)		**(%)**	ρ_{sx}	f_{yx}	ρ_{sy}	f_{yy}
					%	**MPa**	**%**	**MPa**
Tests Performed by Vecchio & Collins (1986)								
PV6	Normal Strength	29.8	-	-	1.79	266	1.79	266
PV13		18.2	-	-	1.79	248	-	-
Test Performed by Susetyo (2009)								
C2C	High Strength	90.5	-	-	3.31	552	0.42	477
C2F2V3		76.5	RC80/30-BP	1.5	3.31	552	-	-

3.2.2 Material Constitution

Table 3-3 and Table 3-4 provide the concrete mixing proportions and the characteristics of the hooked-end steel fibers used in the study. Two types of steel fibers, differing in length and diameter but with the same aspect ratio, were utilized. In order to mitigate the reduction in workability caused by the addition of fibers, the ratio of coarse to fine aggregate was adjusted according to recommended by Liao et al. [32]. The concrete was prepared using coarse aggregate with a maximum size of 10 mm, and admixtures were added to achieve the desired workability of the concrete. The mixing process followed the methodology outlined by Susetyo [75]. The batching and mixing processes were carried out using the facilities at the University of Toronto.

Table 3-3 Concrete Mix Proportion

Material	**Proportion**
Cement (ASTM Type III)	1
Fly ash (Class C)	0.875
Fine aggregate	2.2
Coarse aggregate	1.2
Water	0.8
Superplasticizer (SP)	0.005
Viscosity modifying admixtures (VMA)	0.038

Table 3-4 Geometry and Properties of Fiber

Fiber Type	l_f in (mm)	d_f in (mm)	Aspect Ratio	Tensile Strength in (MPa)
RC 80/30 BP	30	0.38	79	2300
RC 80/60 BN	60	0.75	80	1050

3.2.3 Specimen description and panel test

Panel specimens measuring 890 x 890 x 70 mm were prepared using two layers of reinforcement in a single longitudinal direction only. Table 3-1 presents the specifications of the reinforcement, with both panels containing 2.47% reinforcement only in the longitudinal direction. The reinforcement consisted of cold-formed deformed bars while steel fibers contributing resistance against deformation in the transverse direction. After installing the reinforcing bars and shear keys, the specimen was cast in the steel formwork. Rubber spacers were inserted between the gaps of the two shear keys to seal the formwork and prevent cement slurry from leaking out. There were a total of twenty shear keys, with five on each side of the panel, cast on all four sides. The reinforcement was spliced with 5/16" threaded rod to secure it with the shear keys. The load transfer from the shear key to the reinforced concrete panel was facilitated by splicing the threaded rods (or shear studs) to the reinforcement. To ensure secure mechanical anchorage at the end of the threaded rod, a system consisting of a nut and washer were used. After a curing time of 7 days, the specimens were tested.

All tests were conducted using the Panel Element Test facility, designed by Vecchio and Collins [14] at the University of Toronto, capable of applying various in-plane loads. Since uniaxial tensile tests are limited in their ability to accurately measure the interaction between the reinforcement and fiber-reinforced concrete, panel tests are typically performed [75]. Figure 3-1 displays the parts of the panel test rig. As seen in Figure 3-

1(a), the panel test apparatus is composed of a steel box reaction frame that accommodates the jack and link assembly.

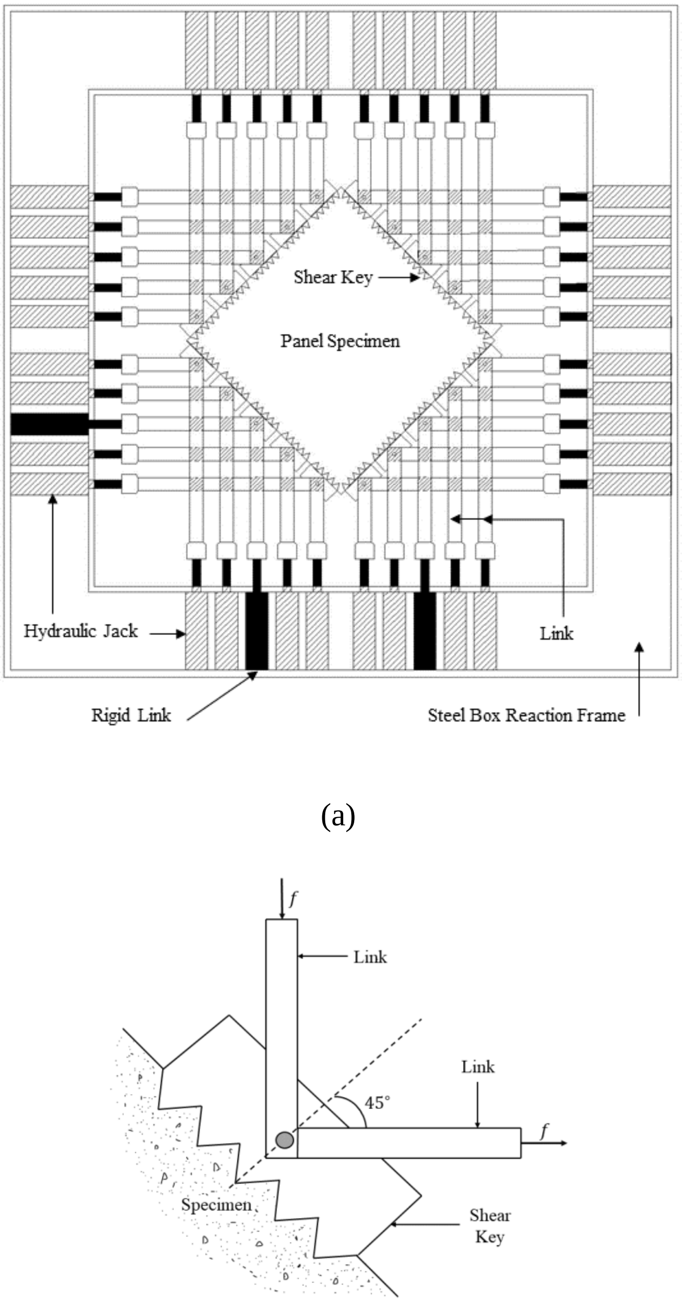

(a)

(b)

Figure 3-1 (a) Diagrammatic representation of Panel Element Testing Facility (b) Link-Shear Key assembly [8]

The two links were connected to each shear key in order to load the specimens into the testing facility. Specimens were loaded using two links per shear key, undergoing pure monotonic shear. Thirty-seven links around the member's periphery induce force in shear keys, while three rigid links stabilize the panel within the rig [76]. Lateral support frames and tie-rods prevent out-of-plane displacement. To ensure pure shear conditions, one link undergoes compressive force, and another equal amount of tensile force, as shown in Figure 3-1(b). To prevent out-of-plane displacement, the panel needs to be installed into the panel testing machine appropriately. This out-of-plane displacement may occur from inconsistent lengths of the links and over tightening the bolt that secures the links to the shear key Figure 3-1(b).

Strain gauges and linear variable differential transducers (LVDTs) were placed on the panel to continuously monitor the strain in all four directions. LVDTs were positioned on both the front and back surfaces of the panel to assess the average strains within a specific length. These LVDTs do not demonstrate localized strain behavior. Figure 3-2(a) depicts the arrangement of twelve LVDTs, which were positioned on both the front and rear sides of the panel. The Zurich gauge is a mechanical strain device that demonstrates localized strain behavior in a particular area. This strain measurement method involved affixing 16 aluminum targets to each face of the panel specimen. Figure 3-2(b) illustrates the arrangement of the metal targets that are properly positioned on a grid measuring 200 × 200 mm. In addition, the readings collected from the Zurich gauge were averaged and utilized to verify the data obtained from the LVDTs. The load was systematically increased until failure, and the strain in the panel specimen was measured at each load step. Strain gauges were affixed to the steel reinforcement in order to measure the localized strain.

doi:10.6342/NTU202403952

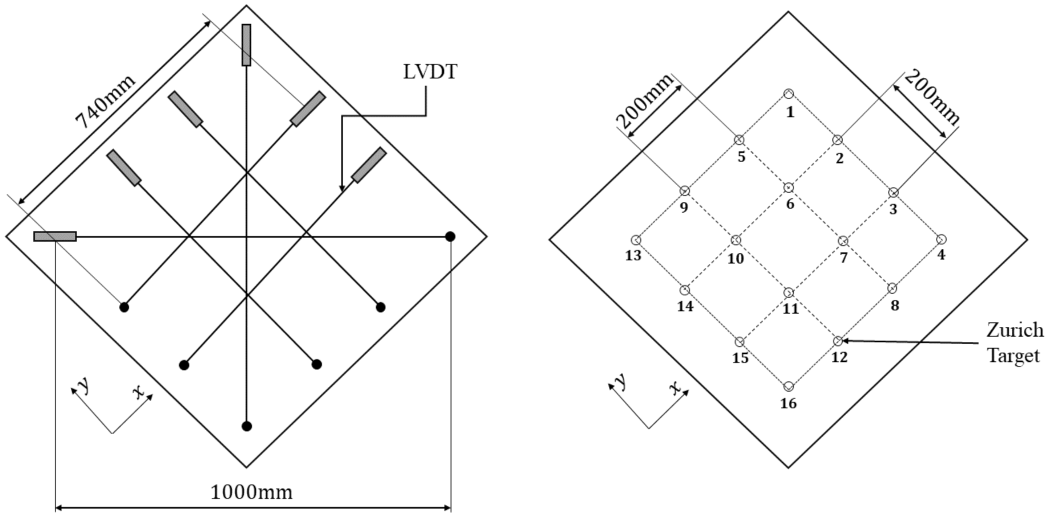

(a)

(b)

Figure 3-2 (a) Arrangement of LVDT's for the panel test (b) Layout of Zurich targets

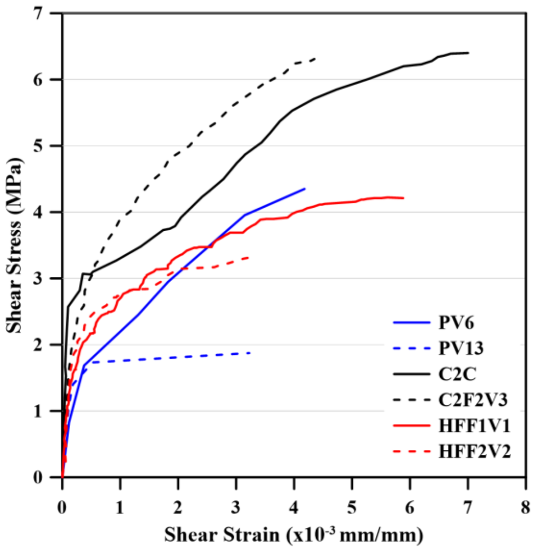

Figure 3-3 Shear stress-strain response

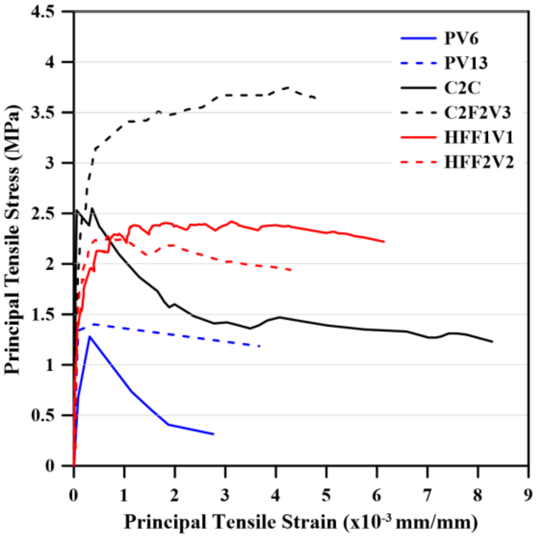

Figure 3-4

Principal tensile stress-strain response

3.3 Discussion of Experimental Results

Figure 3-3 and Figure 3-4 illustrate the panels' shear and tension responses, respectively. Figure 3-3 illustrates the linear relationship between shear stress and shear strain in the panel until the first crack appears. The shear stress values at the initiation of the first cracking (v_{cr}) and the maximum shear strength (v_u) are given in Table 3-5.

Table 3-5 Summary of the Panel Test Results

Panel	**Concrete**		**Experimental Observations**	
	ϵ_c'	f_c'	v_{cr}	v_u
	×10^{-3}	MPa	MPa	MPa
C2C	2.703	90.5	2.57	6.40
PV6	2.5	29.8	2.00	4.55
PV13	2.7	18.2	1.73	2.01
C2F2V3	2.224	76.5	1.59	6.31
HFF1V1	2.708	35	1.63	4.22
HFF2V2	2.853	21	1.90	3.31

The maximum shear stresses for panels PV13 and C2F2V3 were 44.18% and 98.59%, respectively, when compared to the control panels PV6 and C2C, respectively. Figure 3-3 demonstrates that the SFRC panel C2F2V3, reinforced with RC65/35-BN fibers, exhibited shear strength that was nearly identical to that of the control panel C2C. Similar findings can also be made for the HFF2V2 and PV13 panels without transverse reinforcement. The inclusion of merely 0.75% additional fibers resulted in a notable improvement of shear strength, with an increase of 39%. The reason for this is that the inclusion of fibers greatly enhances shear strength [6,13]. The RC panel PV13 that is without longitudinal reinforcement exhibited less than 50% of the shear strength observed in the control panel PV6. Furthermore, it is evident that SFRC panels HFF1V1 and HFF2V2 attain shear stress that is at least 73% of the shear stress exhibited by control panel PV6. The shear resistance of panel HFF2V2 is lower than that of panel HFF1V1 because the equivalent shear resistance cannot be achieved at a low fiber content [7]. Nevertheless, the response indicated by panel HFF2V2 is acceptable especially considering the absence of transverse reinforcement. The fiber-type RC80/30BP exhibited the maximum shear stress value because to its high tensile strength, as seen by the test results of panel HFF1V1 in Figure 3-5. This panel also had improved crack control capabilities compared to panel HFF2V2. This finding is consistent with the results presented by Susetyo et. al. [7]. It indicates that the shear strength of SFRC panels is not considerably influenced by the compressive strength of concrete. However, the type of fiber and aspect ratio do have an impact. The data presented above show a 28% increase in shear strength when the fiber content was doubled (from 0.75 to 1.5%) between panel HFF2V2 and HFF1V1. Increase in fiber aspect ratio indicates higher post-cracking deformation capabilities. Panel HFF2V2 achieved a shear strain that was 37% lower than panels HFF1V1 and C2F2V3 due to the lower dosage of fibers.

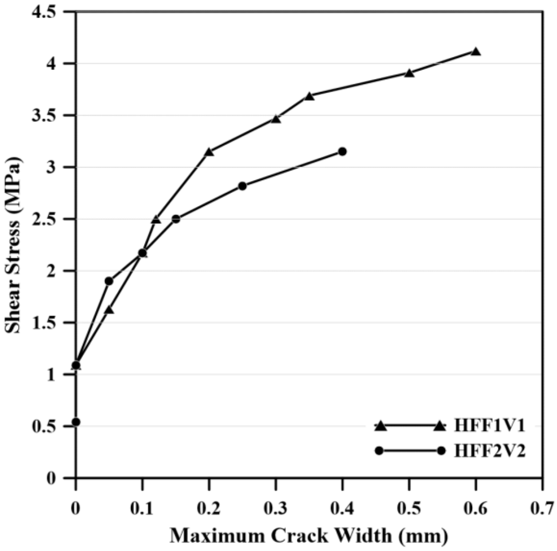

Figure 3-5 Propagation of cracks in panels HFF1V1 and HFF2V2

The principal tensile stress-strain relationship for the panels is illustrated in Figure 3-4. The occurrence of the first crack indicated the point of maximum principal tensile stress in reinforced concrete (RC) panels. The strain-hardening behavior of all the SFRC panels is attributed to the presence of fibers, which improve the bridging effect across cracks and improve the transfer of tensile stresses. Nevertheless, due to the progressive degradation of the bond between the reinforcement and concrete, all reinforced concrete (RC) panels showed strain-softening behavior. Panel C2C displayed brittle behavior because of its high-strength concrete mix. The principal tensile stress decreased until failure occurred after the first crack appeared. In contrast, specimen C2F2V3 demonstrated that the control of crack propagation by an increase in principal tensile stress and shear stresses.

The failure of all SFRC panels occurred due to shear slip on the crack surface, resulting in the pull-out of fibers from the matrix and the loss of aggregate interlock. Figure 3-6(a) and Figure 3-6(b) display the failure modes for panels HFF1V1 and HFF2V2. At the peak load of 2.01 MPa, the load in panel PV13 abruptly dropped to 1.73 MPa. The concrete failed in shear before the reinforcement yielded. Additionally, the PV6 RC panel failed due to the transverse reinforcement yielding. Panel C2C exhibited sudden failure due to severe concrete spalling and rupture of the transverse reinforcement.

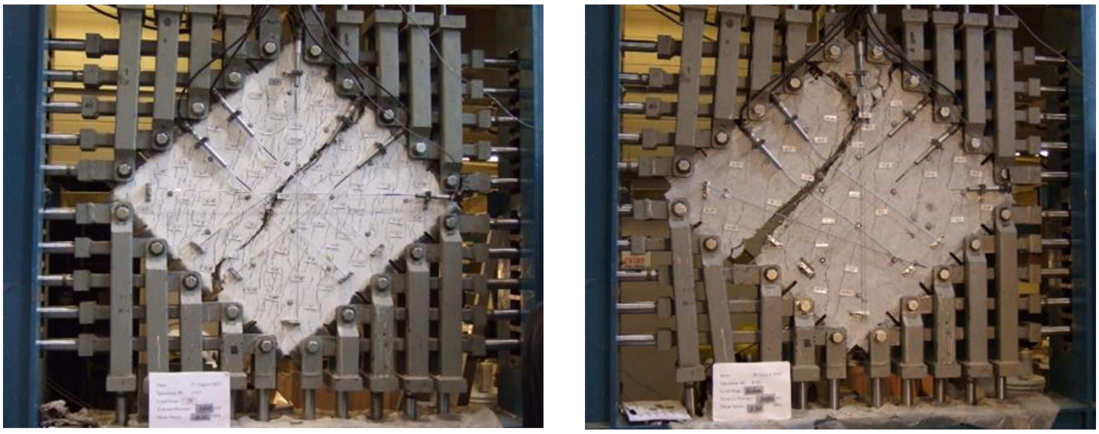
(a) (b)

Figure 3-6 Failure stage of panel: (a) HFF1V1, (b) HFF2V2

3.4 Material Constitutive laws

3.4.1 Constitutive laws for cracked concrete

Concrete in Compression: For understanding the behavior of the cracked concrete following Eq. (3-1) is used where the value of strain in concrete with reference to peak

doi:10.6342/NTU202403952

stress (ϵ_c') in cylinder compression, often referred to as -0.002 (negative the quantity). Eq. (3-2) represents the average maximum principal compressive stress (f_{c2max}) in cracked concrete.

$$f_{c2} = f_{c2max}\left[\frac{2\epsilon_2}{\epsilon_c'} - \left(\frac{\epsilon_2}{\epsilon_c'}\right)^2\right] \tag{3-1}$$

$$f_{c2max} = \frac{f_c'}{0.8 - 0.34\left({\epsilon_1}/{\epsilon_c'}\right)} \leq 1.0 \tag{3-2}$$

Concrete in Tension: Eq. (3-3) establishes the correlation between the principal tensile stress (f_{c1}) and strain (ϵ_1) in the concrete before it cracks, to represent the tensile behavior of SFRC. In addition, the model proposed by Naaman in 1972 [77], which is based on the statistical mechanics of composite materials, has been used to demonstrate the ductile behavior of SFRC after cracking. Thus, at this stage, the value of f_{c1} can be approximated using Eq. (3-4).

$$f_{c1} = E_c\epsilon_1 \text{ for } \epsilon_1 \leq \epsilon_{cr} \text{ (Ascending Branch)} \tag{3-3}$$

$$f_{c1} = \sigma_{cc} + \frac{\sigma_{pc}-\sigma_{cc}}{\epsilon_{pc}-\epsilon_{cc}} \times (\epsilon_1 - \epsilon_{cc}) \text{ for } \epsilon_1 > \epsilon_{cr} \text{ (Strain Hardening Branch)} \tag{3-4}$$

The variables σ_{cc} and σ_{pc} represent the initial cracking and post-cracking strength of concrete, respectively. ϵ_{cc} and ϵ_{pc} represent the cracking strain and maximum strain in concrete, respectively. E_c represents the modulus of elasticity of concrete in MPa. These values are derived by the following equations:

$$\sigma_{cc} = \sigma_{mu}\left(1 - V_f\right) + \alpha\tau_{eq}V_f\left(\frac{l_f}{d_f}\right) \tag{3-5}$$

$$\sigma_{pc} = \lambda\tau_{eq}V_f\left(\frac{l_f}{d_f}\right) \tag{3-6}$$

$$E_c = 4700\sqrt{f_c'} \tag{3-7}$$

doi:10.6342/NTU202403952

Where, strength at concrete cracking $(\sigma_{mu}) = 0.33\sqrt{f_c'}$ (MPa).

As per the ACI 363 [1], concrete has been classified into high-strength concrete and normal strength (low-strength) concrete. High strength concrete is characterized by having a compressive strength that is greater than 55 MPa. Using these two categories, values for the bond strength at the interface between fibers and matrix (τ_{eq}) were determined. The equivalent bond stress for high-strength concrete is 5.6 MPa, while for normal strength concrete it is 4.65 MPa. These values were determined directly from fiber pull out tests conducted on hooked end steel fibers with various mix proportions by Liao et al. [10]. If the value of (τ_{eq}) is not known, it can be approximated using the Variable Engagement Model (VEM) as $\tau_{eq} = 0.825\sqrt{f_c'}$ (MPa). However, it is important to note that this model may underestimate the pull-out strength for hooked-end steel fibers since it only takes into account the frictional bond qualities and does not consider the mechanical anchorage [9,78]. In addition, the values of α and λ used in this work have been defined as 0.25 and 0.65, respectively. These values are obtained from the coefficients resulting from the uniaxial tension tests conducted by Susetyo [75]. Moreover, substituting $\epsilon_{pc} = 0.007$ into Eq. (3-4) yields Eq. (3-8). The direct tension test indicated a maximum tensile strain value of 0.7% [32,79]. In contrast, plain concrete also achieves the maximum level of tensile strain at 0.7% [31]. Therefore, Eq. (3-8) is considered conservative for both plain concrete and the SFRC.

$$f_{c1} = \sigma_{cc} + \frac{\sigma_{pc} - \sigma_{cc}}{0.007 - \epsilon_{cc}} \times (\epsilon_1 - \epsilon_{cc}) \tag{3-8}$$

3.4.2 Constitutive laws for steel reinforcement

The stress-strain relationship for bare reinforcing steel bars is considered to be a bilinear, elastic-perfectly plastic, and can be expressed as

$$f_{sx} = E_s \epsilon_x \tag{3-9}$$

$$f_{sy} = E_s \epsilon_y \tag{3-10}$$

Where, E_s = elastic modulus of reinforcing bar; f_s = stress in reinforcing bar; ϵ_x and ϵ_y= strain in steel respectively in x and y direction.

3.5 Strain Compatibility

Given that the strain in steel and concrete is the same at any loading instance ($\epsilon_s = \epsilon_c = \epsilon$), the Mohr's circle for strains in the ϵ and $\gamma/2$ coordinate system, as depicted in Figure 3-7 illustrates the geometric correlations for the three strain components described by Eq. (3-11) to (3-13).

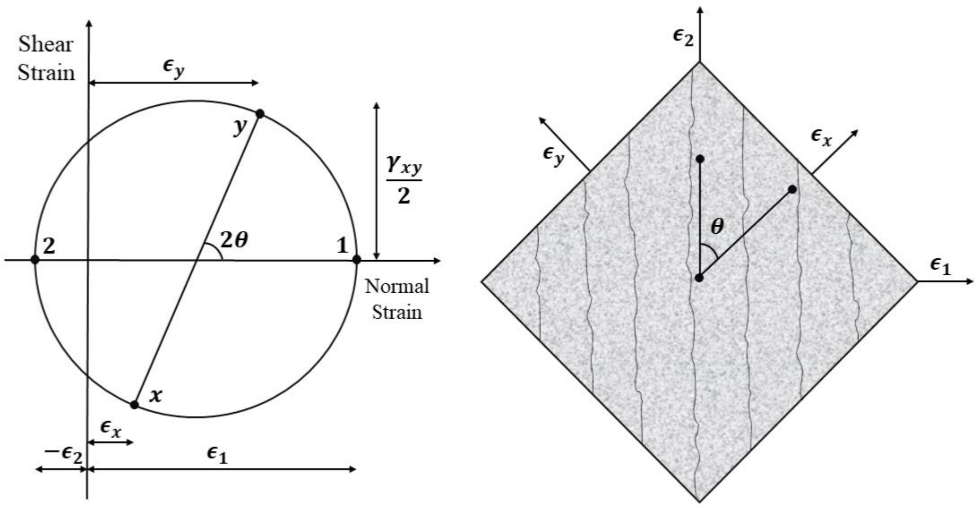

Mohr's Circle **Average Strains**

Figure 3-7 Strain compatibility for cracked element

$$\gamma_{xy} = 2(\epsilon_x - \epsilon_2)/tan\theta \tag{3-11}$$

$$\epsilon_x = \epsilon_1 + \epsilon_2 - \epsilon_y \tag{3-12}$$

$$\epsilon_y = \frac{\epsilon_1 + \epsilon_2 tan^2\theta}{1 + tan^2\theta} \tag{3-13}$$

The negative quantity of principal compressive strain in concrete (ϵ_2) can be calculated numerically using the following Eq. (3-14).

$$\epsilon_2 = \epsilon_c' \left(1 - \sqrt{1 - \frac{f_{c2}}{f_{c2max}}}\right) \tag{3-14}$$

The equation to calculate the angle θ, according to Mohr's compatibility truss model, is as follows:

$$tan^2\theta = \frac{\epsilon_x - \epsilon_2}{\epsilon_y - \epsilon_2} \tag{3-15}$$

3.6 Force Equilibrium

Prior to cracking, the applied forces are balanced by the combined effect of the steel and concrete. The following equilibrium equations are considered after eliminating the difference between the actual cross-sectional area of the concrete before and after the incorporation of reinforcing bars. That is, the decrease in the concrete's cross-sectional area caused by the reinforcing bars is not taken into account.

$$f_x = f_{cx} + \rho_{sx} f_{sx} \tag{3-16}$$

$$f_y = f_{cy} + \rho_{sy} f_{sy} \tag{3-17}$$

$$v_{xy} = (f_{c1} - f_{cy})/tan\theta \tag{3-18}$$

$$f_{cx} = f_{c1} - \frac{v_{xy}}{tan\theta} \tag{3-19}$$

$$f_{cy} = f_y - \rho_{sy} f_{sy} \tag{3-20}$$

$$f_{c2} = f_{c1} - v_{xy}(tan\theta + 1/tan\theta) \tag{3-21}$$

doi:10.6342/NTU202403952

Where, f_x and $f_y =$ stresses applied to the element in x and y directions respectively; f_{cx} and $f_{cy} =$ stresses in concrete in x and y directions respectively; ρ_{sx} and $\rho_{sy} =$ are the reinforcement ratios in the respective directions x and ; $v_{xy} =$ the shear stress.

After the development of cracks, it is important to take into account the stresses in the reinforcement at the location of the cracks. These stresses can be estimated in the following manner. Figure 3-8 depicts the stresses at various positions within the SFRC element.

$$f_{sxcr} = f_{sx} + (f_{c1} + f_{ci} + v_{ci}/tan\theta)/\rho_{sx} \tag{3-22}$$

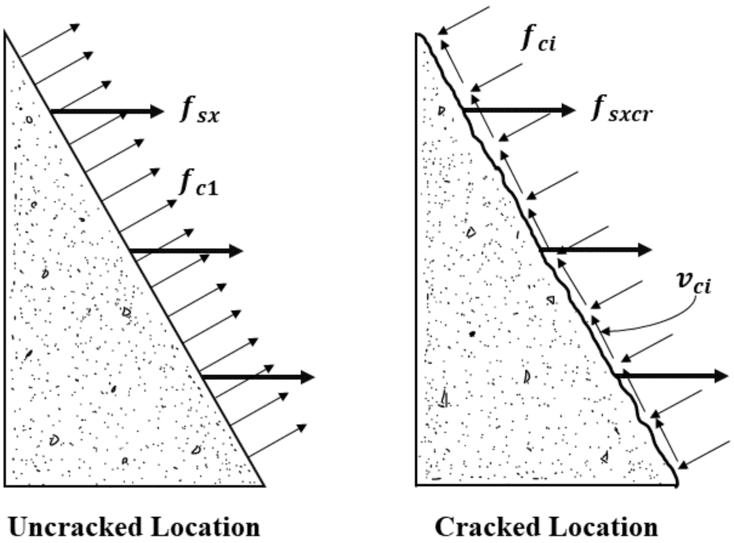

Uncracked Location **Cracked Location**

Figure 3-8 Stresses in steel and concrete at the uncracked and cracked location

In order to determine the correlation between the principal tensile strain and the crack width, it is essential to consider the average distance between the cracks. The values for average crack spacing (s_m) are directly derived from the experimental results. Consequently, the width of cracks can be calculated using the following equation:

$$w = \epsilon_1 s_\theta \tag{3-23}$$

Where, s_θ is the crack spacing measured at an angle θ.

$$s_\theta = \frac{1}{\left(\frac{sin\theta}{s_{mx}} + \frac{cos\theta}{s_{my}}\right)} \tag{3-24}$$

To determine the maximum resistance to shear stress for a given width of the crack, following relationship can be used:

$$v_{cimax} = \frac{\sqrt{-f_c'}}{0.31 + 24w/(a + 16)} \tag{3-25}$$

Where, a is the maximum size of aggregate.

3.7 Solution method

The proposed solution approach is based on the equations outlined in the preceding section. The solution algorithm can be seen in Figure 3-9. In this trial-and-error approach, the number of iterative cycles needed to satisfy all conditions are determined for a given assumed value of f_x,. This process will provide a single point on the v_{xy}versus γ_{xy} curve.

During the primary stage (S), it is essential to input all of the relevant material properties, crack spacing characteristics, and fiber properties. The process for determining the whole v_{xy}versus γ_{xy} curve begins with assuming the values of ϵ_1, θ, and f_x (Steps 1 to 3). Prior to step 6, it is important to note that the condition $f_{c2}/f_{c2max} \leq 1.0$ is fulfilled; otherwise, the solution is not possible [14]. If the condition fails to be fulfilled, an alternative value of θ in proximity of 45 degrees can be assumed, or a lower value of ϵ_1 may be used. Therefore, in addition to the three decision making steps in the solution algorithm, it is important to take this condition into account.

The lower half section of the solution algorithm is comparatively complex than the upper half section. Minor adjustments are required in the computation of Δf_{c1} in the

doi:10.6342/NTU202403952

original MCFT to more accurately represent the behavior of SFRC with reinforcement in the longitudinal direction only. The computation of v_{ci} and f_{ci} may take different routes for each load stage, as specified in the algorithm. Furthermore, it is important to observe that the computed value of f_{sxcr} increases for every increment in the value of f_x. By performing calculations for a series of f_x values and repeating steps 1 to 11, the entire v_{xy}versus γ_{xy} curve can be obtained.

In order to identify the failure pattern, the guidelines presented by Vecchio & Collins [14] were followed. The pattern of failure is determined by satisfying any of the conditions listed in Table 3-6 at the stage of failure. These conditions can be applied separately or in conjunction with others.

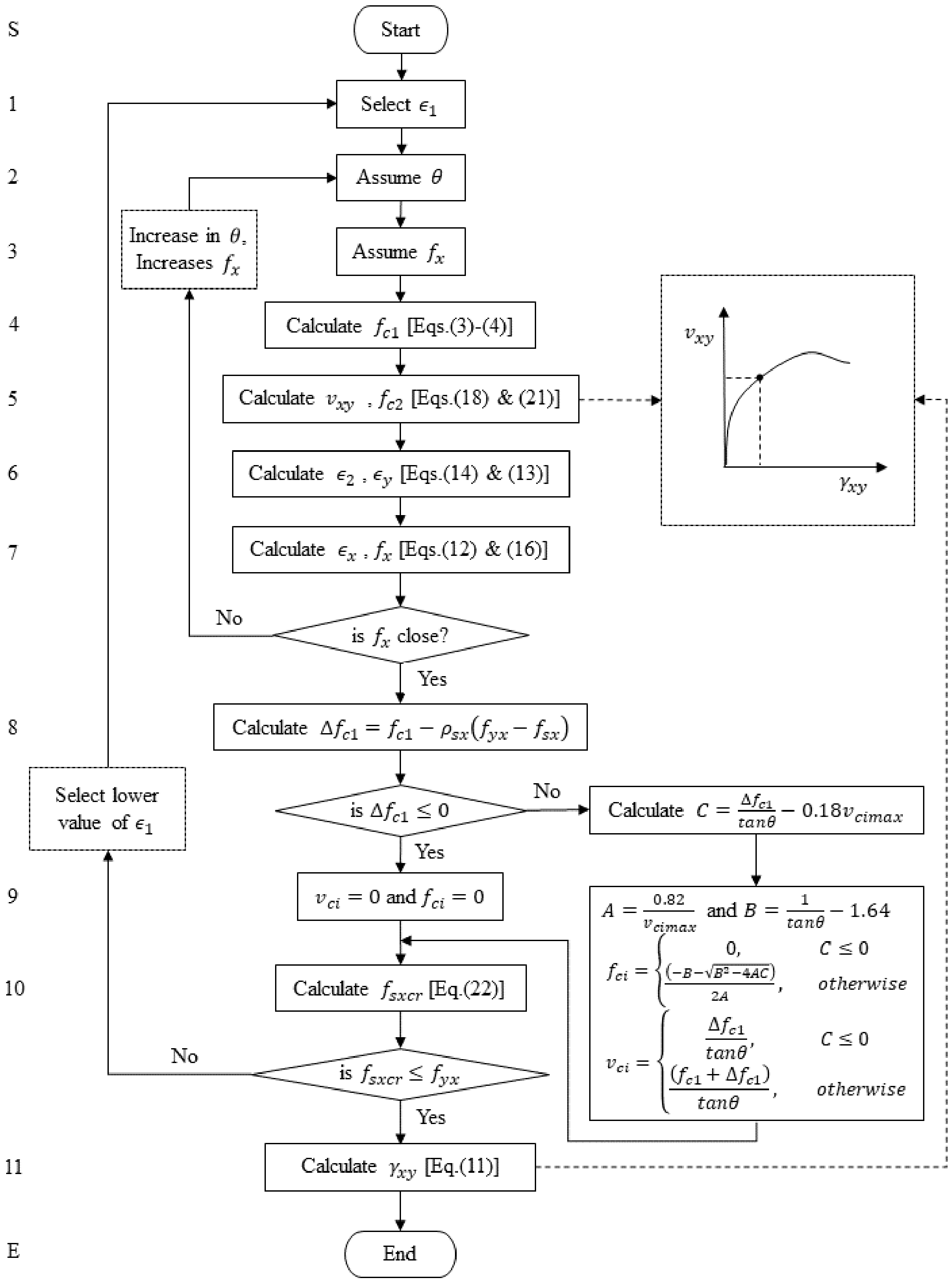

Figure 3-9 Solution algorithm (Based on equations presented in this chapter)

Table 3-6 Failure Patterns for the SFRC Panels

Condition	**Prediction**
Condition 1: $f_{c1} \leq v_{cimax}(0.18 + 0.3k^2)tan\theta + \rho_{sy}(f_{yy} - f_{sy})$ Where, $k = 1.64 - 1/tan\theta$, but $k \geq 0$.	Slip-on the crack
Condition 2: $f_{c2} \leq f_{c2max}$	Concrete shear failure
Condition 3: $f_{sxcr} \leq f_{yx}$	Yielding the reinforcement

3.8 Verification of the model

The proposed analytical model was implemented for predicting the shear stress-strain behavior of the SFRC panel specimens in order to evaluate its accuracy. The appendix provides the values for the estimated ultimate shear strength (v_{umodel}) obtained from the proposed analytical method, as well as the results of the experiment (v_{uexp}). The shear strength obtained from the proposed model is compared to the experimental data in order to check the model's validity. The data set for 30 SFRC panels was collected, as reported in the Appendix A. Out of them, 18 panels were tested under monotonic loading, while the remaining 12 panels were tested under reversed cyclic loading [2,7,80,81]. Variation is also apparent in the types of steel fibers utilized. In addition, the prediction results derived from the proposed model for the two panels that include MAC Matrix fibers (DC-P3, DC-P5) can also be seen in the last two rows of the Appendix A.

doi:10.6342/NTU202403952

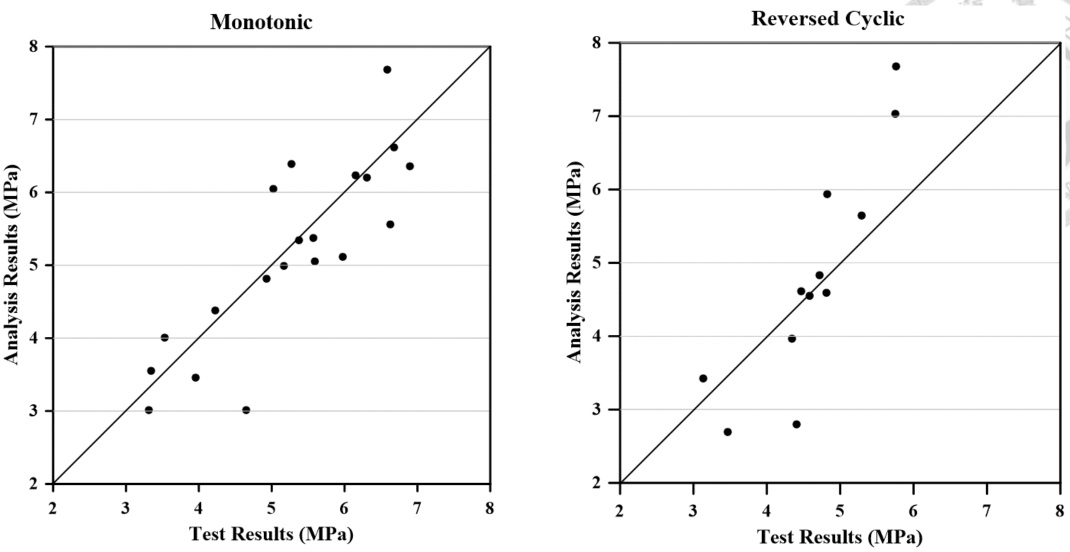

(a) (b)

Figure 3-10 Shear stress calculated from the proposed analysis procedure to test results: (a) Monotonic (b) Reversed cyclic

The results obtained from the proposed analysis procedure are plotted alongside the experimental results in Figure 3-10(a) and Figure 3-10(b) respectively. The coefficient of variation (CoV) for monotonic loading conditions was 15.41%, whereas for reversed cyclic loading conditions it was 22.34%. The data shows the shear strength prediction for monotonic loading closely resembles the experimental results, as compared to the reversed cyclic loading condition. This indicates that the method described in this paper is intended for monotonic loading and does not consider the effects of reversed cyclic loading. Figure 3-11 illustrates the predicted shear stress-strain behavior of the HFF1V1 and HFF2V2 panels, as predicted by the proposed analysis method. The sample calculation for panel HFF1V1 is given in Table 3-7 for reference. Figure 3-11(b) illustrates that the analysis results for panel HFF2V2 align well with the actual results. However, slight discrepancies can be found in the estimated response of panel HFF1V1 [Figure 3-11(a)]. These discrepancies can be related to the sensitivity of the tension model Eq. (3-8). The sensitivity is determined by the computed values of α, λ, and τ_{eq}, obtained from the uniaxial tension test and fiber pullout test. The outcomes of the uniaxial tension test can be substantially influenced by factors such as aggregate distribution, improper mixing, and the experimental procedure [82]. Based on the criteria outlined in Table 3-6, the failure mode observed in this study for both panels can be classified as shear-slip failure, given the first two conditions specified in Table 3-8 are satisfied.

Table 3-7 Calculated response for panel HFF1V1

ε_1	θ	f_{c1}	**Condition 1**	V_{xy}	f_{c2}	f_{c2}/f_c'	f_{c2max}	f_{sxcr}	Υ_{xy} X 10^{-3}	**Remarks**
	Degree	**MPa**		**MPa**	**MPa**		**MPa**	**MPa**		
0	0	0	0	0	0	0	0	0	0	
0.0002	44.8	3.301769	5.577997	3.324901	-3.34819	0.095663	-41.9664	146.7917	0.281434	
0.0007	42	3.322174	4.240446	3.689648	-4.09777	0.117079	-38.0849	191.2692	0.806216	
0.0025	40	3.395632	3.074579	4.046757	-4.82274	0.137792	-28.5714	346.57	2.635929	
0.004	39	3.456847	2.524324	4.26885	-5.27159	0.150617	-23.6486	464.194	4.144362	Condition 1 and Condition 2 (Table 3-6)
0.005	38.6	3.497657	2.277987	4.381439	-5.48853	0.156815	-21.2121	541.27	5.146913	Peak Load $f_{sxcr} \cong f_{yx}$
0.0052	38.6	3.505819	2.204051	4.391663	-5.50134	0.157181	-20.1729	558.1643	5.348693	Fail $f_{sxcr} > f_{yx}$

Note:

Condition 1: $f_{c1} \leq v_{cimax}(0.18 + 0.3k^2)tan\theta + \rho_{sy}(f_{yy} - f_{sy})$
Slip-on the crack

Condition 2: $f_{c2} \leq f_{c2max}$
Concrete shear failure

$f_{sxcr} \cong f_{yx}$ Reinforcing bars have reached yielding capacity

$f_{sxcr} > f_{yx}$ The reinforcement is unable to carry additional stresses
(This point is not included in the shear stress-strain curve)

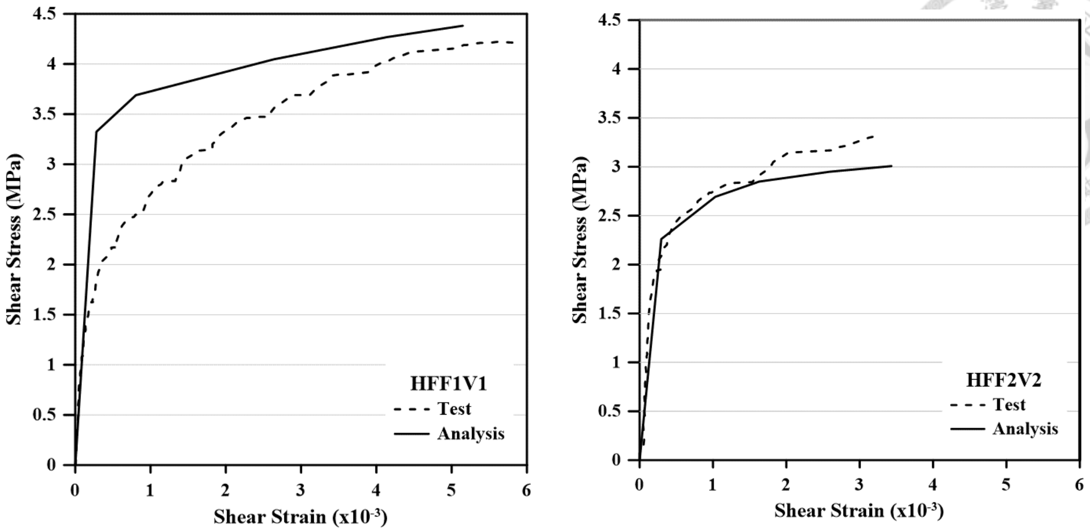

(a) (b)

Figure 3-11 Comparison of shear stress-strain response between test and analysis

Table 3-8 Predicted failure patterns for the panels tested in this study

Specimen ID	**Applicable conditions**	**Failure Pattern**
HFF1V1	Condition:1 and Condition: 2	Shear Slip
HFF2V2	Condition:1 and Condition: 2	Shear Slip

3.9 Summary

The inclusion of fibers enhances the bridging effect over cracks, leading to increased shear and tension performance in SFRC panel specimens compared to conventionally reinforced concrete panels, due to strain hardening behavior. Additionally, the strength of the concrete is influenced by the type of fiber used.

The proposed analysis procedure enables MCFT to predict the shear stress–strain response of SFRC panels by incorporating strain hardening behavior of fibers. The key difference between original MCFT for RC and Modified MCFT for SFRC is indicated in Table 3-9. This procedure was validated by comparing the analysis results with experimental data from 30 SFRC shear panels, accurately predicting both the shear strength and the failure pattern.

Table 3-9 Comparison between Original MCFT for RC and Modified MCFT for SFRC

Parameter		**MCFT**	**Modified MCFT for SFRC**
$\boldsymbol{f_{c1}}$	$\epsilon_1 \leq \epsilon_{cr}$	$E_c\epsilon_1$	$E_c\epsilon_1$
	$\epsilon_1 > \epsilon_{cr}$	$\dfrac{f_{cr}}{1+\sqrt{200\varepsilon_1}}$	$\sigma_{cc} + \dfrac{\sigma_{pc} - \sigma_{cc}}{0.007 - \epsilon_{cc}} \times (\epsilon_1 - \epsilon_{cc})$
Reinforcement stresses at cracks		$f_{sycr} = f_{sy} + (f_{c1} + f_{ci} - v_{ci} tan\theta)/\rho_{sy}$ (Presence of Transverse Reinforcement)	$f_{sxcr} = f_{sx} + (f_{c1} + f_{ci} + v_{ci}/tan\theta)/\rho_{sx}$ (Absence of Transverse Reinforcement)
$\Delta \boldsymbol{f_{c1}}$		$f_{c1} - \rho_{sy}(f_{yy} - f_{sy})$	$f_{c1} - \rho_{sx}(f_{yx} - f_{sx})$

Chapter 4 Development of Softened Strut-and-Tie Model for SFRC

4.1 Summary of isolated panel tests

The experimental program involved the examination of 43 square and rectangular panels made of high-strength steel-fiber reinforced concrete. All the specimens underwent in-plane axial compression loading tests. Detailed information about the experimental procedure is presented in the following subsections.

Portland cement conforming to ASTM Type I, ground granulated blast furnace slag (ASTM Grade 100), and silica fume were used as cementitious materials. Manufactured sand and coarse aggregate with a nominal size of 10 mm were employed. High-range water-reducing admixture (superplasticizer) with a specific gravity of 1.08 was added to ensure the desired workability of the fiber-reinforced mixtures. The fibers used in this study were Dramix RC80/30-BP hooked-end steel fibers, of length 30 mm (l_f), 0.38 mm in diameter (d_f), and an aspect ratio $(\frac{l_f}{d_f})$ of 79.The ultimate tensile strength of the fibers was 2300 MPa. The design concrete compressive strength for all specimens was set at 70 MPa. The details of the concrete mix proportions are summarized in Table 4-1. Reinforcing bars with varying specified yield strength and diameter were employed. The properties of the reinforcing steel are listed in Table 4-2.

Table 4-1 Mix design details of concrete

Material	Proportion
Cement	1
Slag	0.65
Silica Fumes	0.12
Coarse Aggregate	1
Fine Aggregate	2.49
Water	0.52
Superplasticizer (SP)	0.022

doi:10.6342/NTU202403952

Table 4-2 Properties of reinforcement

Reinforcing bar type	d_b **(mm)**	A_s **(mm^2)**	f_y **(MPa)**	f_u **(MPa)**
D10 (SD785)	9.525	71	841	1042
D13 (SD785)	12.7	129	868	1066
D13 (SD420)	12.7	129	481	683
D16 (SD785)	15.87	200	848	1050

4.1.1 Fabrication

Sixteen square panel specimens (isolated strut specimens) measuring $900 \times 900 \times 100\, mm\ (l \times b \times t)$, and twenty-seven rectangular panel specimens measuring $1200 \times 600 \times 150\, mm$, were tested under compression. The square and rectangular panel specimens represent aspect ratios (l/b) of 1 and 2, respectively. Details of the isolated strut specimens are presented in Table 4-3. The Figure 4-1 illustrates the formation of the bottle-shaped strut in the square and rectangular panels when the finite area of the top edge of the panel is subjected to in-plane loading. The dispersion of in-plane loading in the bottle-shaped strut is represented by the isostatic lines of compression (ILCs). When the aspect ratio of the concrete panel exceeds 2, the bottle-shaped strut engages the full width of the panel [58,83]. Conversely, when the aspect ratio equals unity, the bottle-shaped strut engages half the width of the panel [12]. Therefore, in the present research, SFRC panel specimens with two different aspect ratios have been considered for experimental investigation.

Three primary reinforcement layouts were used in the 43 isolated strut specimens. Panels from the T and N series consisted of no reinforcement, representing the first layout. In the subsequent series of panel specimens (Series DL and DH), reinforcement was uniformly distributed. In the third series of specimens (Series TM, TL, TS and CL), reinforcement was provided in bundles, resembling the reinforcement for the tie in STM as indicated in Figures 4-1 (a), (b), (c). Longitudinal reinforcement consisted of D10

(SD785) reinforcing bars, while details of the transverse reinforcement are given in Table 4-2. Square panels comprise fiber volume fractions (V_f) of 0% and 0.75%, while rectangular panels comprise fiber volume fractions of 0%, 0.75%, and 1.5%. Plain concrete panels (0% fibers) were used as a reference for comparing the test results. Reinforcing bars were positioned at the mid-thickness of the panels, and the steel reinforcement was bound using a welding method. For square and rectangular panels, bearing plates with dimensions of $300 \times 100 \times 50\, mm$ and $200 \times 150 \times 50\, mm$, respectively, were employed. A concentration ratio of 0.33 was maintained for the bearing plates, which is defined as the ratio of the length of the bearing plate to the length of the loaded face of the panel.

In the nomenclature, 'S' represents a square panel, and 'R' represents a rectangular panel. The numbers, 0, 075, and 150 represents 0%, 0.75%, and 1.5% steel fibers volume fraction. As indicated in Table 4-3, the arrangement of reinforcement is categorized under different series. Therefore, the last term in the nomenclature indicates the arrangement of reinforcement along with the panel identification number. Each series consists of two panel specimens, except for the rectangular panel specimens without transverse reinforcement (N-Series).

To produce steel fiber reinforced concrete in large quantities, cement, aggregate, and water were batched by weight and mixed at the ready-mix concrete facility. Weighed steel fibers were added in batches to the transit mixers at the casting site, and mixing continued until the fibers were observed to be uniformly dispersed. For each batch, three cylinders measuring $100\, mm \times 200\, mm$ were prepared and used to determine the compressive strength of the fiber concrete, along with casting the panel specimen.

doi:10.6342/NTU202403952

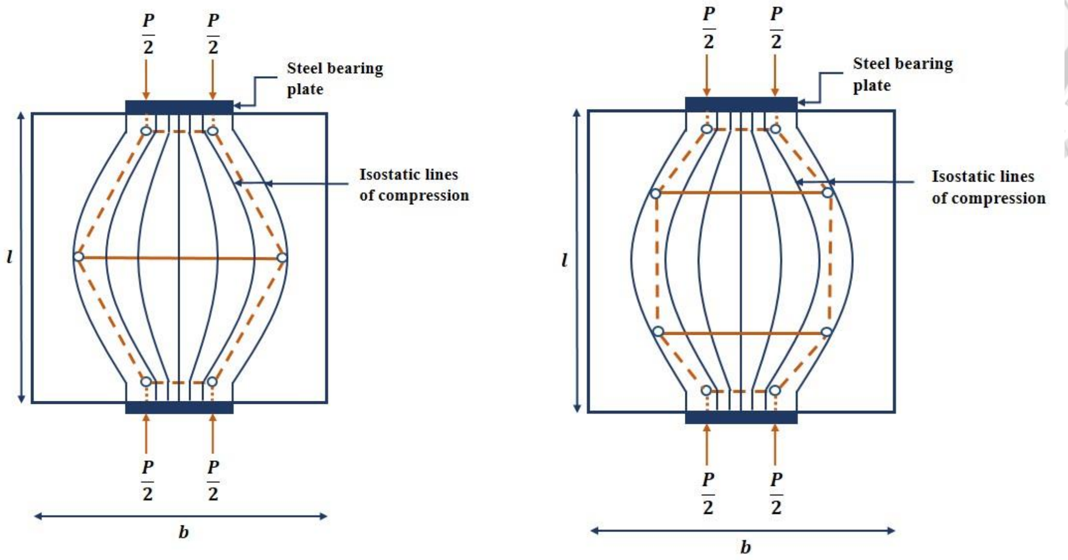

(a) Bottle-shaped strut with diamond shaped STM

(b) Bottle-shaped strut with refined STM in square panels

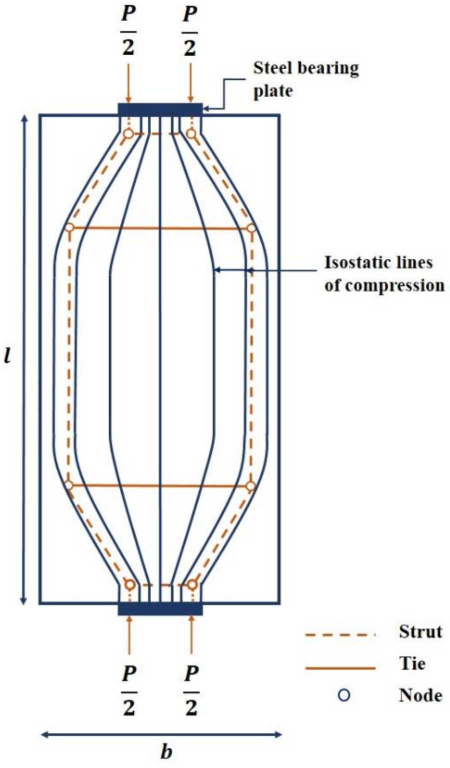

(c) Bottle-shaped strut with refined STM in rectangular panels

Figure 4-1 Stress field in the panels with corresponding strut-and-tie models

doi:10.6342/NTU202403952

4.1.2 Instrumentation

Electrical resistance strain gauges were attached to the surface of the concrete and reinforcing steel to continuously monitor the local longitudinal and transverse strains. In addition, NDI markers were fixed on either surface of the concrete panel to obtain more detailed information of local deformations. The details of the instrumentation are available in Hung (2020) [84], and Kuo (2019) [85].

4.2 Testing

The tests were conducted at the National Center for Research on Earthquake Engineering (NCREE) Taiwan. As shown in Figure 4-2, all the panels were tested to failure using a compression testing machine with a capacity of 500 tonnes. In-plane axial compression was applied through symmetrically placed 50 mm thick bearing plates at the top and bottom edges of the panel. For square and rectangular panels, the load was applied in a strain-controlled mode at a rate of 0.2 mm/min and 0.3 mm/min, respectively. Under the specified loading conditions, a bottle-shaped strut is expected to form. The cylinder tests were conducted concurrently with the panel testing. The test results for the peak compressive load, are provided in Table 4-4.

doi:10.6342/NTU202403952

Table 4-3 Details of isolated strut specimens

Panel Aspect Ratio: 1				
Bearing Plate $300 \times 100 \times 50\ mm$	Series			
	T	TM	TL	TS
	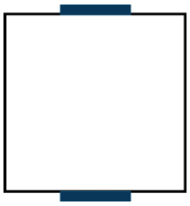	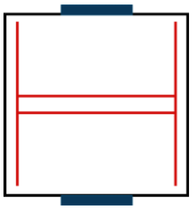	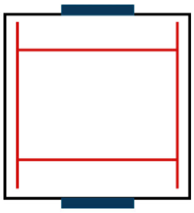	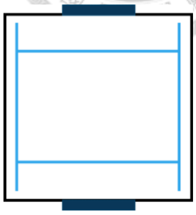
	NA	D13 (SD785)	D13 (SD785)	D13 (SD420)
Spacing of transverse reinforcement (mm)	NA	40	600	600
Panel Aspect Ratio: 2				
Bearing Plate $200 \times 150 \times 50\ mm$	Series			
	N	DL	CL	DH
	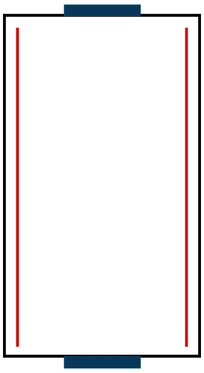	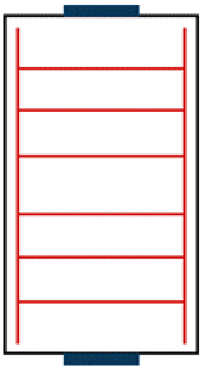	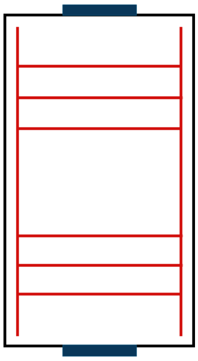	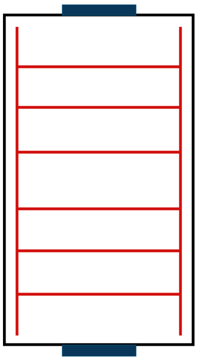
	NA	D13 (SD785)	D13 (SD785)	D16 (SD785)
Spacing of transverse reinforcement (mm)	NA	150	100	150

doi:10.6342/NTU202403952

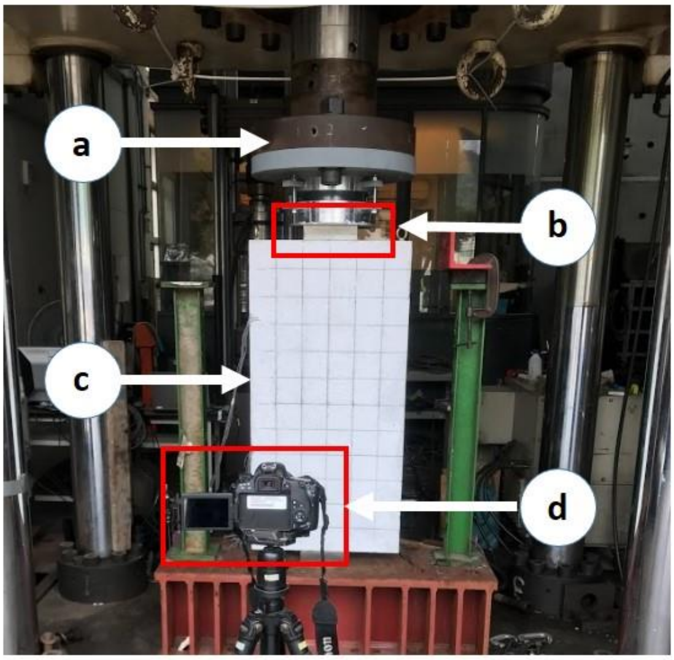

a) Compression testing machine of 500 Tonnes capacity
b) Bearing Plate
c) Panel specimen
d) Camera

Figure 4-2 Experimental setup

Table 4-4 Details of test specimens and test results

Specimen ID	f_c'	**Bar Spacing**	**Peak compressive load (P_u)**
	MPa	mm	kN
S0-T1	55.5	NA	1097.04
S0-T2	55.5		1357.09
S0-TM1	55.5	40	1649.04
S0-TM2	55.5		1611.18
S0-TL1	55.5	600	1348.13
S0-TL2	55.5		1702.85
S0-TS1	55.5	600	1572.32
S0-TS2	55.5		1411.90
S075-T1	43.5	NA	1439.80
S075-T2	43.5		1569.33
S075-TM1	43.5	40	1774.59
S075-TM2	43.5		1679.93
S075-TL1	43.5	600	1528.48
S075-TL2	43.5		1478.66
S075-TS1	43.5	600	1339.16
S075-TS2	43.5		1449.76
R0-N1	74.3	NA	1451.93

R0-N2	74.3		1676.43
R0-N3	74.3		1506.32
R0-DL1	81.9	150	2838.72
R0-DL2	82.7		2641.10
R0-CL1	84.2	100	3065.67
R0-CL2	68.6		2756.08
R0-DH1	81.8	150	2841.09
R0-DH2	81.8		2884.88
R075-N1	76.8	NA	2954.85
R075-N2	76.8		2476.52
R075-N3	78.8		2741.58
R075-DL1	79.2	150	3021.47
R075-DL2	75.9		3049.28
R075-CL1	78.9	100	3664.23
R075-CL2	81.1		3378.53
R075-DH1	76.6	150	3010.66
R075-DH2	78.9		3640.75
R150-N1	69.6	NA	2614.98
R150-N2	68.1		2515.31
R150-N3	68.1		2608.86
R150-DL1	69.2	150	3257.76
R150-DL2	62.3		2761.23
R150-CL1	69.6	100	3260.62
R150-CL2	62.0		3517.49
R150-DH1	68.1	150	2988.73
R150-DH2	69.2		3334.60

4.3 Results and discussion

4.3.1 Effect of steel fibers on cracking pattern

Controlling crack propagation is an influential property of SFRC. After the concrete cracks, the fibers bridge over the cracks and fully control the transfer of tensile stresses. These stresses are then transferred back to the concrete matrix through the bond action between the fibers and the concrete matrix [7]. All the plain concrete panels without reinforcement (Series S0-T and R0-N) failed when large vertical cracks propagated from the mid-height of the panel towards the bearing plates, resulting in the loss of integrity (Figures 4-3(a), 4-4(a)). The failure of these specimens can be identified as splitting of the strut. In contrast, the panels reinforced with fibers (Series S075-T, R075-N, and R150-

N) maintained their integrity upon failure (Figures 4-3(b), 4-4(b)), as smaller crack widths were observed along the length of the panel. This demonstrates the ability of fibers to control crack propagation and exhibit the fiber bridging effect.

Failure in square and rectangular panels from Series S0-TM, S0-TL, S0-TS, R0-DL, R0-CL, and R0-DH was initiated by a vertical splitting crack at the center of the panel and concrete crushing near the bearings, as indicated in Figures 4-3(c) and 4-4(c). In the vicinity of the bearing plate, severe spalling of the concrete was observed in these panel specimens. Although wider cracks were observed in these specimens, all the panel specimens maintained their integrity due to the provided reinforcement and failed as a result of strut crushing. Crushing of the strut can be identified when fan-shaped cracks begin to form near the bearing plate. The nodal region in the STM was indicated by fan shaped cracks.

The influence of fiber addition on spalling and crack width can be observed in Figure 4-3(d) and 4-4(d). After adding 0.75% fibers, SFRC panels exhibited good crack control and resistance to spalling compared to plain concrete panels. Furthermore, even with the addition of 1.5% fibers, crack control and resistance to spalling were significantly improved. However, no significant improvement in the compressive strength of the strut was observed after adding 1.5% fibers. Instead of forming dominant central cracks, many smaller cracks following the profile of bottle-shaped struts were observed in the SFRC panels. The pattern of failure observed in these specimens, which involved the crushing of the strut adjacent to a node, was similar to that of reinforced concrete specimens without fibers. Figure 4-5 depicts the stress-strain curves for the square and rectangular panels with 0.75% fiber addition.

doi:10.6342/NTU202403952

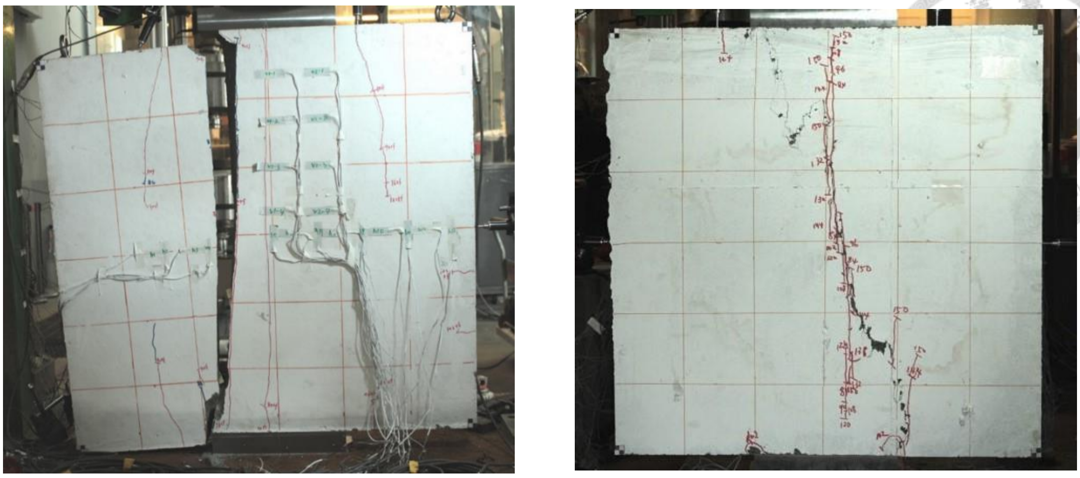

(a) Panel S0-T1 (b) Panel S075-T1

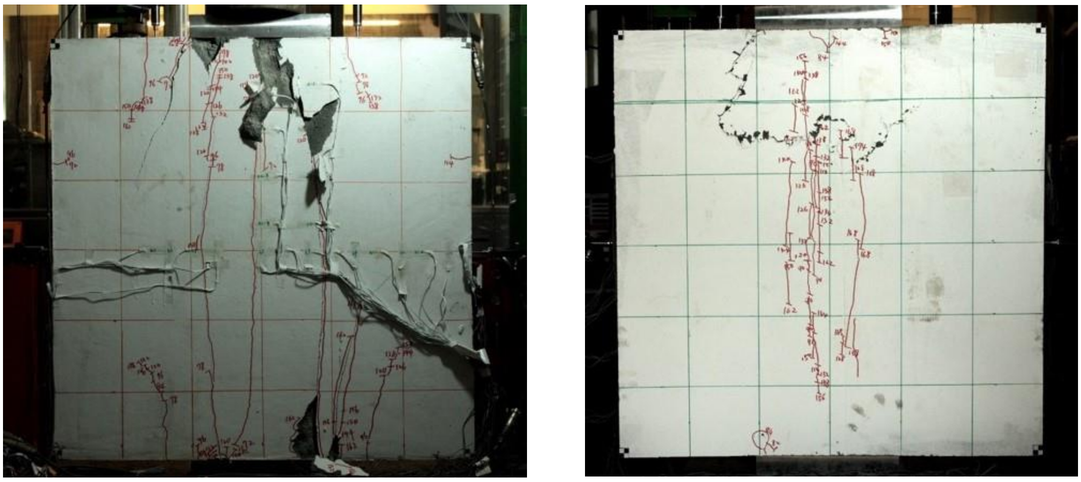

(c) Panel S0-TM1 (d) Panel S075-TM2

Figure 4-3 Representative failure modes in square panels

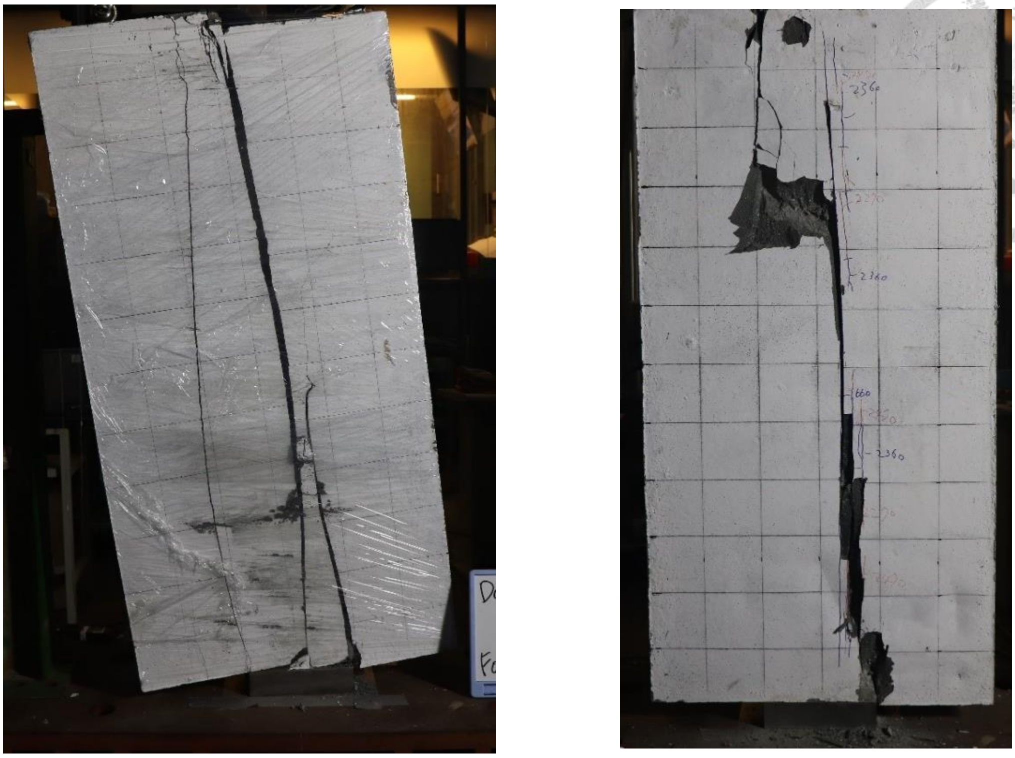

(a) Panel R0-N2 (b) Panel R075-N2

(c) Panel R0-CL2 (d) Panel R075-CL1

Figure 4-4 Representative failure modes in rectangular panels

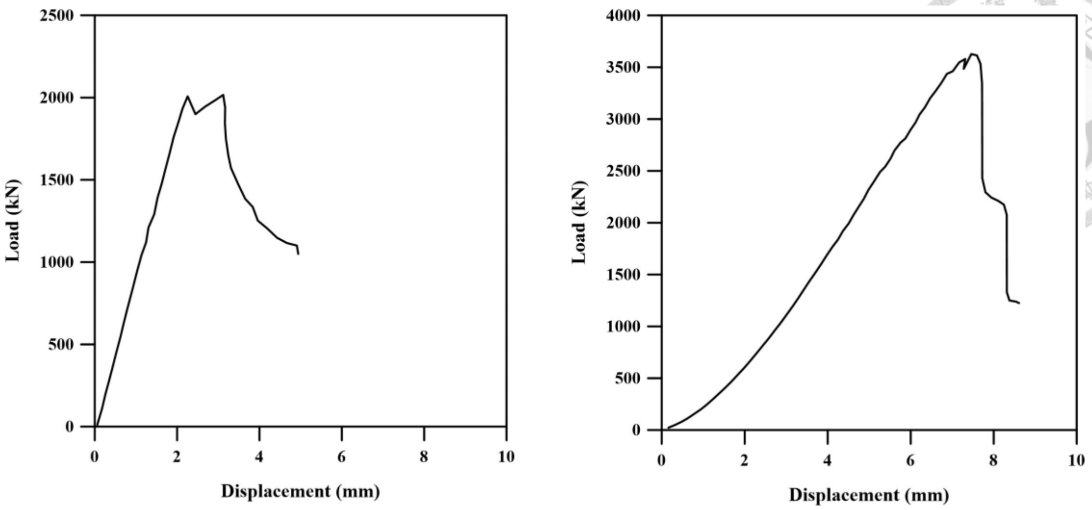

(a) Panel S075-TM2 (b) Panel R075-CL1

Figure 4-5 Stress-strain curves for panels

4.3.2 Crack width and spacing

The Figure 4-6 indicates that the width of cracks increases with the applied load for both square and rectangular panels. Instantaneous failure was observed in RC panels without reinforcement in the S0-T and R0-N series, therefore their results are not presented in Figure 4-6. At the ultimate loading stage, the maximum crack width observed in square specimens was 2.5 mm, while for rectangular specimens, it was 2 cm. These cracks penetrated through the panel's thickness, causing the panel to split into two pieces. However, after the addition of reinforcement, the crack width was maintained between 0.62 mm and 1.4 mm in square panels (S0-TM, S0-TL, and S0-TS), and between 1.5 mm and 4.0 mm in rectangular panels (R0-DL, R0-CL, R0-DH) as indicated in Figures 4-6(a) and 4-6(b). From Figures 4-6(c) and 4-6(d), compared to panels from the S0-T and R0-N series, with an increased fiber content of 0.75% exhibited a significant reduction in crack width, with a maximum value of 0.55 mm and 1.5 mm respectively in square and rectangular panels.

doi:10.6342/NTU202403952

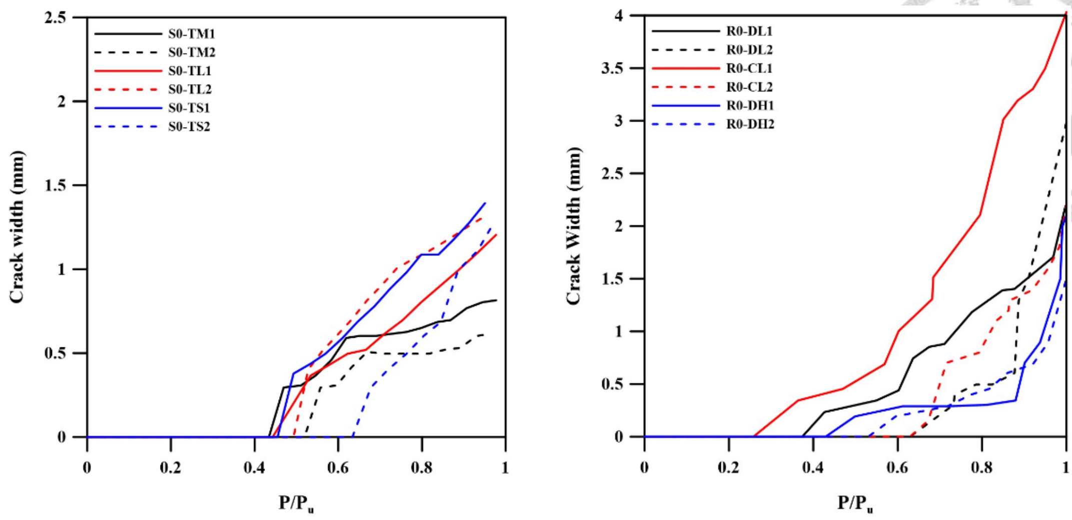

a) S0 Series b) R0 Series

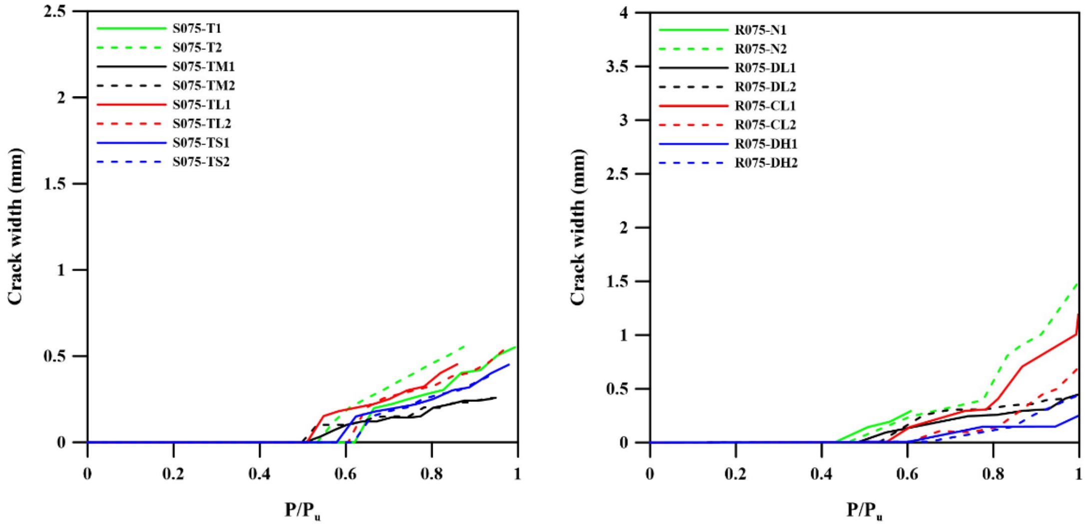

c) S075 Series d) R075 Series

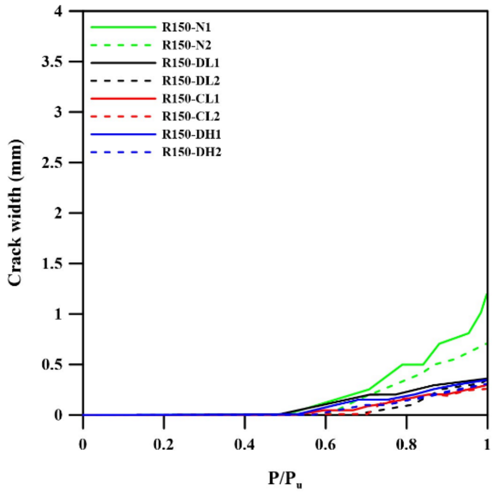

e) R150 Series

Figure 4-6 Crack widths observed in test panels

After adding 1.5% fibers (Figure 4-6(e)), the majority of rectangular specimens (R150) maintained a crack width of 0.25 mm. The incorporation of fibers in the S075, R075, and R150 series resulted in an adequate tension response due to the fiber's bridging effect. This effect controlled crack propagation and facilitated the transfer of tensile stresses. It also enabled higher stresses to be transmitted due to the smaller crack width. Among all the rectangular panels, the DH series exhibited the lowest crack width, likely due to its high reinforcement ratio. The TM series exhibited the lowest crack width among all the square panels, possibly due to its reinforcement layout.

4.3.3 Effect of reinforcement layout

Two different reinforcement layouts were used in the present study. The first layout represents distributed reinforcement (Series DL and DH). However, to represent the discrete tie location in the STM, the second layout involved providing reinforcement in bundles (Series TM, TL, TS, and CL). Bundled reinforcement provided at the mid-height of the specimens from the TM series formed a diamond-shaped refined STM, as shown in the Figure 4-1(a). Other specimens from the TL, TS, and CL series represented the general shape of the refined STM, where the tie formed at the location of the provided reinforcement, as indicated in the Figure 4-1(b), (c).

The compressive strength of the panels from the TM series was approximately 7% and 15% higher than that of the panels from the TL series after the addition of 0% and 0.75% fibers, respectively. However, this difference in compressive strength is not significant in the panels from the TL series. Therefore, it can be concluded that square panel specimens from the TM and TL series exhibited a similar level of performance despite having different reinforcement layouts. This similarity in compressive strength can be attributed to the fact that all these specimens failed due to the crushing of the strut,

doi:10.6342/NTU202403952

with the reinforcement contributing minimally. These observations align with the findings reported by Brown et al. [57].The panels from the TS series, characterized by reinforcing bars with lower yield strength, demonstrated a strength that was 10% and 20% lower than that of the panels from the TM series after the addition of 0% and 0.75% fibers, respectively. The difference in strength increased to 20% after the addition of fibers, indicating that the yield strength of the reinforcement has an impact on the compressive strength.

Among all the rectangular panel specimens, the highest compressive strength was observed in the panels from the CL and DL series, with no significant difference. Despite having a low reinforcement ratio, the reinforcement layout conforming to Figure 4-1(c) resulted in higher strength recorded in the panels from the CL series. This can be attributed to the effective reinforcement layout.

On the other hand, when comparing the average ultimate strength observed in the DL series with the CL series, at the same reinforcement ratio but with a different reinforcement layout, it was 14% and 11% lower than the CL series after the addition of 0.75% and 1.5% fibers, respectively. Therefore, it can be concluded that in rectangular panels, both the reinforcement ratio and the layout of the reinforcement have an impact on the ultimate strength. Providing reinforcement in bundles at the location of discrete ties affects the ultimate strength of the panel. Hence, the illustration provided by Brown et al. [57] for square panels, which indicates that lumping the reinforcement at the location of a discrete tie does not show a significant contribution, may not be applicable to rectangular panels.

4.3.4 Bar strain profile

Observations of the strain profile of the reinforcing bars in both rectangular and square panels, as shown in the Figure 4-7, indicate a large strain detected at the center of the transverse reinforcing bar. In RC panels (Series S0 and R0) (Figure 4-8(a)), prior to the concrete cracking, the strain profile was relatively consistent. However, after concrete cracking, the strain profile for the reinforcing bar became erratic and changed abruptly. From the bar strain profile for RC panel from R0 series, it was clearly observed that, with an increase in loading, the location of the discrete tie shifted away from the transverse axis. In other words, at the ultimate bearing capacity, the reinforcing bar farther from the transverse axis contributed more for resisting the tensile stresses, while at the initial loading stages, the center-provided reinforcing bars played a greater role in resistance. This phenomenon was clearly observed in the specimens from the R0-DL and R0-CL series, which is consistent with the observations made by Sahoo et al. (2008) [12]. However, in the case of the square RC and SFRC panels (Series S0-T, S0-TM, S0-TL, S0-TS), the location of tie remained at the center because bottle-shaped strut does not engage the full width of the panel, as a result the ILC’s will be curtailed, causing the critical loading case.

doi:10.6342/NTU202403952

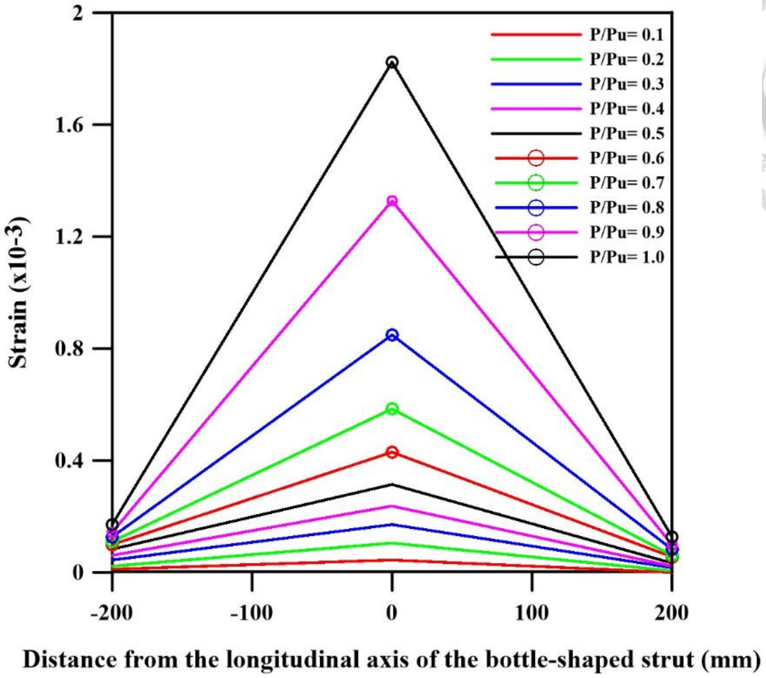

Figure 4-7 Typical strain profile for the transverse reinforcing bar

After the addition of fibers (Series R075, and R150) in SFRC rectangular panels, the enhanced ability to control crack propagation and reduce crack width resulted in all reinforcing bars indicating maximum strain at the ultimate loading stage (Figure 4-8(b)). However, upon studying the strain data for individual bars, it was observed that at the ultimate loading stage, the discrete tie changed its location away from the transverse axis of the panel. Furthermore, in the R0-DH series, the specimens exhibited lower strain compared to the R0-DL and R0-CL series, with the tie location shifted away from the transverse axis.

doi:10.6342/NTU202403952

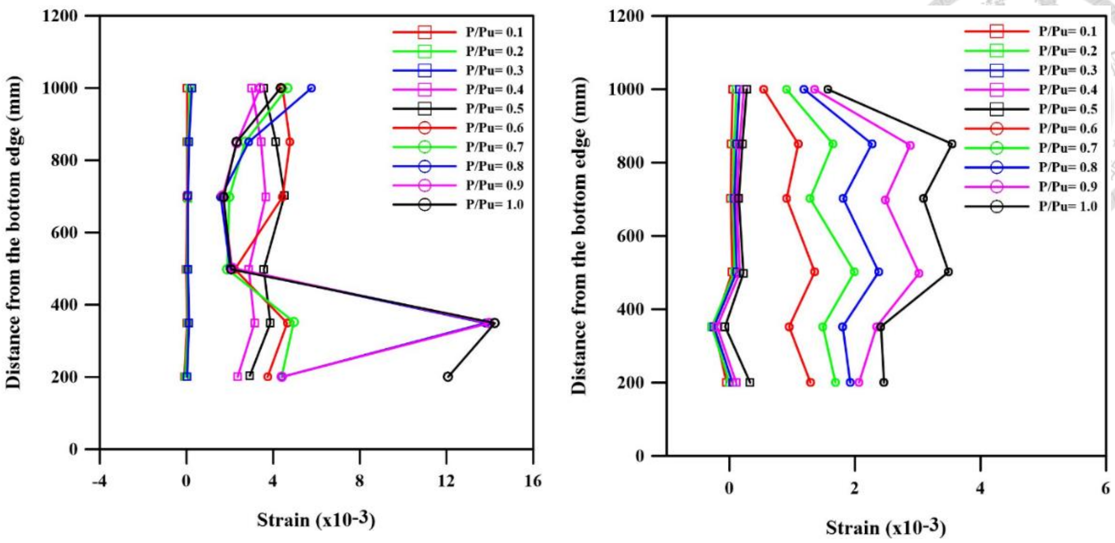

a) RC Panel b) SFRC Panel

Figure 4-8 Strain profile along the axis of the bottle-shaped strut

Based on the surface strain profile normal to the axis of the bottle-shaped strut as depicted in Figures 4-9(a) and 4-9(b), it can be concluded that in the case of square SFRC panels, the strut engages more than half the width of the panel. On the other hand, in rectangular SFRC panels, the strut engages nearly the full width of the panel.

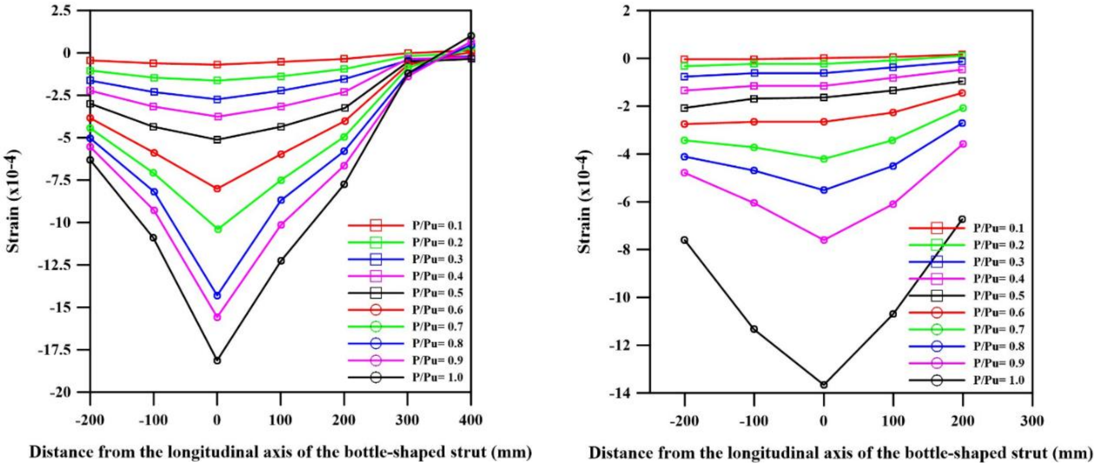

a) Square panels b) Rectangular panels

Figure 4-9 Vertical deformation of concrete on horizontal axis

4.4 Force Transfer Mechanism

At the peak compressive strength, the damage pattern in the isolated strut panels were observed. The diagonal cracks in SFRC panels tends to spread from the compression zone near the bearing plate where the ILC's are parallel to the direction of applied load, to the D-region where ILC's are spread laterally inducing the tension. In other words, when the load is applied to a relatively smaller area of the member, compressive forces spread laterally, inducing tensile stresses in the transverse direction to maintain the static equilibrium. This phenomenon gives rise to the formation of bottle shaped strut.

Before formulating the mathematical model, it is essential to determine the forces in the isolated strut panels. Considering a typical square and rectangular panel as depicted in Figure 4-10(a) and (b), both ends of the panels are supported over a bearing plate. Compression is transmitted from the loading plate to the supporting plate through strut-and-tie action. Where, the compression struts and tension ties are interconnected at the nodes, collaborating to resist applied loads. The Figure 4-11 indicates the average values of the angle of inclination of the strut (θ) for square and rectangular panels based on the crack pattern. However, measuring the exact value of θ is from the crack pattern is challenging due to the erroneous direction of the cracks, which may measure $\theta = 90°$. Using this value of θ in SST is not mathematically feasible. This value of θ will also overestimate the compressive strength of the isolated strut in the panels using the equilibrium approach. To avoid this computational error and to be on the conservative side, the location of the tie based on the strains in the horizontal reinforcing bar at the ultimate load stage was calculated, determining the value of θ as depicted in Table 4-5. Depending on the layout of the reinforcement, two different values are proposed for the rectangular panels, while for square panels, a single value is proposed. Based on this

doi:10.6342/NTU202403952

information, the softened Strut-and-Tie model is discussed and compared with the equilibrium approach.

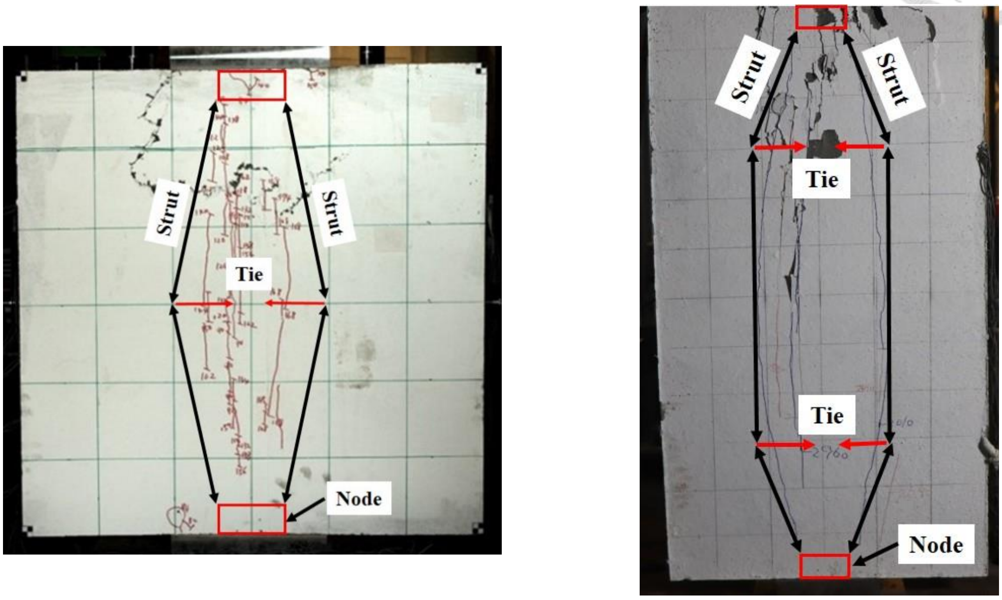

(a) (b)

Figure 4-10 Panels with strut-and-tie model

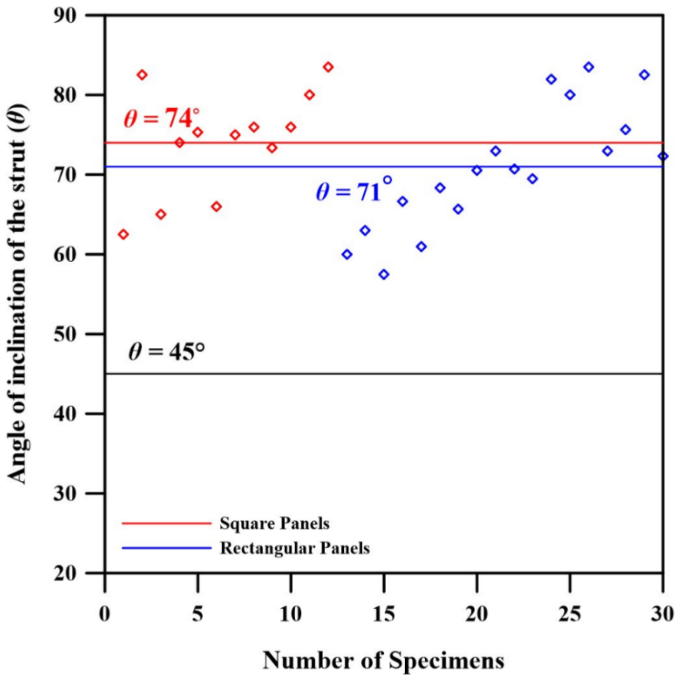

Figure 4-11 Angle of inclination of the strut based on crack pattern

Table 4-5 Angle of inclination of the strut in the Panel (with respect to horizontal axis)

	Series		
Angle of inclination of strut ($\boldsymbol{\theta}$)	**TM, TL, and TS**	**DL and DH**	**CL**
	$45°$	$49.40°$	$33.69°$

4.5 Review of SST

4.5.1 Force Equilibrium

As described in Figure 4-1, the diagonal compression strut is formed between loaded and supported face, indicating the diagonal mechanism. The angle of inclination of the diagonal compression strut (θ) with respect to the horizontal tie is defined as

$$\theta = tan^{-1}\left(\frac{l_v}{l_h}\right) \tag{4-1}$$

In case of the D-Region element, the stiffness ratio between the horizontal and diagonal mechanism and between the vertical and diagonal mechanism are defined in Eq. (4-2) and Eq. (4-3). The following models have been adopted from the studies of Schäfer (1996) [65] by Hwang & Lee (1999, 2002) [16,17].

$$R_h : R_d = \gamma_h : (1 - \gamma_h) \tag{4-2}$$

$$R_v : R_d = \gamma_v : (1 - \gamma_v) \tag{4-3}$$

The sum of these ratios of joint shear carried by the horizontal, vertical, and diagonal mechanisms is set equal to unity i.e. $R_h + R_v + R_d = 1$, and their values are defined as

$$R_h = \frac{\gamma_h(1 - \gamma_v)}{1 - \gamma_h\gamma_v} \tag{4-4}$$

$$R_v = \frac{\gamma_v(1 - \gamma_h)}{1 - \gamma_h\gamma_v} \tag{4-5}$$

$$R_d = \frac{(1 - \gamma_h)(1 - \gamma_v)}{1 - \gamma_h\gamma_v} \tag{4-6}$$

Where, γ_h and γ_v are the fraction of the forces transferred by the horizontal tie in the absence of a vertical tie and vertical tie in the absence of a horizontal tie, respectively.

$$\gamma_h = \frac{2\,tan\theta - 1}{3} \text{ for } 0 \leq \gamma_h \leq 1 \tag{4-7}$$

$$\gamma_v = \frac{2\,cot\theta - 1}{3} \text{ for } 0 \leq \gamma_v \leq 1 \tag{4-8}$$

4.5.2 Constitutive relations for concrete and reinforcement

In the context of Softened Strut-and-Tie (SST) model, cracked concrete is treated as a new material with distinct stress-strain characteristics, characterized by lower strength and stiffness when compared to uniaxially compressed concrete. This phenomenon, known as compression softening (Figure 4-12), has been appropriately addressed in the development of MCFT by Vecchio & Collins (1986) [14] and has also been quantified by Vecchio & Collins (1993) [86] and Belarbi & Hsu (1995) [39] to aid in the understanding of shear problems in reinforced concrete. The ascending branch of the softened stress-strain relationship for cracked concrete in compression and peak stress softening co-efficient is described in Eq. (4-9) and (4-10) respectively [40].

$$\sigma_d = \zeta f_c' \left[2\left(\frac{\varepsilon_d}{\zeta\varepsilon_0}\right) - \left(\frac{\varepsilon_d}{\zeta\varepsilon_0}\right)^2 \right] \text{ for } \frac{\varepsilon_d}{\zeta\varepsilon_0} \leq 1 \tag{4-9}$$

$$\zeta = min\left(\frac{5.8}{\sqrt{f_c'}}, 0.9\right) \times \frac{1}{\sqrt{1+400\varepsilon_r}} \tag{4-10}$$

Where, σ_d is principal compressive stress in concrete (negative quantity), f_c' is the maximum compressive stress observed in a cylinder test, ε_d and ε_r are the average principal strains respectively in the d and r directions, ε_o is strain in concrete cylinder at peak stress f_c'.

The value of principal tensile strain ε_r directly governs the extent of softening of concrete. This value can be determined from the relationship derived from the Mohr's circle for average strains (Figure 4-13). Hence

$$\varepsilon_r + \varepsilon_d = \varepsilon_h + \varepsilon_v \tag{4-11}$$

Here, the average normal strains in the h and v directions represented respectively as ε_h and ε_v. In SST model, the values of ε_h, ε_v, and ε_d are limited as 0.002, 0.002, and -0.001 respectively.

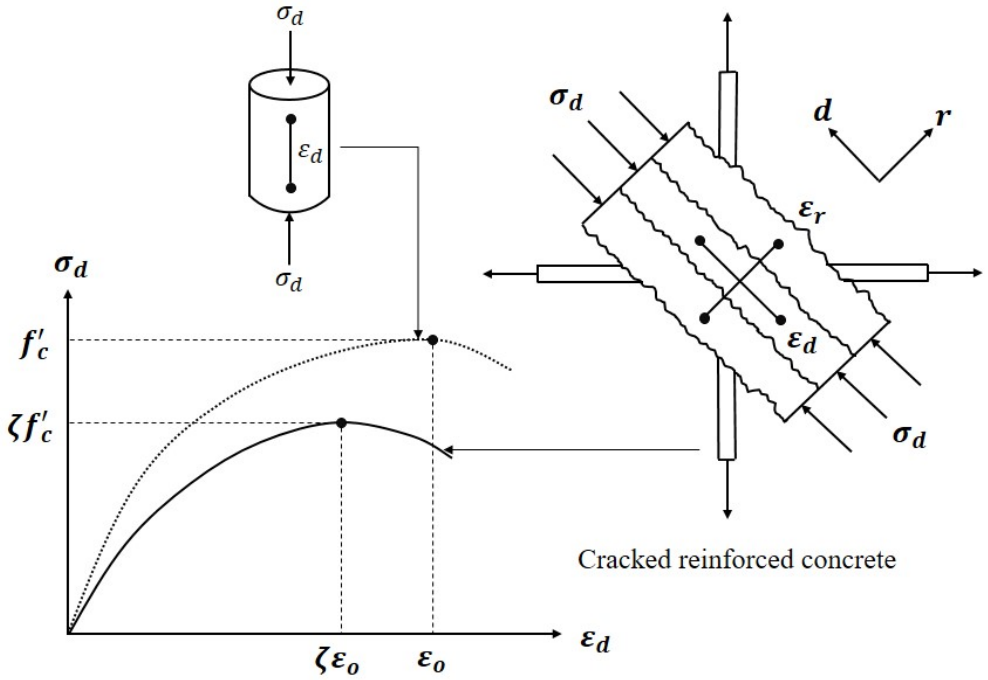

Figure 4-12 Stress-strain relationship for cracked concrete in compression

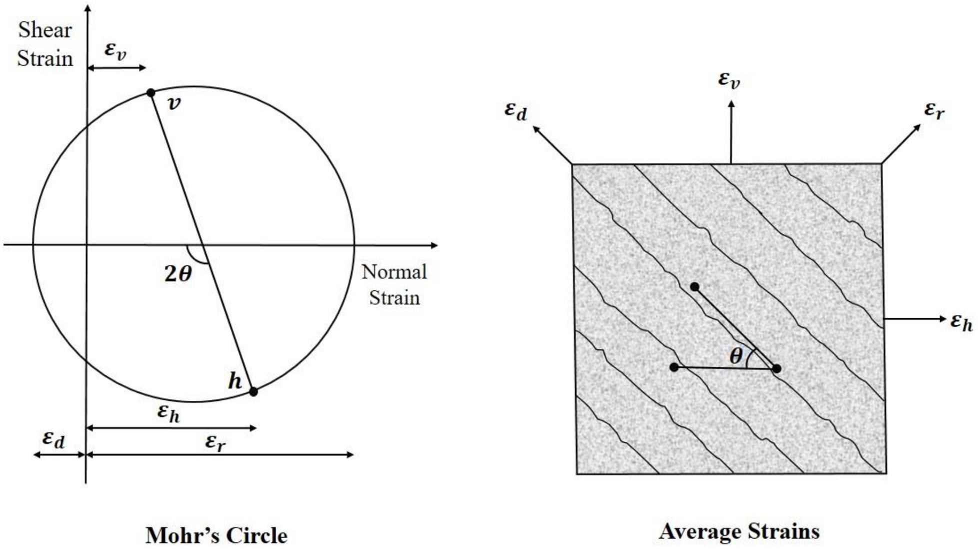

Mohr's Circle **Average Strains**

Figure 4-13 Compatibility conditions for cracked concrete

For steel reinforcing bars, the bilinear uniaxial stress-strain relationship, i.e., elastic-perfectly plastic, will be adopted. Therefore

$$f_s = E_s \varepsilon_s \text{ for } \varepsilon_s < \varepsilon_y \tag{4-12}$$

$$f_s = f_y \text{ for } \varepsilon_s \geq \varepsilon_y \tag{4-13}$$

Where, f_s and ε_s are the stress and strain in the steel reinforcing bars, respectively; E_s is modulus of elasticity of reinforcement. In the horizontal and vertical direction, f_s becomes f_h or f_v; similarly, ε_s becomes ε_h or ε_v. The yield strength of the bare reinforcing bar (f_y) becomes f_{yh} in the horizontal direction and f_{yv} in the vertical direction.

Tension forces in the ties in horizontal (F_h) and vertical (F_v) direction can be estimated from the following simplified constitutive equations,

$$F_h = A_{th} E_s \varepsilon_h \leq F_{yh} \tag{4-14}$$

$$F_v = A_{tv} E_s \varepsilon_v \leq F_{yv} \tag{4-15}$$

doi:10.6342/NTU202403952

Where, A_{th} and A_{tv} represents the areas of ties in horizontal and vertical direction, while F_{yh} and F_{yv} denote the yielding forces in each direction and calculated as follows,

$$F_{yh} = A_{th} f_{yh} \tag{4-16}$$

$$F_{yv} = A_{tv} f_{yv} \tag{4-17}$$

Compressive strength of the strut $(C_{d,n})$ can be calculated as follows.

$$C_{d,n} = K \zeta f_c' A_{str} \tag{4-18}$$

The strut-and-tie index (K) is defined as $K_h + K_v - 1$, and A_{str} is the effective area of the diagonal strut or nodal zone. These two parameters are discussed in detail in the following sections.

4.5.3 Strut-and-Tie Index

The contribution of the tension ties in enabling additional load carrying capacity, represented by the strut-and-tie index (K); where, $K \geq 1$. Based on the findings presented in Hwang & Lee (2002) [64], K can be estimated in the horizontal and vertical directions as follows,

$$K_h = 1 + (\overline{K_h} - 1)\left(F_{yh}/\overline{F_h}\right) \leq \overline{K_h} \tag{4-19}$$

$$K_v = 1 + (\overline{K_v} - 1)\left(F_{yv}/\overline{F_v}\right) \leq \overline{K_v} \tag{4-20}$$

Where, $\overline{F_h}$ and $\overline{F_v}$ are the balanced amount of tie forces at which the horizontal and vertical tie reaches yielding at failure, can be calculated accordingly, as follows

$$\overline{F_h} = \gamma_h \times (\overline{K_h} \zeta f_c' A_{str}) \times cos\theta \tag{4-21}$$

$$\overline{F_v} = \gamma_v \times (\overline{K_v} \zeta f_c' A_{str}) \times sin\theta \tag{4-22}$$

Within the elastic range, the horizontal tie reinforcement provides additional contribution when the strength of the strut is reached. To consider this contribution of the horizontal tie ($\overline{K_h}$), the following simplified equations proposed by Hwang & Lee (2002) has been adopted in this paper.

$$\overline{K_h} = \frac{1}{1 - 0.2(\gamma_h + \gamma_h^2)} \tag{4-23}$$

$$\overline{K_v} = \frac{1}{1 - 0.2(\gamma_v + \gamma_v^2)} \tag{4-24}$$

4.5.4 Application of SST for panels

The geometric properties and the strut-and-tie model for a typical panel specimen are illustrated in Figure 4-14(a). One of the key input parameters is the angle of inclination of the strut (θ), which, according to the force transfer mechanism, is calculated according to Table 4-5. Hence, the proposed model for all panel specimens tested in this study adopts these values for the calculation. The values of θ and l_h determine the location of the tie. The number of reinforcing bars on and above the tie location are taken into account for calculating the strength of the strut. Additionally, the method for calculating the length of the strut (l_s) and the effective area on the nodal zone of the strut (A_{str}) are illustrated in Figure 4-14(b), where a_p represents the half length of the bearing plate. The depth of the compression zone can be estimated by assuming the depth as a_p. The analysis method proposed in this study is depicted in Figure 4-15. Following this method, the compressive strength of the strut ($C_{d,n}$) is calculated from one side only. This value, $C_{d,n}$, should then be multiplied by $\sin\theta$ to calculate its vertical component. By considering the effects from both sides of the panel along the axis of symmetry, the compressive strength of the panel P_{ucal} can be determined.

doi:10.6342/NTU202403952

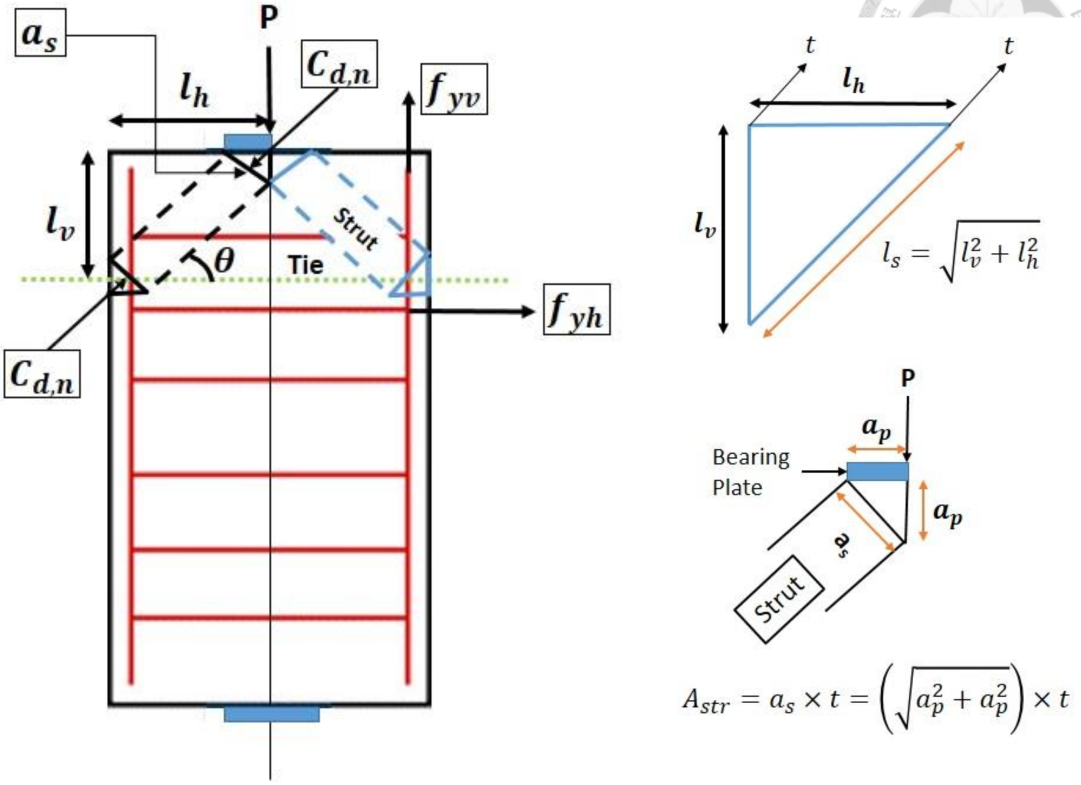

(a) (b)

Figure 4-14 Illustration of strut-and-tie model for Panel

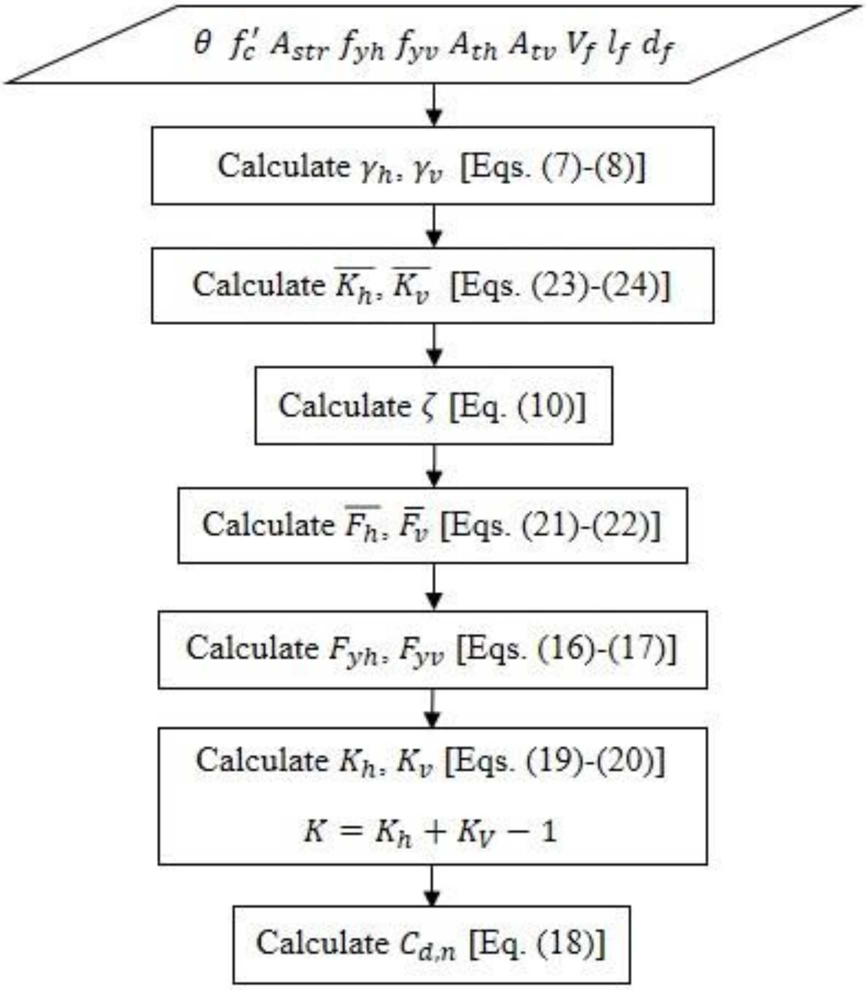

Figure 4-15 Algorithm for calculating the compressive strength of bottle-shaped strut

4.5.5 Results and discussion

In this study, both RC and SFRC square and rectangular specimens were tested to verify the proposed analysis procedure. The test variables included the panel aspect ratio, the location of the reinforcement, the fiber volume fraction, and the reinforcement ratio. The analysis also incorporates data collected from the literature. Specimens that failed due to strut failure were included in the analysis, while those subjected to varying concentration ratios using bearing plates of different lengths on the loaded and supported faces were excluded. Additionally, panels that failed due to splitting of the strut were not considered. Consequently, panels without transverse reinforcement (Series T and N) were omitted from the analysis. The compressive strength of the concrete in the panels ranged from less than 40 MPa in the literature to approximately 70 MPa in the present study. Various test variables were considered, including the panel aspect ratio, the location of the reinforcement, and the reinforcement ratio. The dataset comprised 34 rectangular panels and 18 square panels. Analysis of the results (Figure 4-16) indicates an underestimation of the compressive strength of the bottle-shaped strut. The proposed analysis procedure, as shown in Figure 4-15, yielded a mean strength ratio (P_u/P_{ucal}) of 2.74 and a coefficient of variation (CoV) of 58.40%.

In the SST, among the test variables considered, a major factor missing is the effect of fiber addition. The addition of fibers in plain concrete substantially enhances its post-cracking response, including ductility, toughness, strain hardening, crack control characteristics [8,11,41,87]. This resulting in a different material softening phenomenon in SFRC as compared to RC panels. Moreover, the softening of the material is proportional to the principal tensile strain value ε_r. Therefore, it becomes necessary to define the values of $\varepsilon_h, \varepsilon_v$, and ε_d for SFRC material, which can be obtained from strain gauge readings and readings from NDI markers.

Based on the above discussion, modifications should be made to the yielding forces of the horizontal and vertical ties (F_{yh} and F_{yv}), the softening coefficient of the material (ζ), and the average strains ($\varepsilon_r, \varepsilon_h, \varepsilon_v$, and ε_d) should be adjusted for SFRC material. The discussion regarding the modification of SST for SFRC panels is provided in the next section.

doi:10.6342/NTU202403952

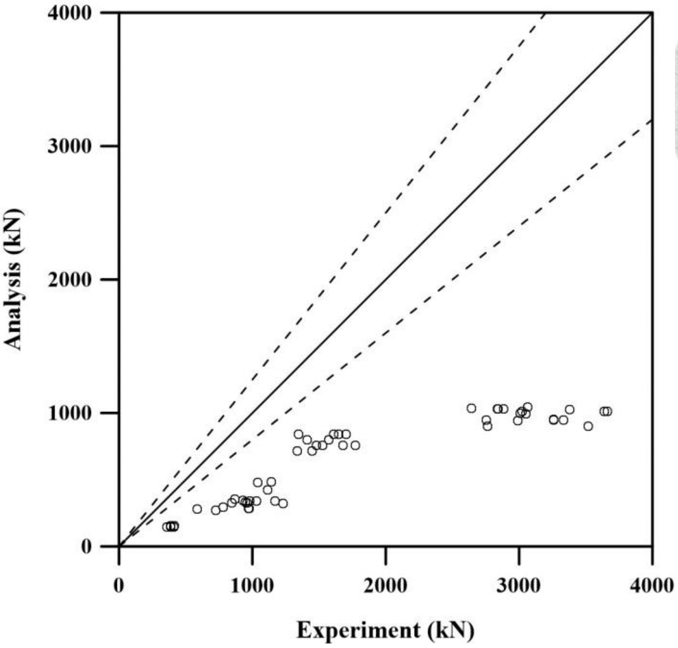

Figure 4-16 Comparison between experimental and proposed analysis prediction results

4.6 Modification of SST for SFRC

The peak stress softening coefficient ζ is calculated by considering the effect of steel fiber addition. The equation proposed by Zhang & Hsu [40], originally derived by Belarbi & Hsu [39], at the University of Houston, is adopted and modified by Hung [84], through regression analysis of available test data. This equation also accommodates the effects of fiber volume fraction (V_f) and fiber aspect ratio $\left(l_f/d_f\right)$, with the bond strength of steel fiber $\left(\tau_{eq}\right)$ as given in Eq. (4-25)

$$\zeta = (1 + 0.07S_f) \times min\left(\frac{5.8}{\sqrt{f_c'}}, 0.9\right) \times \frac{1}{\sqrt{1+400\varepsilon_{r(SFRC)}}} \text{ Where,} \tag{4-25}$$

$$S_f = \tau_{eq} \times V_f \times \left(\frac{l_f}{d_f}\right)$$

In line with the previous discussion, the bond strength value of 8 MPa, as proposed by Perceka & Liao [88], can be employed for calculating ζ. Furthermore, Hung [84] introduced modifications to Eq. (4-11), taking into account the properties of fibers

$$\varepsilon_{r(SFRC)} = \frac{\varepsilon_h + \varepsilon_v - \varepsilon_d}{(0.1S_f) + 1} \tag{4-26}$$

As depicted in Figures 4-17(a) and 4-17(b), the electrical resistance strain gauge attached to the surface of the reinforcing bars provides ε_h and ε_v, limited to 0.003 and -0.003, respectively. Additionally, for SFRC, ε_d, derived as -0.003 (Figure 4-17(c)), is based on the displacement of the NDI markers on the concrete surface. However, for RC, ε_d is adopted directly as -0.001 from Hwang & Lee (2002) [64]. The value of ε_r in the present study is directly obtained from experimental results, or alternatively, it can be estimated from Eq. (4-26).

The values of ε_h, ε_v, and ε_d proposed in this study differ from those proposed by Hwang & Lee (1999) [16], primarily due to the yield strength of the reinforcement and use of normal strength concrete. This study specifically focuses on the use of high-strength reinforcement and concrete. Since, the experimental results for the panel test indicated the concrete strut failure before yielding of the reinforcement, therefore, ε_h is considered as 0.003 for calculation.

doi:10.6342/NTU202403952

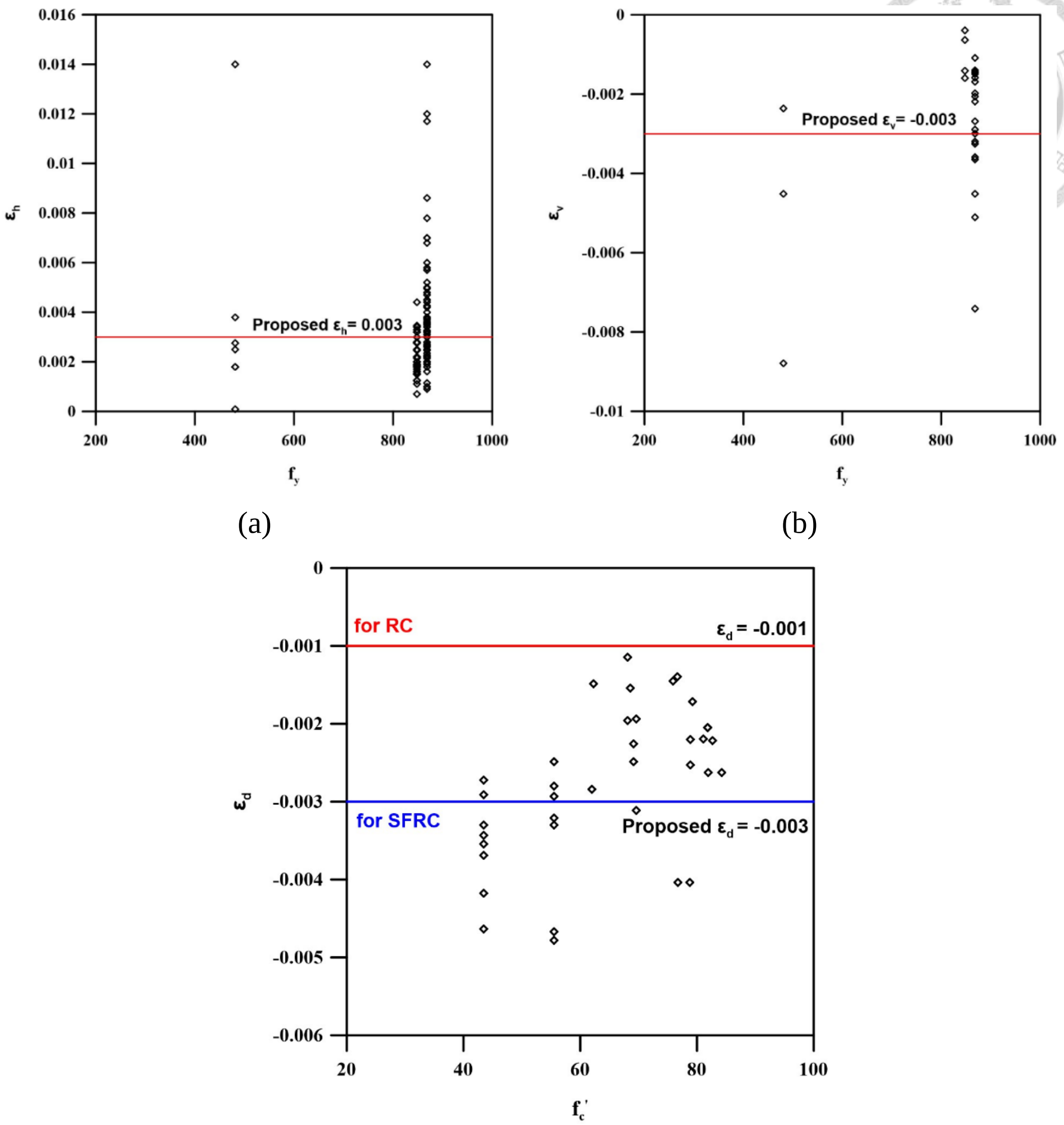

(a) (b)

(c)

Figure 4-17 Effect of high-strength reinforcement and concrete on average strains

In concrete panel, because of the tension cracking, the reinforcing bars bridge over the crack and exhibits higher resistance to tension. Similarly, the orientation and distribution of fibers also affect the panel's resistance to tension. To account for these effects, Eq. (4-16) and (4-17) were modified as follows.

$$F_{yh} = (A_{th} f_{yh} \times 10^{-3}) + (l_s \times f_{c1} \times t \times sin\theta \times 10^{-3}) \qquad (4\text{-}27)$$

$$F_{yv} = (A_{tv} f_{yv} \times 10^{-3}) + (l_s \times f_{c1} \times t \times cos\theta \times 10^{-3}) \qquad (4\text{-}28)$$

f_{c1} indicates the tensile stress in SFRC. Based on the statistical mechanics of composite materials, Naaman (1972) [77] proposed an equation for the calculation of f_{c1} which is further modified by Wagh et al. (2023) [8] by limiting the $\varepsilon_{pc} = 0.007$ is adopted

$$f_{c1} = \sigma_{cc} + \frac{\sigma_{pc} - \sigma_{cc}}{0.007 - \varepsilon_{cc}} \times (\varepsilon_{\mathrm{r}} - \varepsilon_{cc}) \tag{4-29}$$

The parameters, σ_{cc} and σ_{pc}, represent the initial cracking and post-cracking strengths of the concrete, while ε_{cc} and ε_{pc} denote the cracking strain and maximum strain within the concrete, respectively. These parameters are determined through the following derivation:

$$\varepsilon_{cc} = \frac{\sigma_{cc}}{E_c} \text{ where, } E_c = 0.8 \times 4700\sqrt{f_c{}'} \tag{4-30}$$

$$\sigma_{cc} = \sigma_{mu}\left(1 - V_f\right) + \alpha\tau_{eq}V_f\left(\frac{l_f}{d_f}\right) \tag{4-31}$$

$$\sigma_{pc} = \lambda\tau_{eq}V_f\left(\frac{l_f}{d_f}\right) \tag{4-32}$$

The modulus of elasticity of the concrete (E_c), expressed in MPa. The average tensile strength of the matrix, σ_{mu}, can be calculated as $0.56\sqrt{f_c'}$. The multiplying coefficient $\alpha = 0.1 \times 2/\pi \times 1$, representing the average contribution of bond at onset of matrix cracking, fiber orientation factor, and reduction factor for bond strength at fiber matrix interface. The multiplying coefficient $\lambda = 0.25 \times (4 \times 2/\pi) \times 1 \times 1$, representing average fiber pull-out length, orientation effect, group reduction, and reduction due to spalling of the wedge. The values of α and λ has been adopted in this paper from in this paper Liao et al. (2017) [87].

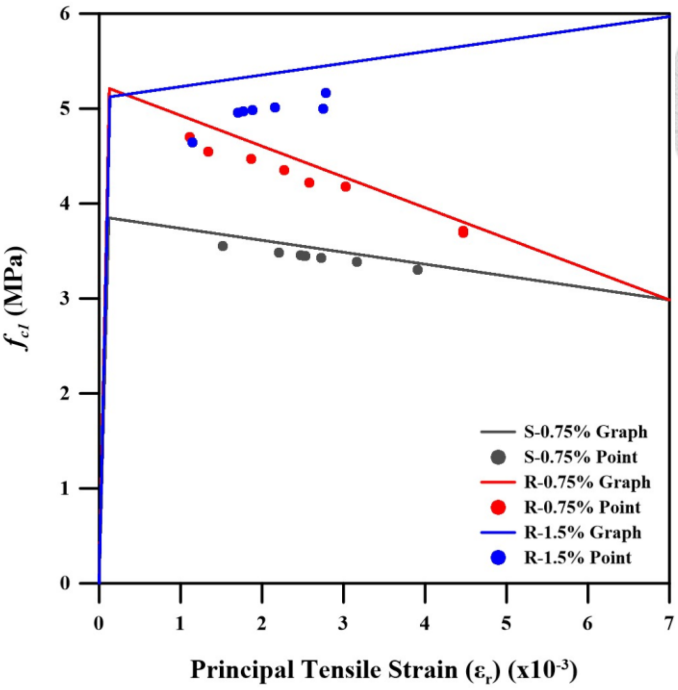

Figure 4-18 Principal tensile stress in SFRC

The Figure 4-18 shows the relationship between principal tensile strain (ε_r) and principal tensile stress in concrete (f_{c1}). The variables "S" represents the square panels and "R" represents the rectangular panel. The graphs (in line format) indicating the general behavior of SFRC for 0.75% and 1.5% fibers, representing the initial response until cracking followed by the line joining the cracking and post-cracking stress. These lines are plotted after considering $\tau_{eq} = 8\ MPa$ as proposed by Perceka & Liao [88] and the value of average compressive strength of concrete cylinder for each fiber volume fraction. All the graphs representing general behaviour of SFRC are plotted up to maximum post-cracking strain of 0.007.

Based on the value of principal tensile strain, the value of principal tensile stress in concrete were calculated for each panel and indicated in the form of point (or dot). In the Figure 4-18, most of the points for SFRC panels are in between the σ_{cc} and σ_{pc}. Therefore the formula for calculating the principal tensile stress Eq. (4-29) is valid for calculating the resistance from fibers and thereby, yielding forces (F_{yh}) in the tensile ties. Addition

doi:10.6342/NTU202403952

of fibers shows strain hardening behaviour for 1.5% fibers. However, the response of SFRC with fibers lower than 1.5% shows strain softening behaviour with large energy dissipation.

4.6.1 Test verification

The predicted compressive strength of the bottle-shaped strut is compared with the test results using the proposed analysis procedure in Figure 4-19(a). Additionally, Figure 4-19(b) compares the proposed analysis procedure with the equilibrium approach. As evident from the Figure 4-19(a), the analysis results are conservative, nevertheless they exhibit good agreement compared to the equilibrium approach. A detailed example for calculating the compressive strength of a bottle-shaped strut is presented in section 4.6.1.1. Thirty specimens from this study and twenty-two specimens from the literature, as indicated in Appendix B, were analyzed using the proposed SST. The calculated results indicated that the strength ratio (P_u/P_{ucal}) had a mean of 2.195 and a coefficient of variation of 33.62%. Any discrepancy in the compressive strength of the bottle-shaped strut is primarily attributed to the angle of inclination of the strut (θ), governing the calculated strength. The underestimation of results arises because θ is derived from the strains in the reinforcing bars at the ultimate load stage and not from the crack pattern of the concrete surface. Moreover, the calculated results obtained for the RC panels from the proposed analysis procedure are more conservative than the results for SFRC panels. This is possibly because the value of ε_r recorded for the RC panels at the ultimate loading stage were higher than the SFRC panels.

Conversely, for the equilibrium approach (Figure 4-19(b)), the strength ratio has a mean of 4.147 and a coefficient of variation of 51.56%, with a difference of 52.92%

doi:10.6342/NTU202403952

compared to the proposed analysis procedure. It is evident that the equilibrium approach is more conservative for the angle of inclination of the strut given in Table 4-5.

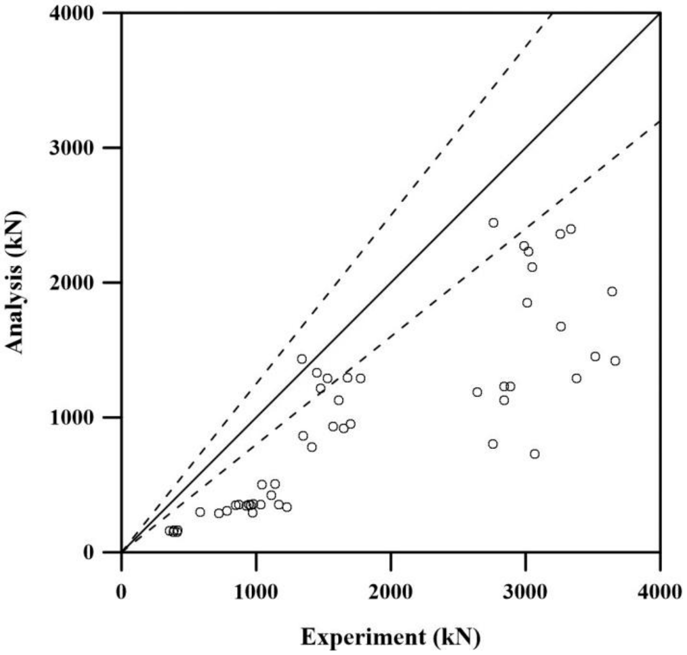

(a) Proposed SST

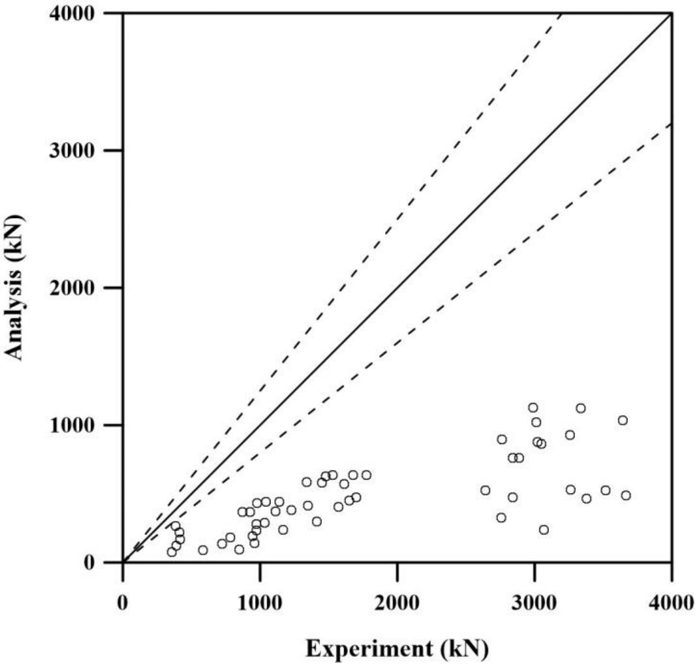

(b) Equilibrium Approach

Figure 4-19 Compressive strength of bottle-shaped struts calculated using the proposed SST and Equilibrium Approach

doi:10.6342/NTU202403952

4.6.1.1 Sample calculation for panel under compression

Given Parameters	**Panel ID: R150-DL1** $\boldsymbol{P_u = 3257.755kN}$ 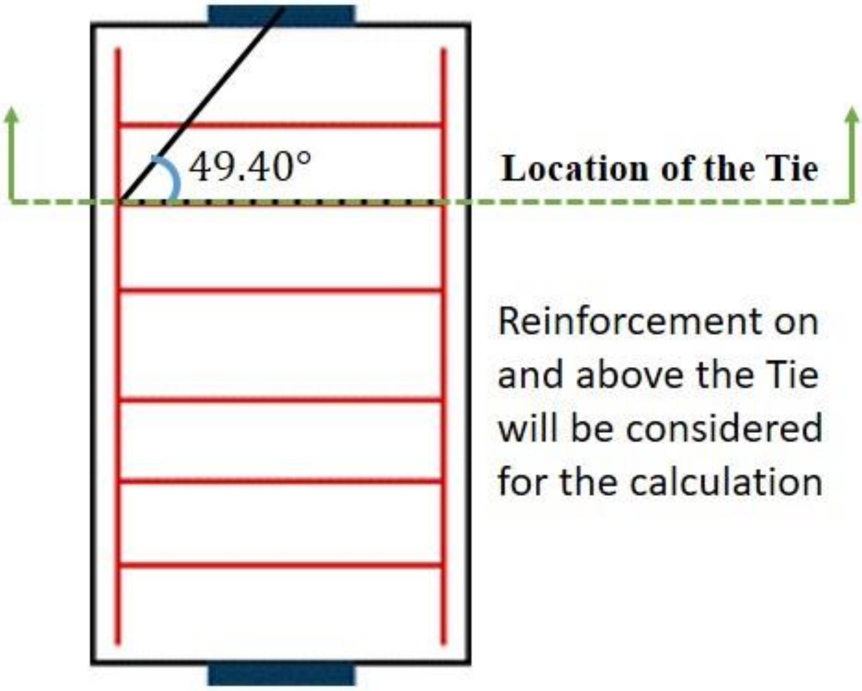 Illustration for panel R150-DL1
	Panel Dimensions: $1200 \times 600 \times 150mm$ Number of bars in horizontal Direction = 6 nos. Number of bars in vertical Direction = 2 nos. Area of Horizontal Bar =$129mm^2$ Area of Vertical Bar =$71mm^2$ $f_y = 600MPa$ $f_c' = 69.17MPa$ $\varepsilon_r = 0.001884$ $V_f = 0.015$ $l_f = 30mm$ $d_f = 0.38mm$ $\alpha = 0.063$ $\lambda = 0.63$ $\tau_{eq} = 8MPa$

Solution

Step 1: **Calculation of l_v, l_s, and A_{str}**

for $\theta = 49.40°$ (DL Series)

$l_v = 350mm$ and,

$l_s = 460.97mm$

$A_{str} = 21213.2mm^2$

Step 2: **Properties of SFRC**

$$\sigma_{cc} = \sigma_{mu}\left(1 - V_f\right) + \alpha\tau_{eq}V_f\left(\frac{l_f}{d_f}\right)$$

$$\therefore \sigma_{cc} = [4.66(1 - 0.015)] + \left[0.063 \times 8 \times 0.015 \times \frac{30}{0.38}\right] = 5.184MPa$$

$$\sigma_{pc} = \lambda\tau_{eq}V_f\left(\frac{l_f}{d_f}\right)$$

$$\therefore \sigma_{pc} = 0.63 \times 8 \times 0.015 \times \frac{30}{0.38} = 5.968MPa$$

$$f_{c1} = \sigma_{cc} + \frac{\sigma_{pc} - \sigma_{cc}}{0.007 - \epsilon_{cc}} \times (\epsilon_{\mathrm{r}} - \epsilon_{cc})$$

$$\therefore f_{c1} = 5.184 + \frac{5.968 - 5.184}{0.007 - 0.000166} \times (0.001884 - 0.000166)$$

$$= 5.384MPa$$

Step 3: **Yielding forces of the ties**

$$F_{yh} = (A_{th}f_{yh} \times 10^{-3}) + (l_s \times f_{c1} \times t \times sin\theta \times 10^{-3})$$

$$\therefore F_{yh} = (2 \times 129 \times 600 \times 10^{-3}) + (460.97 \times 5.384 \times 150$$

$$\times sin49.4° \times 10^{-3}) = 437.46kN$$

$$F_{yv} = (A_{tv}f_{yv} \times 10^{-3}) + (l_s \times f_{c1} \times t \times cos\theta \times 10^{-3})$$

$$\therefore F_{yv} = (1 \times 71 \times 600 \times 10^{-3}) + (460.97 \times 5.382 \times 150 \times cos 49.4° \times 10^{-3}) = 284.78kN$$

Step 4: Force distribution

$$\gamma_h = \frac{2\ \tan\theta - 1}{3} = \frac{2\ \tan 49.4° - 1}{3} = 0.444$$

$$\gamma_v = \frac{2\ \cot\theta - 1}{3} = \frac{2\ \cot 49.4° - 1}{3} = 0.238$$

Step 5: Balanced amounts of tie forces

$$\overline{K_h} = \frac{1}{1 - 0.2(\gamma_h + \gamma_h^2)} = \frac{1}{1 - 0.2(0.444 + 0.444^2)} = 1.147$$

$$\overline{K_v} = \frac{1}{1 - 0.2(\gamma_v + \gamma_v^2)} = \frac{1}{1 - 0.2(0.238 + 0.238^2)} = 1.063$$

Step 6: Softening of concrete

$$\zeta = \left(1 + 0.07S_f\right) \times min\left(\frac{5.8}{\sqrt{43.5}},\ 0.9\right) \times \frac{1}{\sqrt{1 + 400 \times 0.001884}} = 0.876$$

Where, $S_f = 0.015 \times \frac{30}{0.38} \times 8$

$$\overline{F_h} = \gamma_h \times (\overline{K_h}\zeta f_c' A_{str}) \times \cos\theta$$

$$\therefore \overline{F_h} = 0.333 \times 1.098 \times 0.876 \times 69.17 \times 21213.2 \times cos 49.4° = 426.521kN$$

$$\overline{F_v} = \gamma_v \times (\overline{K_v}\zeta f_c' A_{str}) \times \sin\theta$$

$$\therefore \overline{F_v} = 0.333 \times 1.098 \times 0.876 \times 69.17 \times 21213.2 \times sin 49.4° = 246.851kN$$

Step 7: Tie index

$$K_h = 1 + (\overline{K_h} - 1)\left(F_{yh}/\overline{F_h}\right)$$

doi:10.6342/NTU202403952

$$\therefore K_h = 1 + (1.147 - 1)\left(\frac{437.46}{426.521}\right) = 1.151 > \overline{K_h}$$

take, $K_h = 1.147$

$$K_v = 1 + (\overline{K_v} - 1)(F_{yv}/\overline{F}_v)$$

$$\therefore K_v = 1 + (1.063 - 1)\left(\frac{284.78}{246.851}\right) = 1.072 > \overline{K_v}$$

take, $K_v = 1.063$

Step 8: **Compressive strength of the bottle-shaped strut**

$$C_{d,n} = (K_h + K_v - 1)\zeta f_c' A_{str}$$

$$\therefore C_{d,n} = (1.147 + 1.063 - 1) \times 0.876 \times 69.17 \times 21213.2$$

$$= 1555.297 \text{ kN}$$

$$P_{ucal} = 2 \times 1555.297 \times sin 49.4° = 2361.785 \text{kN}$$

Strength Ratio

$$\frac{P_u}{P_{ucal}} = \frac{3257.755}{2361.785} = 1.379$$

4.7 Sensitivity analysis

The sensitivity of the modified SST for SFRC is analyzed by considering the following 2 conditions given in Table 4-6. Table also provides the difference between Condition 1 & 2 from Modified SST for SFRC. The equation for softening coefficient proposed by Vecchio & Collins [14] at the University of Toronto is checked for its effect on the calculated results by using the Modified SST for SFRC.

doi:10.6342/NTU202403952

Table 4-6 Conditions for sensitivity analysis

Condition	**Parameter**	**Equation**
Modifies SST for SFRC	ζ	$(1+0.07S_f)\times min\left(\frac{5.8}{\sqrt{f_c'}},0.9\right)\times\frac{1}{\sqrt{1+400\varepsilon_{r(SFRC)}}}$
	τ_{eq}	8 MPa
Condition 1	ζ	$(1+0.07S_f)\times min\left(\frac{5.8}{\sqrt{f_c'}},0.9\right)\times\frac{1}{\sqrt{1+400\varepsilon_{r(SFRC)}}}$
	τ_{eq}	Based on Section 2.4
Condition 2	ζ	$\left(\frac{1}{0.8-0.34(\epsilon_1/\epsilon_c')}\right)\leq 1$
	τ_{eq}	Based on Section 2.4

The analysis of the modified SST for SFRC, Condition 1, and Condition 2 is presented in the following Figure 4-20. The graphical representation in Figure 4-20 (a) shows that the modified SST for SFRC and Condition 1 yield identical results, with a mean of 2.20, a standard deviation of 0.74, and a coefficient of variation of 33.63%, despite the different values of τ_{eq}. This similarity occurs because the strut-and-tie index is governed by the conditions $K_h \leq \overline{K_h}$, and $K_v \leq \overline{K_v}$. For calculating $C_{d,n}$, the value of τ_{eq} only affects the strut-and-tie index. These three conditions in Table 4-6 consistently underestimate compressive strength, as evidenced by the majority of data points lying above the 1.0 line on the graph. In contrast, Condition 2, which employs the MCFT approach for determining ζ, exhibits predictions more close to the experimental values. With a mean of 1.74, standard deviation of 0.52, and coefficient of variation of 29.55%, this condition demonstrates improved accuracy.

The effects of fiber volume fraction, concrete compressive strength, and transverse reinforcement on the compressive strength predictions are shown in Figure 4-20(b), (c), and (d). The trend for the data from the modified SST for SFRC and Condition 1 is steeper, indicating that $\frac{P_u}{P_{ucal}}$ becomes closer to 1 as the fiber volume content increases Figure 4-

20(b). The flatter trend in Condition 2 suggests that the softening coefficient does not account for the effect of fiber addition.

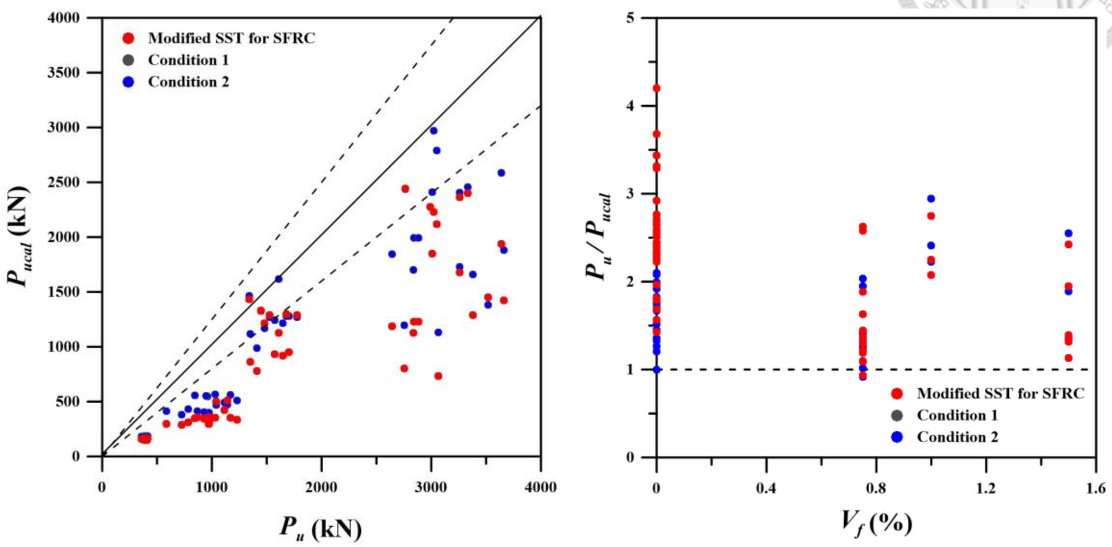

(a) Comparison of Modified SST for SFRC with condition 1 & 2

(b) Effect of fiber volume fraction on strength prediction

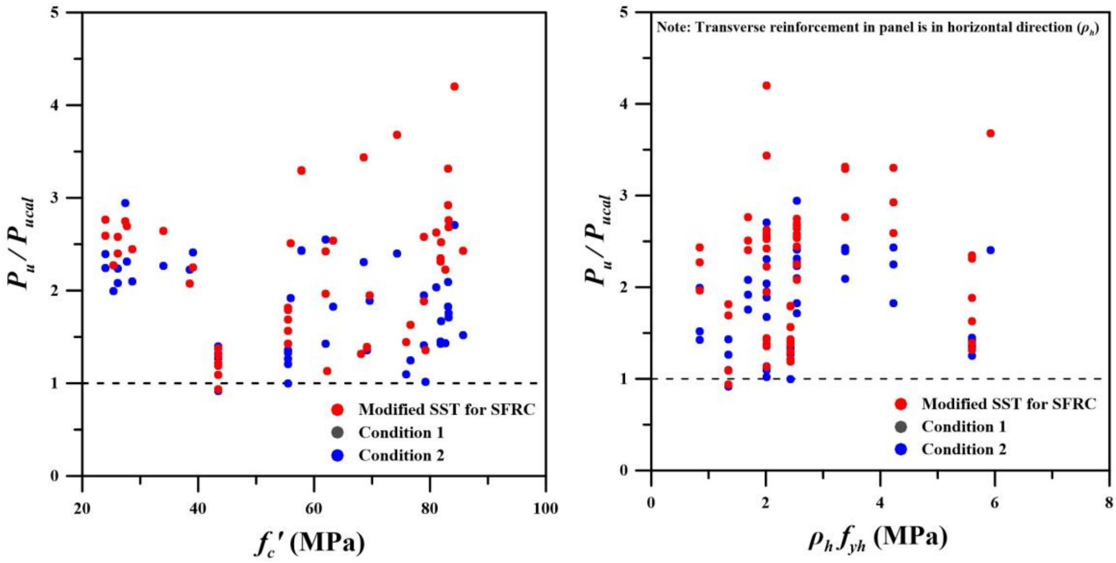

(c) Effect of concrete compressive strength on strength prediction

(d) Effect of transverse reinforcement on strength prediction

Figure 4-20 Sensitivity analysis of calculated compressive strength

The graphs showing the effects of concrete compressive strength (Figure 4-20(c)) and the transverse reinforcement ratio (Figure 4-20(d)) do not display any visible trends, indicating consistency in the predictions.

4.8 Summary

HSC and bottle-shaped struts typically experience brittle failure due to transverse tensile forces (splitting forces). Researchers believe SFRC's ability to transform brittle behavior into ductile behavior might be beneficial in these cases, potentially reducing the need for additional transverse reinforcement.

To explore this possibility, the study proposes a new analytical framework based on the strut-and-tie method (SST). The Modified SST for SFRC can predict the compressive strength of bottle-shaped struts in SFRC elements under in-plane compression. It considers factors like geometry, reinforcement ratio, and steel fiber content, along with realistic SFRC material properties like strain hardening and peak stress softening. The Table 4-7 indicates the principal difference between Modified SST for SFRC and original SST. This comprehensive approach aims to provide a deeper understanding of how SFRC bottle-shaped struts behave under compressive load.

Additionally, new limits for principal tensile strains are proposed for SFRC. This is because adding fibers reduces the size and spacing of cracks, minimizes spalling, and helps resist tensile stresses along with the reinforcement.

The accuracy of this new model was validated by comparing its predictions with experimental results, demonstrating its effectiveness in estimating the ultimate compressive strength of bottle-shaped struts.

Table 4-7 Comparison of Modified SST for SFRC with original SST

Parameter	SST	SST for SFRC
$\boldsymbol{F_{yh}}$	$(A_{th}f_{yh} \times 10^{-3})$	$(A_{th}f_{yh} \times 10^{-3}) + (l_s \times f_{c1} \times t \times sin\theta \times 10^{-3})$
$\boldsymbol{F_{yv}}$	$(A_{tv}f_{yv} \times 10^{-3})$	$(A_{tv}f_{yv} \times 10^{-3}) + (l_s \times f_{c1} \times t \times cos\theta \times 10^{-3})$
$\boldsymbol{\zeta}$	$\zeta = min\left(\frac{5.8}{\sqrt{f_c'}}, 0.9\right) \times \frac{1}{\sqrt{1+400\varepsilon_r}}$	$\zeta = (1+0.07S_f) \times min\left(\frac{5.8}{\sqrt{f_c'}}, 0.9\right) \times \frac{1}{\sqrt{1+400\varepsilon_{r(SFRC)}}}$
$\boldsymbol{\varepsilon_h}$	0.002	0.003
$\boldsymbol{\varepsilon_v}$	0.002	-0.003 (for isolated strut panels), 0.003 (for Deep Beams and, Beam-column Joints, more details are in section 6.3)
$\boldsymbol{\varepsilon_d}$	-0.001	-0.003
$\boldsymbol{\varepsilon_r}$	0.005	$\varepsilon_{r(SFRC)} = \frac{\varepsilon_h + \varepsilon_v - \varepsilon_d}{(0.1S_f)+1}$
$\boldsymbol{\theta}$	$tan^{-1}\left(\frac{l_v}{l_h}\right)$	Based on Table 4-5

doi:10.6342/NTU202403952

Chapter 5 Comparison of Shear Strength Prediction Models for SFRC Deep Beams and Beam-Column Joints

5.1 Deep Beams

In this section, the shear strength prediction models for SFRC deep beams are compared with the modified SST. The shear prediction models from Narayanan & Darwish [13], Ashour et al. [53], and Khuntia et al. [70], mentioned in section 2.8.1, consider the effects of longitudinal and transverse reinforcement, fiber addition, concrete compressive strength, and shear-span to effective depth ratio. These factors are also involved in the modified SST.

In addition to the shear strength prediction equations from section 2.8.1, the shear analysis procedure based on SMM-UHPC by Shahin et al. [68] as detailed in the literature, is reviewed for the parametric study. A beam cross section of 500 x 180 mm with concrete compressive strength of 70 MPa is considered. Various parameters, such as fiber volume fraction, *a/h* ratio, and horizontal (longitudinal) reinforcement ratio, were varied for each case while keeping the other parameters constant. The equivalent bond strength of the fiber is kept constant at 8 MPa.

doi:10.6342/NTU202403952

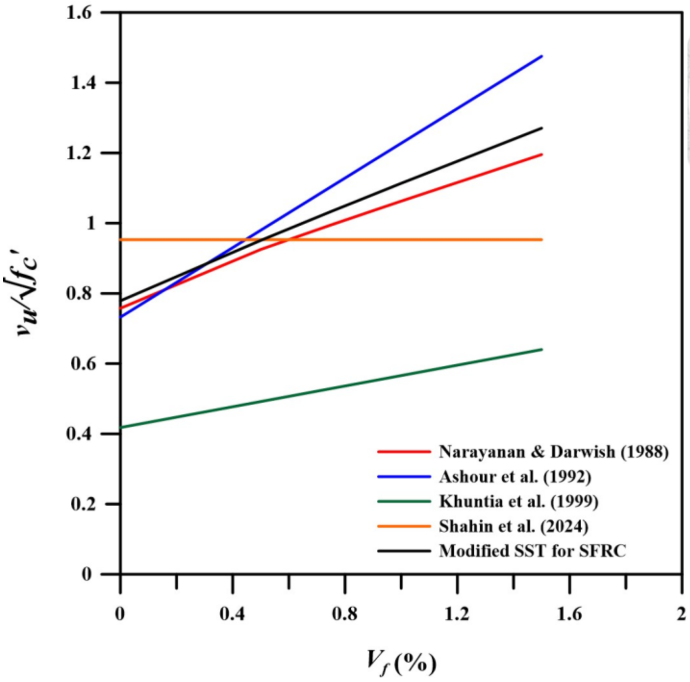

Figure 5-1 Effect of fiber content on calculated shear strength

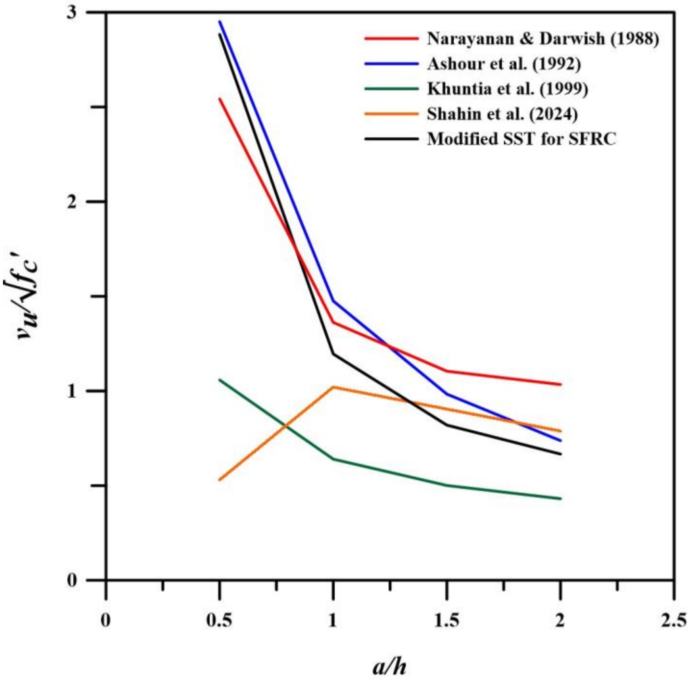

Figure 5-2 Effect of shear span to effective depth ratio

doi:10.6342/NTU202403952

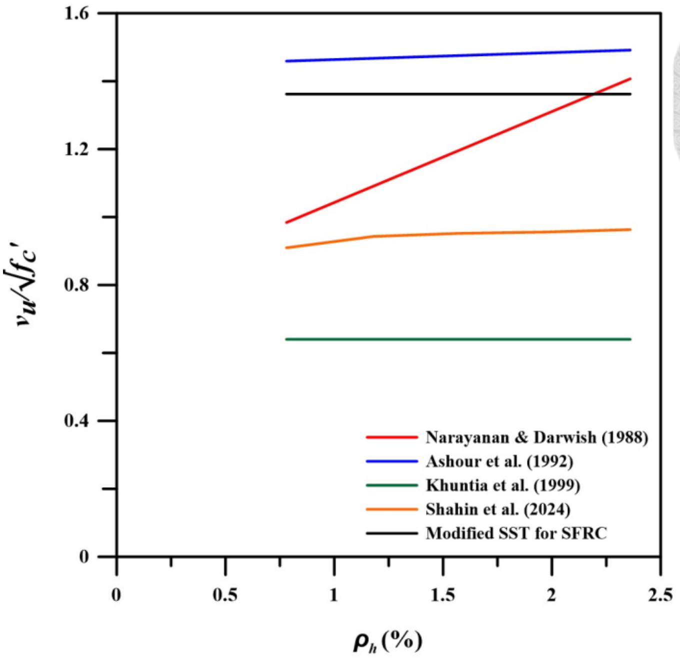

Figure 5-3 Effect of longitudinal reinforcement ratio

In Figure 5-1, only the volume fraction of steel fibers was changed, keeping the other parameters constant, such as with a longitudinal reinforcement ratio ρ_h=1.57% and *a/h* ratio = 1. An increase in fiber content indicated increased shear strength. The model from Khuntia [70] is designed for design purposes and thus predicts the strength of the beam conservatively. As SMM-UHPC [68] is developed based on test data for 1% fibers in the panel test, therefore it gives a straight line for all fiber volume fractions.

In Figure 5-2, only the *a/h* ratio was varied, keeping other parameters constant such as V_f= 1.5% and longitudinal reinforcement ratio ρ_h=1.57%. The *a/h* ratio strongly affects the calculated results. All the equations overestimated shear strength when the *a/h* ratio was less than 1.0, indicating that shear strength is inversely proportional to the *a/h* ratio. However, compared to the predictions of other equations, the proposed SST predictions are more consistent, as observed in the graph.

In Figure 5-3, only the horizontal (longitudinal) reinforcement ratio was varied, keeping other parameters constant such as V_f = 1.5% and *a/h* ratio = 1. The proposed SST is insensitive to the reinforcement ratio. This can be attributed to the condition where the tie index is governed by $K_h \leq \overline{K_h}$. For SMM-UHPC, the prediction is not linear because SMM-UHPC is a trial and error process, requiring a new set of input parameters each time to fulfill the conditions. However, the trend for SMM-UHPC is fairly inclined with the increased longitudinal reinforcement ratio. In the case of Ashour (1992) [53], the equation remains insensitive to the longitudinal reinforcement ratio, which is consistent with their findings where the reinforcement ratio increased from 0.374% to 4.58% with no significant increase in shear strength.

5.2 Beam-Column Joints

The shear strength prediction equation by Jiuru et al. [71] which considers the resistance from concrete, transverse reinforcement and steel fibers is considered for the comparison. Similar to deep beams, the SMM-UHPC is also considered for the evaluation of beam-column joint. A parametric case study for a column cross section of 600 x 600 mm, axial load of $0.1A_g f_c'$, with horizontal (l_h) and vertical (l_v) lever arms. Concrete compressive strength of 70 MPa is considered, and parameters such as fiber volume fraction, l_v/l_h ratio, and longitudinal reinforcement ratio were varied while keeping the other parameters constant. The properties of the fiber, such as equivalent bond strength, are kept constant at 8 MPa.

doi:10.6342/NTU202403952

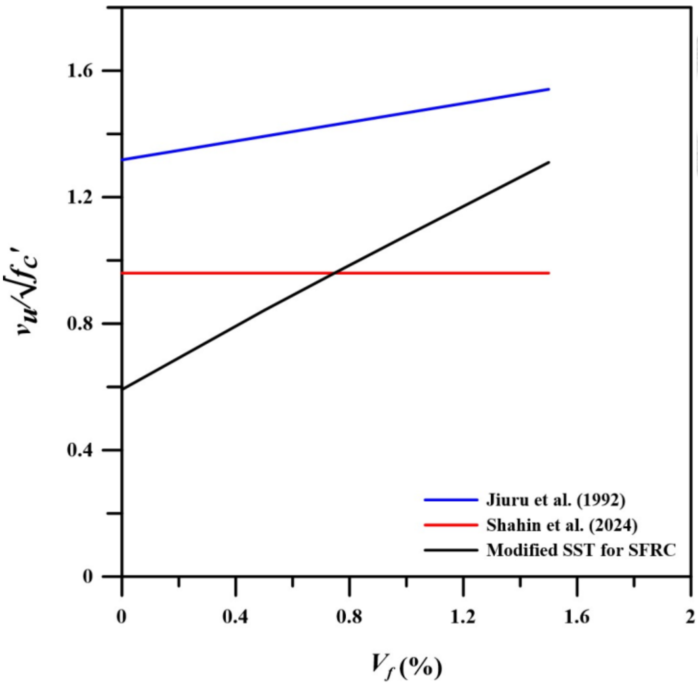

Figure 5-4 Effect of fiber content on calculated shear strength

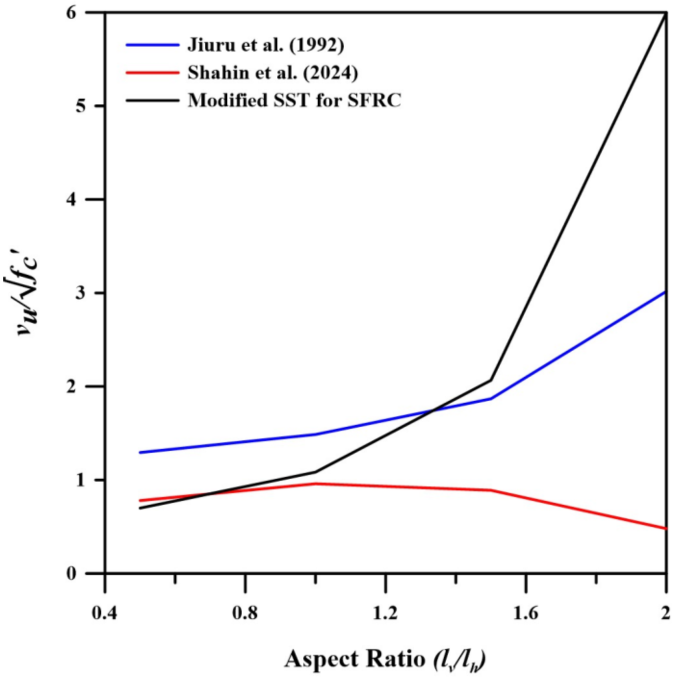

Figure 5-5 Effect of aspect ratio $\left(\frac{l_v}{l_h}\right)$

An increase in fiber content has been observed to enhance shear strength (Figure 5-4). However, the model proposed by Jiuru et al. [71] tends to overestimate this effect. In contrast, the SMM model shows no significant impact from the addition of fibers.

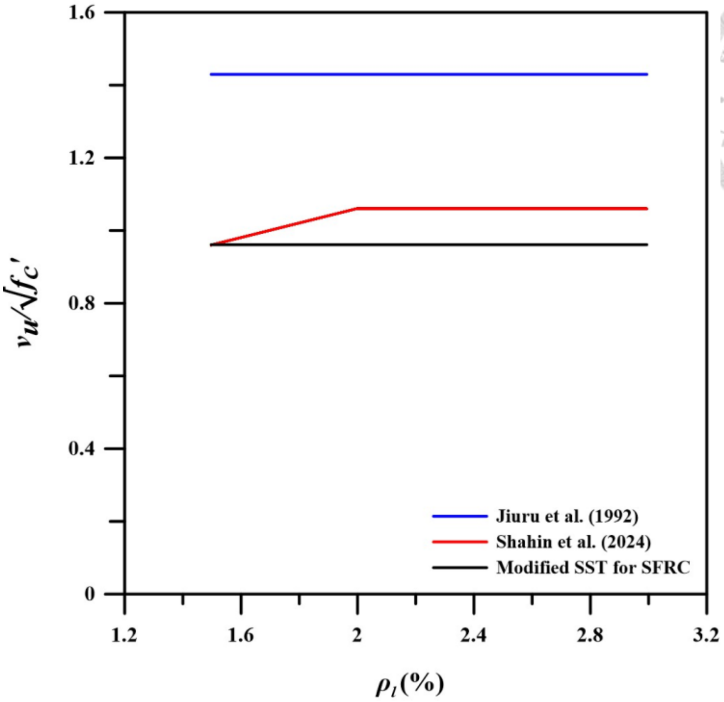

Figure 5-6 Effect of longitudinal reinforcement ratio

In the case of deep beams, when the *a/h* ratio is 0.5, the predictive models will calculate higher shear strength as indicated in Figure 5-2. However, for beam-column joints, after varying the vertical lever arm (l_v), the predictive models will calculate higher strength when the l_v/l_h ratio is 2 (Figure 5-5). This is because, in the case of deep beams, they span along the horizontal axis, while beam-column joints span along the vertical axis.

As indicated in Figure 5-6 The Modified SST for SFRC and the equation provided by Jiuru et al. [71] are insensitive to the longitudinal reinforcement ratio. Similar to deep beams, the effect of the condition $K_h \leq \overline{K_h}$ is also observed in beam-column joints for the modified SST for SFRC. The line drawn for SMM-UHPC is not straight because SMM is an iterative process. For each set of assumed input values, the prediction varies slightly, without large changes. Therefore, it is clear that shear strength prediction is sensitive to the longitudinal reinforcement ratio.

5.3 Summary

A parametric study is provided for deep-beams, comparing different shear strength prediction equations and their sensitivity to various parameters such as fiber volume fraction, *a/h* ratio, and longitudinal reinforcement ratio. Fiber volume fraction and concrete compressive strength show correlations with shear strength. The *a/h* ratio has an inverse relationship with shear strength, with lower ratios (deep beams) exhibiting higher shear strengths. The influence of fiber reinforcement appears to be more consistent than that of traditional web reinforcement.

A parametric study is also conducted for beam-column joint to evaluate the effects of fiber volume fraction, l_v/l_h ratio, and longitudinal reinforcement ratio on joint shear strength. The results show that increasing fiber content enhances shear strength, but the effect may be overestimated by some existing models. The aspect ratio influences shear strength differently in deep beams (*a/h*) versus beam-column joints (l_v/l_h) due to their orientation differences. The proposed SST model and existing models are found to be relatively insensitive to the longitudinal reinforcement ratio.

doi:10.6342/NTU202403952

Chapter 6 Application of Softened Strut-and-Tie model for SFRC Deep Beams and Beam-Column Joints

6.1 Deep Beams

6.1.1 Deep Beam Test Specimens

This study investigates the shear behavior of high-strength steel fiber reinforced concrete (SFRC) deep beams. The experimental program carried out by Chi (2014) [89] and Chen (2018) [90] that includes 3 RC control specimens and 6 SFRC deep beam specimens failed in diagonal splitting or strut failure were adopted in this study. The details of these specimens are given in Table 6-1, and more details are available in Appendix C. The deep beams from “S” series contains a single layer of reinforcement, while, the reinforcement from “D” series contained double layer of reinforcement. Specimens from these series also varied in their width 160mm for specimens from “S” series and 160mm for “D” series. The second term in the nomenclature, “S” represents steel fibers and 000, 075, and 150 represents the 0%. 0.75% and 1.5% fiber volume fraction. Dramix RC-80/30-BP fibers with 0.38mm diameter and aspect ratio of 79 were used. As indicated in Chapter 4, the similar properties of cement, ground granulated blast furnace slag, silica fumes fine aggregate, coarse aggregate, and superplasticizer were used. Cylindrical concrete specimens of dimensions 10cm×20cm were cast on the same of casting the deep beam specimen; and tested for its compressive strength on the day of testing.

Table 6-1 Details of the deep beam specimens

Specimen ID	**Arrangement of the reinforcement**	**Failure Type**	**Beam Cross-section**
S32-S000-HU	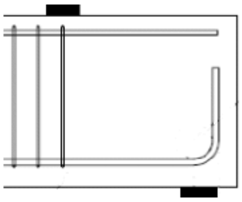	Splitting Failure	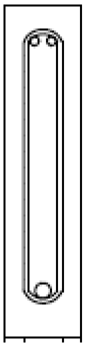
S32-S000-H100	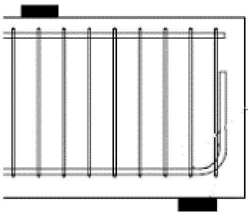	Strut Failure	
S32-S000-TU	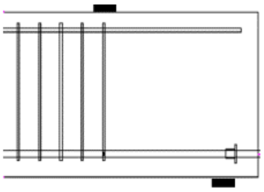	Strut Failure	
D32-S075-TU	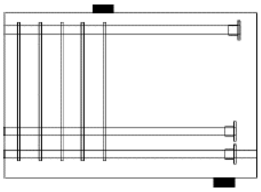	Strut Failure	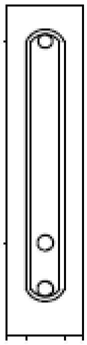
D32-S150-TU			
D32-S075-T300	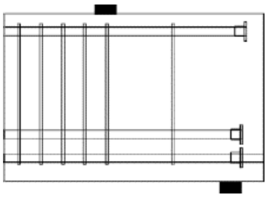	Strut Failure	
D32-S150-T300			
D32-S075-T150	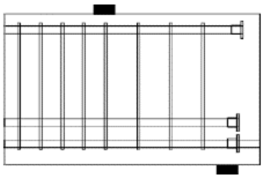	Strut Failure	
D32-S150-T150			

The experimental setup uses a 500 ton compression testing machine for three-point asymmetric tests. Internal measurement systems include strain gauges on the longitudinal (horizontal) and transverse (vertical) reinforcements, while external measurements use dial gauges for deflection measurement; and to get the more precise deformation, NDI markers were fixed on the surface. Pictures were taken at every stage of loading for crack detection.

Table 6-2 indicates the arrangement of strain gauge and NDI markers on the surface. For double layer reinforcement, the strain gauge were attached on the bottom most longitudinal bar.

Table 6-2 Arrangement of strain measuring system

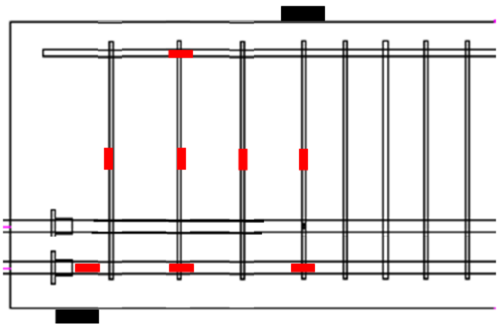	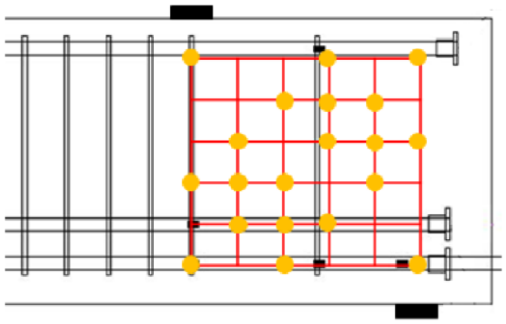
(a) Arrangement of Strain Gauge	(b) Arrangement of NDI markers

6.1.2 Test Results and discussion

The results for material test i.e. the values of concrete compressive strength f_c', yield strength of steel f_y, and ultimate strength V_u are indicated in Appendix C. from the preliminary observations it can be clearly found that, ultimate strength not only increased by increase of stirrup ratio but also increase with fiber volume fraction.

This experimentation by Chen (2018) [90] aims to understand the effects of steel fibers on the structural performance of deep beams, particularly in terms of ultimate strength, failure modes, and crack patterns when compared with the control specimens from Chi (2014) [89]. One of the most significant findings of the study was the substantial increase in ultimate strength observed in specimens containing steel fibers. For instance, the S32-S075-TU specimen, which incorporated 0.75% steel fibers by volume, demonstrated a remarkable more than 50% increase in ultimate strength compared to the S32-S000-HU specimen without fibers.

Table 6-3 Failure pattern in RC specimens [89]

<table>
<tr><td>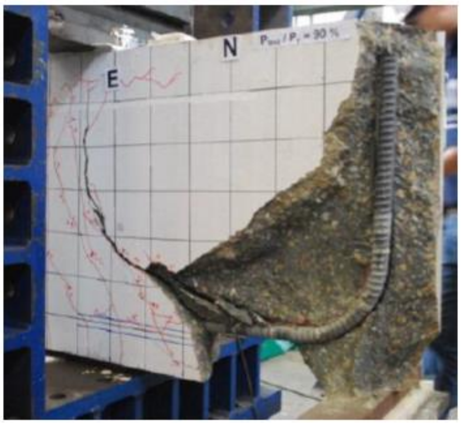 </td><td> </td></tr>
<tr><td>(a) S32-S000-HU</td><td>(b) S32-S000-H100</td></tr>
<tr><td colspan="2">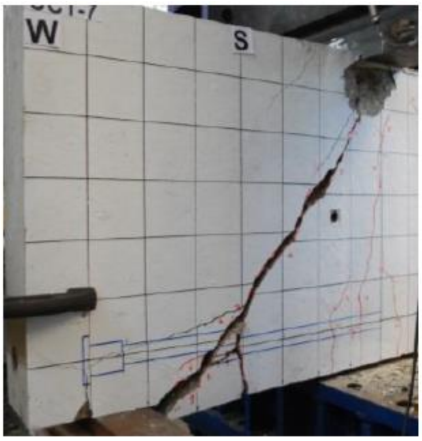 </td></tr>
<tr><td colspan="2">(c) S32-S000-TU</td></tr>
</table>

The failure modes of the specimens varied significantly based on their reinforcement configuration and the presence of steel fibers. Non-fiber reinforced concrete specimens, such as S32-S000-TU, exhibited strut failure. The D32-S075 series and D32-S150 (including TU, T300, and T150 variants) all experienced strut failure. The results also indicated significant improvements in ductility and post-peak behavior for specimens containing steel fibers.

Crack patterns observed in the specimens indicates the internal stress distribution and the effect of steel fibers. The crack pattern for the RC and SFRC specimens adopted in this study at the ultimate load is given in Table 6-3 and 6-4. Specimens reinforced with steel fibers typically developed multiple fine cracks parallel to the main diagonal crack. This crack pattern indicates a more distributed stress field and better crack control compared to non-fiber specimens, which usually exhibited a single prominent diagonal crack. The improved crack controlling characteristics in fiber-reinforced specimens suggests enhanced stress distribution capabilities, contributing to their increased ultimate strength. After reaching ultimate load, fiber-reinforced specimens demonstrated more gradual strength degradation compared to their RC deep beam specimens.

Strain measurements provided crucial data for understanding the internal behavior of the specimens. In most cases, the main tensile reinforcement did not reach yield strain at ultimate load, indicating that the specimens' capacities were not limited by reinforcement yielding. However, exceptions were noted, such as in the D32-S150-T150 specimen, where the main reinforcement reached a strain of 0.0046, exceeding the yield point. However this specimen is still considered for analysis, since it clearly indicates the failure of the strut at the node.

Based on deformation data from strain gauges and NDI markers, Chen (2018) [90] proposed a principal tensile strain value ε_r of 0.008 for SFRC. This value is further modified in this research in the subsequent sections based on isolated panel test results.

doi:10.6342/NTU202403952

Table 6-4 Failure pattern in SFRC specimens [90]

	
(a) D32-S075-TU	(b) D32-S075-T300
	
(c) D32-S075-T150	(d) D32-S150-TU
	
(e) D32-S150-T300	(f) D32-S150-T150

6.2 Force transfer Mechanism in Deep Beams

Strut-and-tie modeling is a popular method for analyzing deep beams, having been included in design codes since 1984 [91,92] as indicated in Figure 6-1. This approach involves three main shear resistance mechanisms: a diagonal strut connecting between the load and support, a truss mechanism with vertical web reinforcement, and a truss mechanism with horizontal web reinforcement. These struts and ties connect at nodal zones near the load and support points.

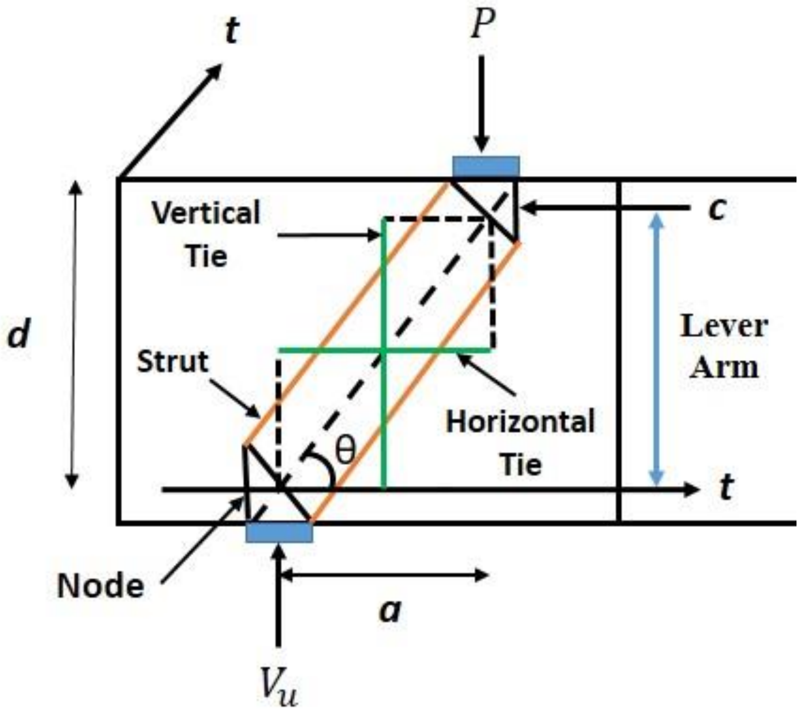

Figure 6-1 FTM in Deep Beams with strut-and-tie model

Hwang et al. (2000) [17] suggested that the shear carried by each mechanism depends on the angle of the diagonal strut. Before the web reinforcement yields, the vertical web reinforcement's shear contribution decreases as the angle increases, while the horizontal web reinforcement's contribution increases. The diagonal strut's contribution increases up to a 45-degree angle and decreases for larger angles. After the

doi:10.6342/NTU202403952

web reinforcement yields, the diagonal strut carries all additional shear until the beam fails, which is thought to happen due to concrete crushing near the nodal zones.

6.2.1 Force transfer mechanism in SFRC deep beams

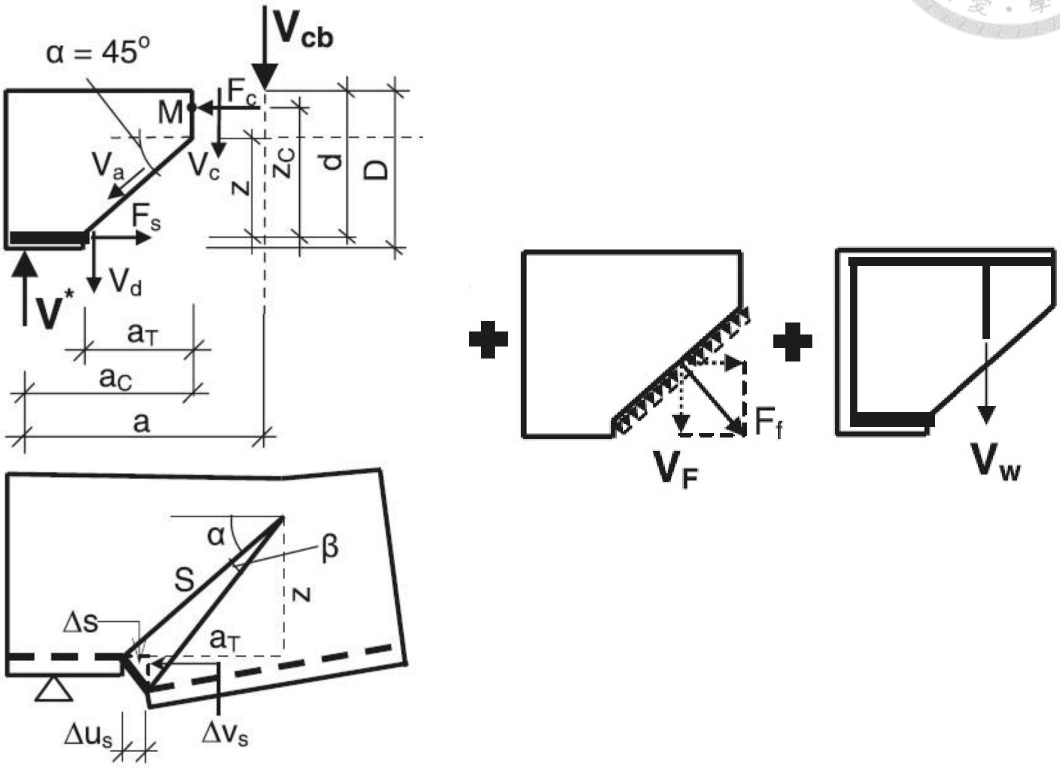

Figure 6-2 Shear cracking in simply supported SFRC beam with geometric assumptions [93]

The equilibrium of internal stresses, compatibility conditions, and material constitutive laws determine the basis for this analysis. The shear capacity of a SFRC beam V_u can be calculated from the formula proposed by Vandewalle et al. (2000) [94]

$$V_u = V_{cb} + V_F + V_w \qquad (6\text{-}1)$$

Here, in Figure 6-2, V_{cb} represents the shear resistance of the beam in the absence of transverse reinforcement. The mechanism includes the shear force across the compression zone V_c, the force due to aggregate interlocking V_a, and the dowel action force V_d. The contribution of fibers is denoted by V_f, while the contribution of shear reinforcement, namely stirrups, is represented by the force V_w.

6.3 Derivation of Principal Tensile Strain(ε_r)Values for SFRC Deep Beams and Beam-Column Joints

Previous studies on the softened strut-and-tie model conducted by Hwang & Lee (1999) [16] and Hwang & Lee (2002) [64] on reinforced concrete elements recommended the use of a principal tensile strain value $\varepsilon_r = 0.005$. This value was derived from the strain conditions of horizontal and vertical reinforcement along with the strain condition of concrete at the ultimate load stage. Therefore, considering normal strength concrete and normal strength reinforcement, these values are $\varepsilon_h = 0.002, \varepsilon_v = 0.002,$ and $\varepsilon_d = -0.001$. By using the equation $\varepsilon_r + \varepsilon_d = \varepsilon_h + \varepsilon_v$, the value of ε_r was calculated as 0.005. However, this value does not simulate the effect of high strength reinforcement, and the effect of steel fiber addition.

According to the values derived for ε_d, ε_h, and ε_v from the isolated panel test results for SFRC material (Chapter 4), which are respectively -0.003, 0.003, and -0.003, they are used in this chapter with a minor modification for the value of ε_v. The value of ε_v derived from isolated panel test results reflects the behavior of vertical reinforcement in compression and is represented by the negative (-ve) sign. However, in the case of shear elements such as deep beams and beam-column joints, the strain in the vertical/shear reinforcement is positive. Therefore, the value of $\varepsilon_v = 0.003$ is considered for further calculations. Moreover, in case of the absence of the steel fibers, the value of ε_d will be reduced to -0.001.

This value of ε_v can be further justified by the value $\varepsilon_h = 0.003$ due to the fact that reinforcement is an isotropic material. Consequently, the value of ε_r used for the calculation of shear strength of D-Region SFRC elements is 0.009.

6.4 α and λ coefficients for 2D and 3D Conditions

Based on the experimental and analytical studies of Liao et al. and Naaman [11,95], the following values for the coefficients α and λ are provided

6.4.1 Coefficient α

$$\alpha = \alpha_1 \alpha_2 \alpha_3 \tag{6-2}$$

The coefficient α_1 represents the average contribution of bonding at the beginning of matrix cracking. For most commonly used cement composites, its value ranges from 1% to 15%. For initial design purposes, a value of $\alpha_1 = 10\%$ is considered reasonable.

The efficiency factor α_2 for fiber orientation in the uncracked state of the composite varies as: it equals 1 for unidirectional fibers (1D case), $2/\pi$ for fibers randomly oriented in planes (2D case), and $1/2$ for fibers randomly oriented in space (3D case). This factor determines the number of fibers intersecting a unit area of the composite, whether it is cracked or uncracked composite.

α_3 coefficient indicates the decrease in bond strength at the fiber-matrix interface due to applied external stress, either radial or normal to the interface. For aligned fibers, this coefficient equals 1.

Since panels are membrane elements (2D) where the length is much greater than the thickness, whereas beams are 3D elements, the coefficient $\alpha = 0.1 \times \left(\frac{1}{2}\right) \times 1 = 0.05$ is considered for deep beams, assuming the fibers are randomly oriented in 3D space.

doi:10.6342/NTU202403952

6.4.2 Coefficient λ

$$\lambda = \lambda_1 \lambda_2 \lambda_3 \lambda_4 \tag{6-3}$$

The coefficient λ_1 is defined as follows:

$$\lambda_1 = \frac{fiber\ embedded\ distance(shorter\ distance\ from\ the\ crack)}{length\ of\ the\ fiber} \tag{6-4}$$

This value is derived as $1/4$ from probability theory considerations.

λ_2 Coefficient considers orientation effect on pull out resistance and is a product of λ_4 and α_2. According to Liao et al. [87] the value of coefficient λ_3 (group reduction coefficient) is taken as 1, which represents the decrease in the bond strength when number of fiber pulled out of the matrix increases from the same area. Moreover, the value of λ_4 is also taken as 1, this value represents the ratio of maximum pull out load for a fibre oriented at angle θ to maximum pull-out load for a fibre aligned with the pull out direction and its value for unidirectional fibers is 1. Consequently, for the case of deep beams the value of $\lambda = 0.25 \times (4 \times 1/2) \times 1 \times 1 = 0.5$.

6.5 Depth of compression zone in Deep Beams

For deep beams within the SST analysis, the key factors influencing the strength are the angle (θ) of the inclined diagonal compressive strut and the effective area A_{str} at the node where the strut interface the node. Figure 6-3 illustrates the method for determining both theta (θ) and A_{str}. A study by Hwang et al. [63] showed that the depth of the compression zone at the interface of the node and the strut is closely related to the effective area A_{str}. Therefore, the depth of the compression zone (kd), in deep beams is suggested to be determined using the following Eq. (6-5) to (6-7).

doi:10.6342/NTU202403952

$$\tan\theta = \frac{d - kd/3}{l_h} \tag{6-5}$$

$$A_{str} = b \times \sqrt{(kd)^2 + \left(\frac{a_p}{2}\right)^2} \tag{6-6}$$

$$kd = \left(\sqrt{\left(\rho_f n\right)^2 + 2\rho_f n} - \rho_f n\right) \times d \tag{6-7}$$

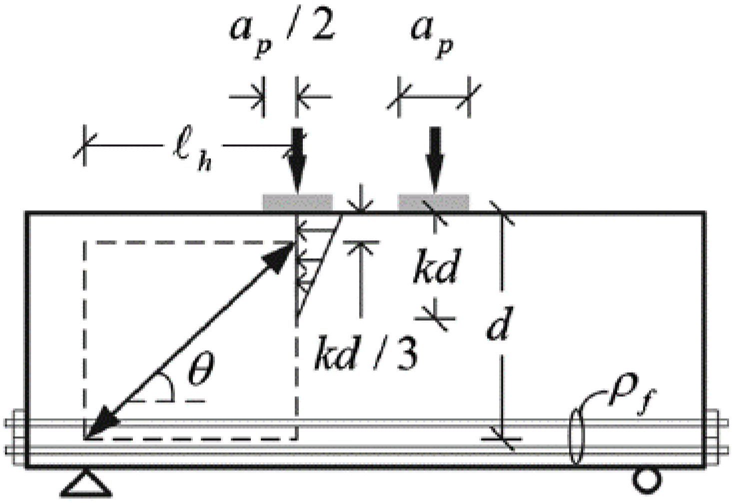

Figure 6-3 Illustration for Deep Beams [63]

Here, ρ_f stands for the flexural tensile reinforcement ratio in the beam; n represents the ratio of the modulus of elasticity of the reinforcement to that of concrete; and *d* is the effective depth of the beam. It's noted that compression reinforcement in a beam will decrease the depth of the compression zone, resulting in lower shear strength as per the softened strut-and-tie model. This outcome is contradictory. Therefore, Hwang et al. [63] suggest the use of Eq. (6-7) regardless of whether the beam or corbel includes compression reinforcement.

6.6 Application of proposed SST to SFRC deep beams available in the literature

A total of 26 SFRC deep beams and 16 companion RC deep beams were used in this evaluation of the SST analysis procedure. These beams had the following properties:

1. Since the applicable range of SST is when a/d < 2.5, deep beams with a shear span-to-depth ratio of a/d < 2.5 were adopted in this study.

2. Beam depth h between 200 mm and 700 mm.

3. Horizontal web reinforcement $\rho_h f_{yh}$ between 1.5 MPa and 15 MPa.

4. Concrete cylinder strength (f_c') between 20 MPa and 90 MPa.

5. Hooked steel fibers (5 deep beams with a combination of straight and hooked-end fibers) in volume fractions (V_f) ranging between 0.5% and 1.5%.

6. Fiber tensile strength (f_u) between 1100 MPa and 2300 MPa.

7. Fiber aspect ratio l_f/d_f between 50 and 79.

8. The test specimens were reported to have failed due to shear, diagonal splitting, and strut failure, not due to shear-flexure or flexure.

9. The test specimens were simply supported. Loads and reactions were applied using bearing blocks of specified depth.

doi:10.6342/NTU202403952

6.7 Sample calculation for SFRC Deep Beam based on Modified SST for SFRC

Given Parameters	**Specimen ID: D32-S075-T150** $\boldsymbol{V_u = 874.7\ kN}$ **Transverse Reinforcement at 150mm C/C** 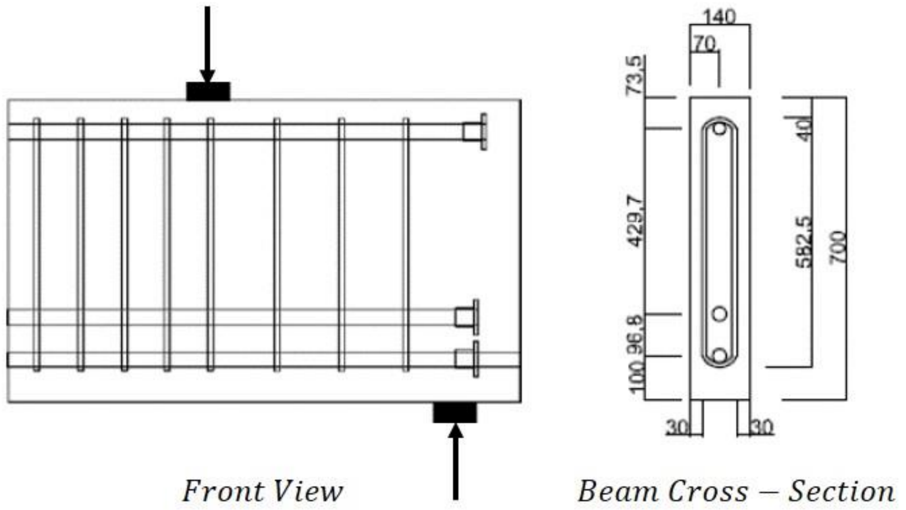
	Dimensions of Beam c/s = $160 \times 700mm$ Number of bars in horizontal Direction (Tension) = 2 nos. Number of bars in horizontal Direction (Compression) = 1 nos. Number of bars in vertical Direction (Transverse reinforcement) = 6 nos. Area of Horizontal Bar (Tension) = $819mm^2$ Area of Horizontal Bar (Compression) = $645mm^2$ Area of Vertical Bar (Transverse reinforcement) = $71mm^2$ $f_y = 600\ MPa$ $f_c' = 79.30MPa$ $V_f = 0.0075$ (Fraction) $l_f = 30mm$ $d_f = 0.38mm$ $\alpha = 0.05$ $\lambda = 0.5$ $\tau_{eq} = 8MPa$ $a_p = 50mm$ (Half the width of the plate i.e. 100/2 = 50mm)

doi:10.6342/NTU202403952

Solution

Step 1: **Calculation of θ and A_{str} for loading plate $100 \times 160mm$**

$$kd = \left(\sqrt{\left(\rho_f n\right)^2 + 2\rho_f n} - \rho_f n\right) \times d$$

$$\therefore kd = \left(\sqrt{(0.0185 \times 4.778)^2 + (2 \times 0.0185 \times 4.778)} - 0.0185 \times 4.778\right) \times 551.6 = 188.25\ mm$$

$$A_{str} = b \times \sqrt{(kd)^2 + \left(a_p\right)^2}$$

$$= 160 \times \sqrt{(188.25\ )^2 + (50)^2} = 31163.69\ mm^2$$

$$\theta = \tan^{-1}\left(\frac{l_v}{l_h}\right) = \tan^{-1}\left(\frac{488.85}{700}\right) = 34.92°$$

Step 2: **Properties of SFRC**

$$\varepsilon_r = \frac{\varepsilon_h + \varepsilon_v - \varepsilon_d}{\left(0.1S_f\right) + 1} = \frac{0.009}{\left(0.1 \times 8 \times 0.0075 \times \frac{30}{0.38}\right) + 1} = 0.0061$$

$$\sigma_{cc} = \sigma_{mu}\left(1 - V_f\right) + \alpha\tau_{eq}V_f\left(\frac{l_f}{d_f}\right)$$

$$\therefore \sigma_{cc} = [4.98(1 - 0.0075)] + \left[0.05 \times 8 \times 0.0075 \times \frac{30}{0.38}\right]$$

$$= 5.186MPa$$

$$\sigma_{pc} = \lambda\tau_{eq}V_f\left(\frac{l_f}{d_f}\right)$$

$$\therefore \sigma_{pc} = 0.5 \times 8 \times 0.0075 \times \frac{30}{0.38} = 2.368MPa$$

$$f_{c1} = \sigma_{cc} + \frac{\sigma_{pc} - \sigma_{cc}}{0.007 - \epsilon_{cc}} \times (\epsilon_{\mathrm{r}} - \epsilon_{cc})$$

$$\therefore f_{c1} = 5.186 + \frac{2.368 - 5.186}{0.007 - 0.00015} \times (0.0061 - 0.00015)$$

$$= 2.738MPa$$

doi:10.6342/NTU202403952

Step 3: **Yielding forces of the ties**

$$F_{yh} = (A_{th}f_{yh} \times 10^{-3}) + (l_s \times f_{c1} \ \times t \times sin\theta \times 10^{-3})$$

$$\therefore F_{yh} = (2 \times 819 \times 600 \times 10^{-3}) \ + (1 \times 645 \times 600 \times 10^{-3})$$

$$+ (853.79 \times 2.738 \ \times 160 \times sin34.92° \times 10^{-3})$$

$$= 1583.79kN$$

$$F_{yv} = \ (A_{tv}f_{yv} \times 10^{-3}) \ + (l_s \times f_{c1} \times t \times cos\theta \times 10^{-3})$$

$$\therefore F_{yv} = (6 \times 71 \times 600 \times 10^{-3})$$

$$+ (853.79 \times 2.738 \times 160 \times cos34.92° \times 10^{-3})$$

$$= 562.029kN$$

Step 4: **Force distribution**

$$\gamma_h = \frac{2 \ \tan\theta - 1}{3} = \frac{2 \ \tan 34.92° - 1}{3} = 0.132$$

$$\gamma_v = \frac{2 \ \cot\theta - 1}{3} = \frac{2 \ \cot 34.92° - 1}{3} = 0.621$$

Step 5: **Balanced amounts of tie forces**

$$\overline{K_h} = \frac{1}{1 - 0.2(\gamma_h + \gamma_h^2)} = \frac{1}{1 - 0.2(0.132 + 0.132^2)} = 1.031$$

$$\overline{K_v} = \frac{1}{1 - 0.2(\gamma_v + \gamma_v^2)} = \frac{1}{1 - 0.2(0.621 + 0.621^2)} = 1.252$$

Step 6: **Softening of concrete**

$$\zeta = \left(1 + 0.07S_f\right) \times min\left(\frac{5.8}{\sqrt{79.3}}, \ 0.9\right) \times \frac{1}{\sqrt{1 + 400 \times 0.0061}} = 0.46$$

Where, $S_f = 0.0075 \times \frac{30}{0.38} \times 8$

$$\overline{F_h} = \gamma_h \times (\overline{K_h}\zeta f_c' A_{str}) \times \cos\theta$$

$$\therefore \overline{F_h} = 0.132 \times 1.031 \times 0.46 \times 79.3 \times 31163.69 \times cos34.92° \times 10^{-3}$$

$$= 126.85kN$$

$$\overline{F_v} = \gamma_v \times (\overline{K_v}\zeta f_c' A_{str}) \times \sin\theta$$

$$\therefore \overline{F_v} = 0.621 \times 1.252 \times 0.46 \times 79.3 \times 31163.69 \times sin34.92° \times 10^{-3}$$

$$= 505.94kN$$

Step 7: **Tie index**

$$K_h = 1 + (\overline{K_h} - 1)\left(F_{yh}/\overline{F_h}\right)$$

$$\therefore K_h = 1 + (1.031 - 1)\left(\frac{1583.79}{126.85}\right) = 1.387 > \overline{K_h}$$

take, $K_h = 1.031$

$$K_v = 1 + (\overline{K_v} - 1)\left(F_{yv}/\overline{F_v}\right)$$

$$\therefore K_v = 1 + (1.252 - 1)\left(\frac{562.029}{505.94}\right) = 1.279 > \overline{K_v}$$

take, $K_v = 1.225$

Step 8: **Compressive strength of the strut**

$$C_{d,n} = (K_h + K_v - 1)\zeta f_c' A_{str}$$

$$\therefore C_{d,n} = (1.031 \ + 1.225 - 1) \times 0.46 \times 79.3 \times 31163.69 \times 10^{-3}$$

$$= 1427.807\text{kN}$$

$$\boldsymbol{V_{ucal} = 1427.81 \times sin34.92° = 817.326}\textbf{kN}$$

Strength Ratio

$$\frac{V_u}{V_{ucal}} = \frac{874.7}{817.326} = 1.07$$

6.8 Effect of fiber volume fraction, a/h ratio, longitudinal and transverse reinforcement ratio, and concrete compressive strength on Modified SST for SFRC

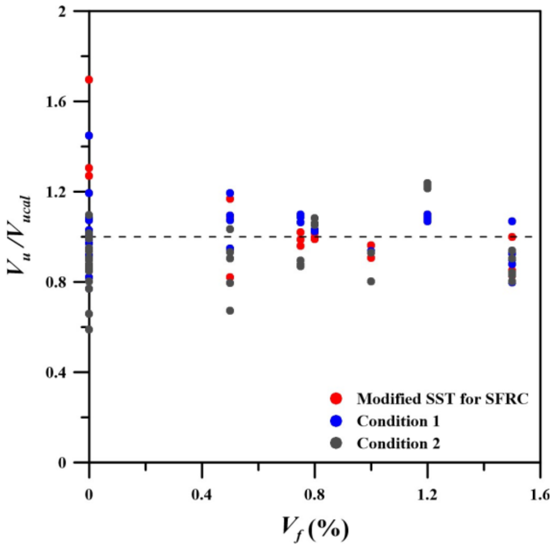

(a) Effect of fiber volume fraction on shear strength prediction

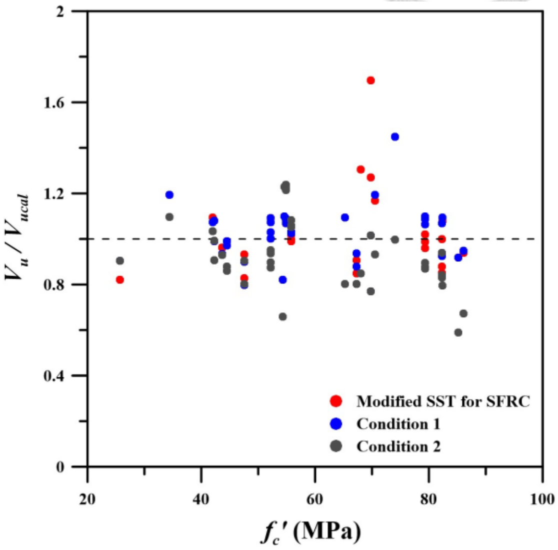

(b) Effect of concrete compressive strength on shear strength prediction

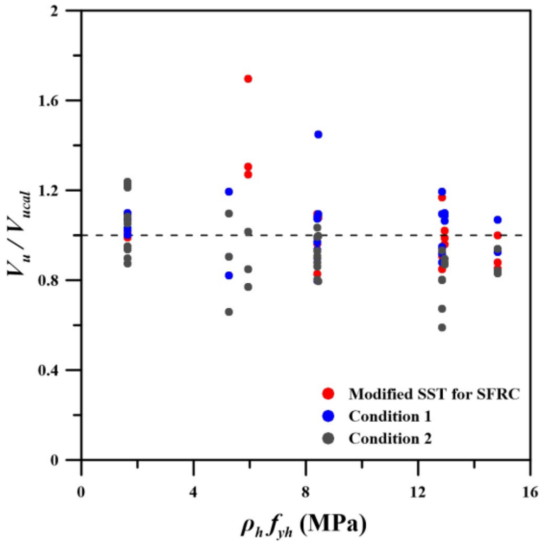

(c) Effect horizontal web reinforcement on shear strength prediction

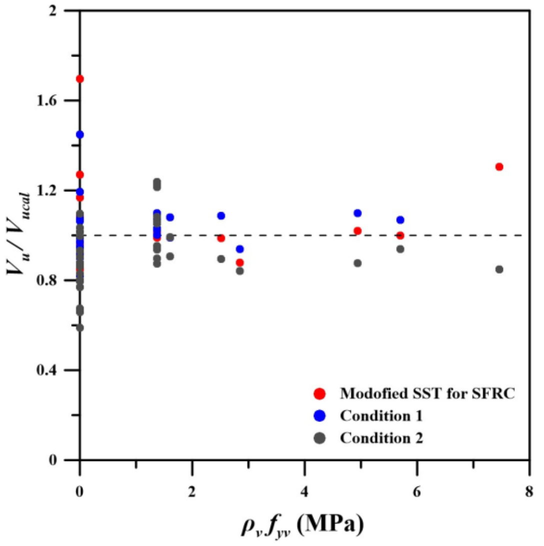

(d) Effect of vertical web reinforcement on shear strength prediction

doi:10.6342/NTU202403952

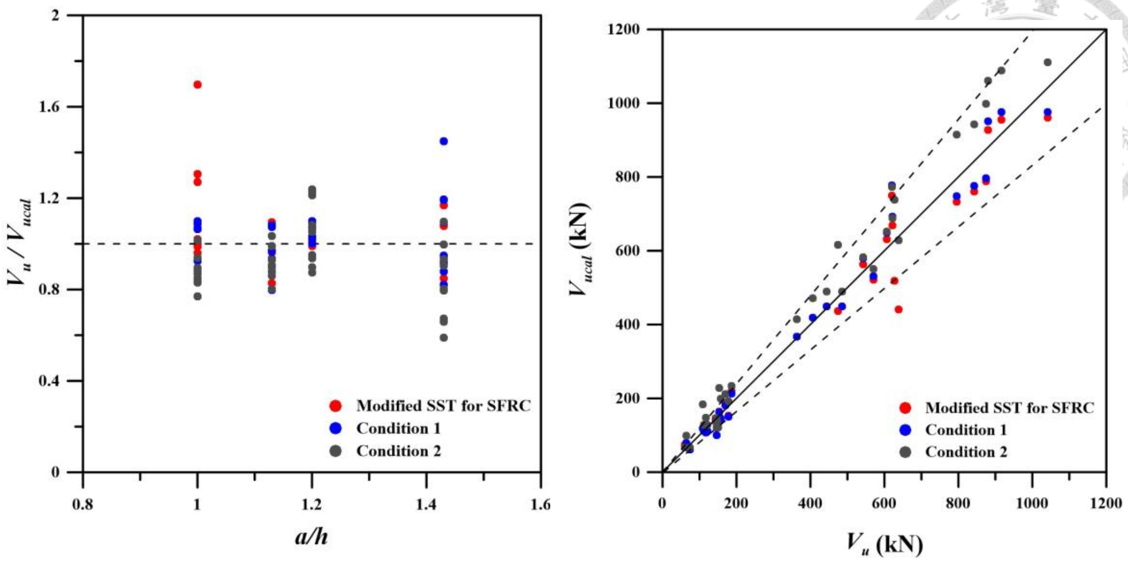

(e) Effect of shear span to depth (*a/h*) ratio on shear strength prediction

(f) Comparison of Modified SST for SFRC with condition 1 & 2 (Table 4-6)

Figure 6-4 Results of deep beams compared with different parameters

Figure 6-4 indicates the effect of different parameters on the sensitivity of the Modified SST for SFRC. The conditions given in Table 4-6 are also considered to check the effect of parameters ζ and τ_{eq} on the calculated shear strength.

Figure 6-4(a) demonstrates the effect of fiber volume fraction on predicted shear strength. As the fiber volume fraction increases, there is a general trend of increasing shear strength for all the conditions. Figure 6-4(b) illustrates the variation in predicted shear strength with concrete compressive strength f_c'. The x-axis represents concrete strength, while the y-axis shows the ratio of experimental to predicted shear strength (V_u/V_{ucal}). There is a slight downward trend, indicating that shear strength is overestimated as concrete strength increases with most data points fall between 0.8 and 1.2, suggesting reasonably accurate predictions for Modified SST for SFRC. However, for Condition 2 this variation is in between 0.7 to 1, indicating overestimation of calculated results. This graph shows a clear positive correlation between concrete compressive strength and shear strength, although the data points are more spread out compared to the fiber volume fraction graph, indicating more variability in predictions as compressive strength changes.

Figure 6-4(c) presents the effect of horizontal web reinforcement ρ_h on shear strength predictions. No clear trend is visible, with data points scattered around $\frac{V_u}{V_{ucal}} = 1$, indicating that the model predicts shear strength reasonably well across different levels of horizontal reinforcement. However, the data points are more scattered, suggesting that horizontal reinforcement might have a less consistent impact on shear strength compared to other factors.

The graph in Figure 6-4(d) shows the influence of vertical web reinforcement ρ_v on shear strength predictions. For low amounts of vertical reinforcement, the Modified SST for SFRC and Condition 2 tends to be slightly conservative ($\frac{V_u}{V_{ucal}} > 1$), with most predictions falling within 20% of the experimental values (0.8 < $\frac{V_u}{V_{ucal}}$ < 1.2). For condition 3, even for the low amount of vertical web reinforcement, the results are overestimated. Figure 6-4(e) depicts the effect of the a/h ratio on shear strength predictions. There is a trend where lower *a/h* ratios correspond to higher shear strengths. The data points are more tightly clustered for lower *a/h* (1<*a/h*<1.2) ratios and become more scattered as the ratio increases (1.2<*a/h*<1.5).

The above discussion indicate that condition 3 where the value of ζ adopted from MCFT is overestimating the shear strength with a mean value of 0.93 ($\frac{V_u}{V_{ucal}} < 1$) as indicated in the Figure 6-4(f). Slight variation between the calculated shear strength by

doi:10.6342/NTU202403952

employing Modified SST for SFRC (Mean: 1.04, and CoV: 12.74) and Condition 2 (Mean: 1.02, and CoV: 11.82) indicated that the τ_{eq} has less influence on the calculated results.

6.9 Verification of the Modified SST for SFRC Deep Beams

For verification, the shear strength prediction equations and analysis procedures by Narayanan and Darwish (1988), Ashour et al. (1992), Khuntia et al. (1999) and SMM-UHPC by Shahin et al. (2024) [13,53,68,70] were applied to the beams listed in Appendix C (Column 1, 2, 3, 4 respectively). These models were chosen in this study due to their applicable range of shear span-to-depth ratios, the use of high-strength concrete, and the inclusion of hooked-end steel fibers.

To evaluate the accuracy of the proposed SST model compared to other shear strength prediction equations, the data provided in Table 6-5 and Figure 6-5 is analyzed. The shear strength of the 42 considered deep beams, shown in Appendix C (Column 5), has been evaluated by means of the analysis procedure discussed in chapter 4. The value of shear strength recorded in the experiments V_u versus the shear strength obtained from the analysis V_{ucal} are plotted in Figure 6-5 for the equations from Narayanan & Darwish [13], Ashour et al. [53] and Khuntia [70]. The mean, standard deviation (SD), and coefficient of variation (COV) values of the experimental shear strengths V_u to the calculated shear strengths V_{ucal} ratios, have been reported in Table 6-5.

The proposed SST model demonstrates superior performance in predicting the shear strength of SFRC deep beams compared to Narayanan & Darwish (1988), Ashour (1992), and Khuntia (1999). Its predictions are more close to the experimental values with low SD and CoV across a wide range of beam properties. While Ashour's model shows good accuracy with a mean of 1.00, its higher standard deviation (0.28) indicates more variability. The Khuntia model, with a mean of 1.93, which could lead to overly

doi:10.6342/NTU202403952

conservative estimations. The Narayanan & Darwish's model, while an improvement over some existing models in terms of CoV, still shows higher variability compared to the Modified SST.

Table 6-5 Results for prediction equations

Author	**Mean**	**Standard Deviation**	**Coefficient of variation**
Narayanan & Darwish (1988)	1.19	0.21	17.24
Ashour (1992)	1.00	0.28	27.86
Khuntia (1999)	1.93	0.51	26.41
Modified SST for SFRC	1.04	0.13	12.74

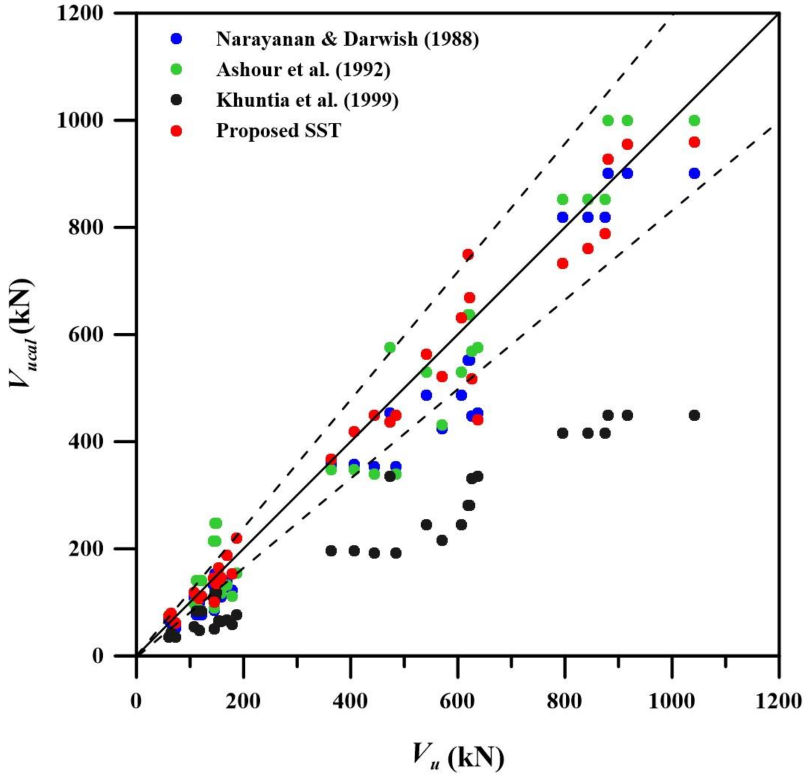

Figure 6-5 Evaluation of Modified SST with existing shear strength prediction models for SFRC

6.10 Summary for Application of Modified SST for SFRC Deep Beam

A consistent SST model for predicting the shear strength of RC and SFRC deep beams is obtained by incorporating the significance of the ε_d value. In this chapter, a new calculated value of principal tensile strain, equal to 0.009 for SFRC, is proposed. A sample calculation based on the Modified SST for SFRC is also provided in this chapter.

In conclusion, calculations based on the modified SST for SFRC are performed and compared with other prediction equations, indicating that the proposed SST model shows significant improvements over existing models for predicting shear strength in SFRC deep beams. Based on the deep beam database presented in Appendix B, this model also demonstrates its applicability across a range of concrete compressive strengths, fiber volume fractions, *a/h* ratios, and reinforcement ratios.

6.11 Beam-Column Joints

6.11.1 Description of Specimen

Laboratory tests on full-scale beam-column joint were carried out by Chang (2017) [96] that includes 2 SFRC beam-column joints out of which one indicated joint failure and is adopted in this study for the analysis. The SFRC joint LAHHV_SF (as Figure 6-6 shows) is subjected to low axial load as $0.1A_g f_c'$ and with 1.5% steel fiber volume fraction in the joint region, and 70 MPa concrete strength.

The specimen was tested using a Multi-Axial Testing System (MATS) with the column ends fixed in hinged supports and cyclic lateral load applied at the column base. Internal strain measurement was done using strain gauges attached to reinforcement, while external measurements included LVDTs, tiltmeters, and π gauges. The loading protocol for the experiment was displacement-controlled, based on drift ratios. As

doi:10.6342/NTU202403952

indicated in Figure 6-7 the loading protocol involved drift ratios from 0.25% to 8% with three cycles at each level. Before lateral loading, a constant axial load ($0.1A_gf_c'$: low axial load) was applied.

6.11.2 Experimental Observations

For specimen LAHHV_SF, the first crack appeared at +0.35% drift in the beam as a flexural crack. Joint shear cracks appeared later at +1.5% drift. As loading progressed, 45° diagonal shear cracks developed in the joint region. Initially, crack widths remained below 1.5mm, with an increasing number of cracks forming.

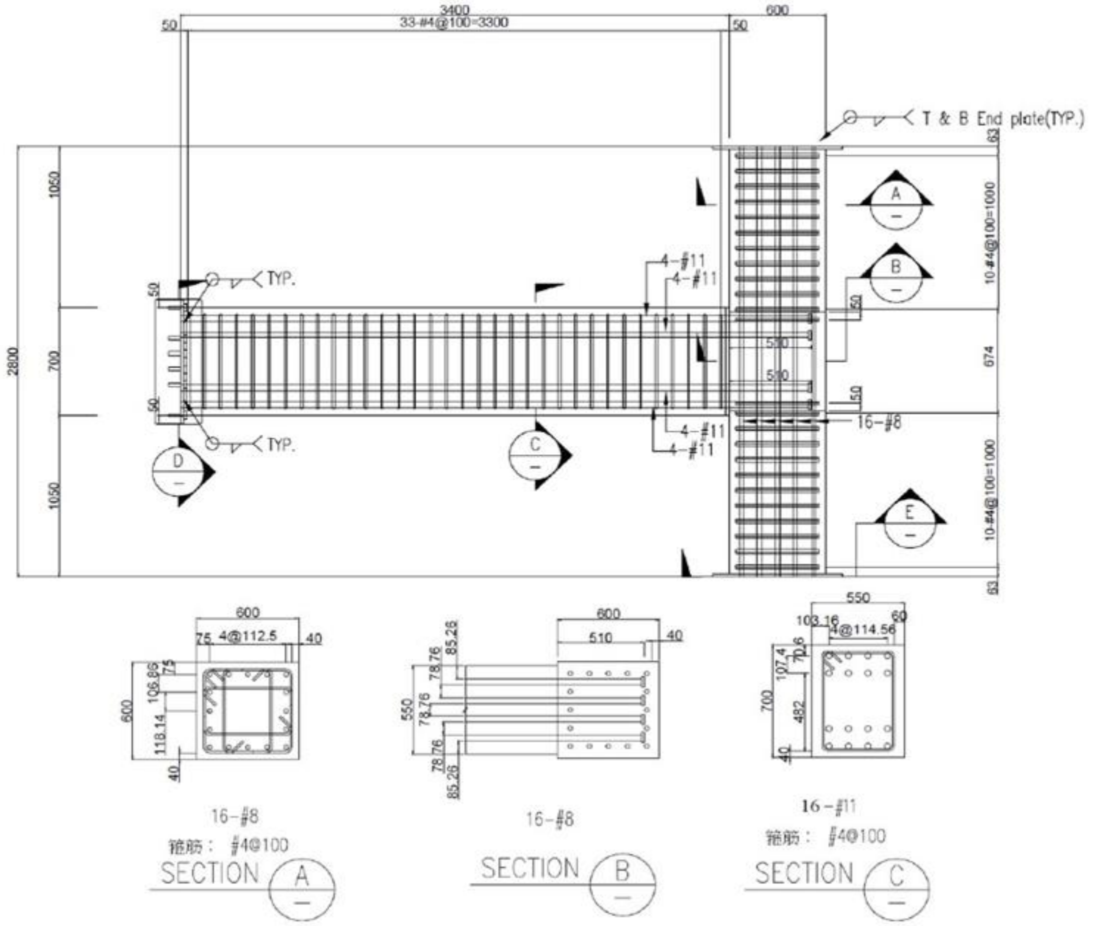

Figure 6-6 Dimensions and reinforcement details of the Beam-Column Joint specimen LAHHV_SF

doi:10.6342/NTU202403952

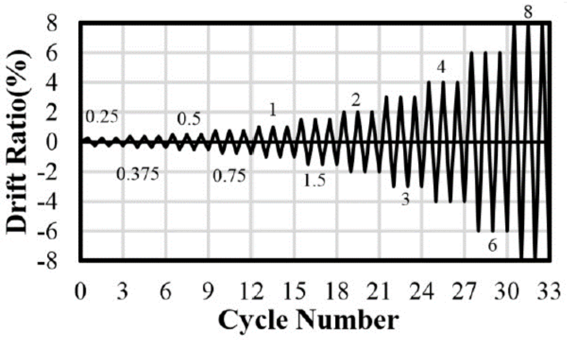

Figure 6-7 Loading protocol

Significant widening of the cracks were observed after +4% drift, with the main wide cracks developing along the diagonal of the joint. The test were termination at +6% drift, and the maximum joint crack width reached 19mm as indicated in Figure 6-8. Notably, beam cracks remained fine throughout the test, with larger cracks only appearing at the beam top and bottom. Despite the extensive cracking, no severe concrete spalling was observed, allowing the specimen to maintain overall integrity.

The strain gauges data indicated that, not all the longitudinal beam reinforcement indicated yielding. Only one top beam longitudinal bar yielded at +3% drift, while two bottom longitudinal beam main bars yielded at -3% drift. Other main bars remained elastic throughout the test. The highest strains in beam main bars were observed at the beam-column interface and within the joint region. Importantly, the column main (longitudinal) bars did not yield, nor did the column and beam stirrups. This strain data indicates that the specimen experienced some beam yielding but maintained elastic behavior in the column and joint reinforcement, suggesting effective load transfer and confinement provided by the steel fibers in the joint region.

While specimen LAHHV_SF was classified as exhibiting joint shear failure (J-type) based on its design and observed behavior, it displayed characteristics unconventional of traditional joint shear failure. These included a delayed onset of joint cracking, gradual

doi:10.6342/NTU202403952

strength degradation instead of a sudden drop, and maintained integrity without severe concrete spalling. The specimen showed ductile behavior similar to beam flexural (B-type) or beam-joint failures (BJ-type). The final failure state showed wide diagonal cracks in the joint region but limited damage to the beam and column. This unique failure pattern suggests that the use of steel fibers in the joint region can modify the typical brittle joint shear failure mode to a more ductile one, potentially improving the overall structural performance under seismic loading.

Figure 6-8 Joint LAHHV-SF at failure stage [96]

6.12 Seismic performance of Beam-Column Joint

6.12.1. Force Transfer Mechanism in Beam-Column Joint

Figure 6-9 demonstrates that when subjected to earthquake-like excitation, significant horizontal and vertical shear forces develop at the junction of beam and column [16]. The magnitudes of the two shear forces exerted to the joint are significantly greater than the shear forces experienced by the other elements connected at the joint.

doi:10.6342/NTU202403952

Furthermore, the joint experiences the most shear force when the beams reach their plastic moment capacity. When the force applied to a joint is greater than its capacity to resist shear, the structure's strength and ability to deform will be restricted. Hence, in designing an external joint, the maximum shear force is considered as the shear demand of the joint and is stated precisely as

$$V_{jh,u} = A_s \Phi f_y - V_c \tag{6-8}$$

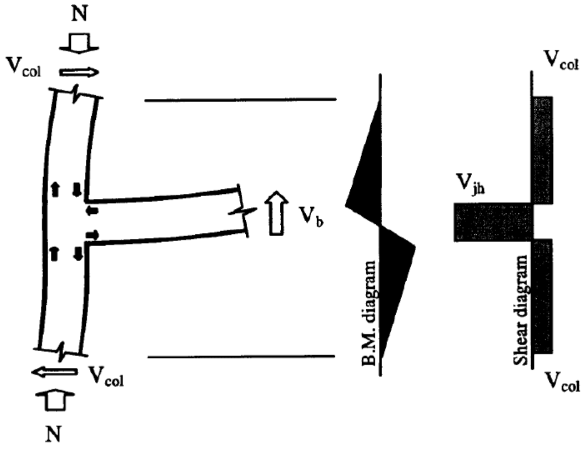

Figure 6-9 An exterior joint under seismic excitation indicating bending moment and shear force diagram [97]

As shown in Figure 6-10, in order to resist the shear force, the resistance from both strut mechanism and truss mechanism in a joint region are considered. The two mechanisms are presented in separate sections below:

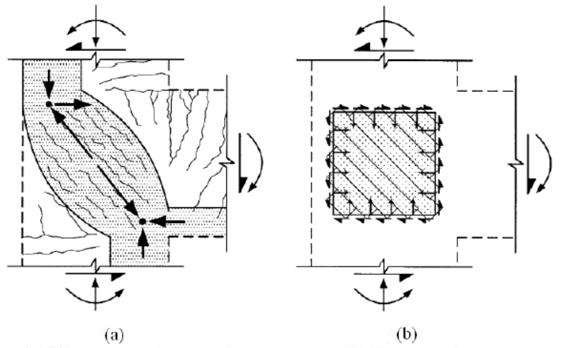

Figure 6-10 Mechanisms of shear transfer at exterior joint (a) Diagonal strut (b) Truss [16]

- **Strut Mechanism:**

The strut mechanism consists of two inclined struts, namely the main strut mechanism (ST1) and the secondary strut mechanism (ST2). These struts are believed to transmit shear forces, as depicted in Figure 6-11. As the tensile stress in the beam reinforcement increases, the primary mechanism of the main strut, which is formed by the hook of the beam reinforcement, carries more forces through a diagonal compression mechanism. Consequently, the secondary strut mechanism's contribution decreases. Therefore, to simplify the analysis, the impact of the secondary strut mechanism is consistently disregarded when estimating shear strength.

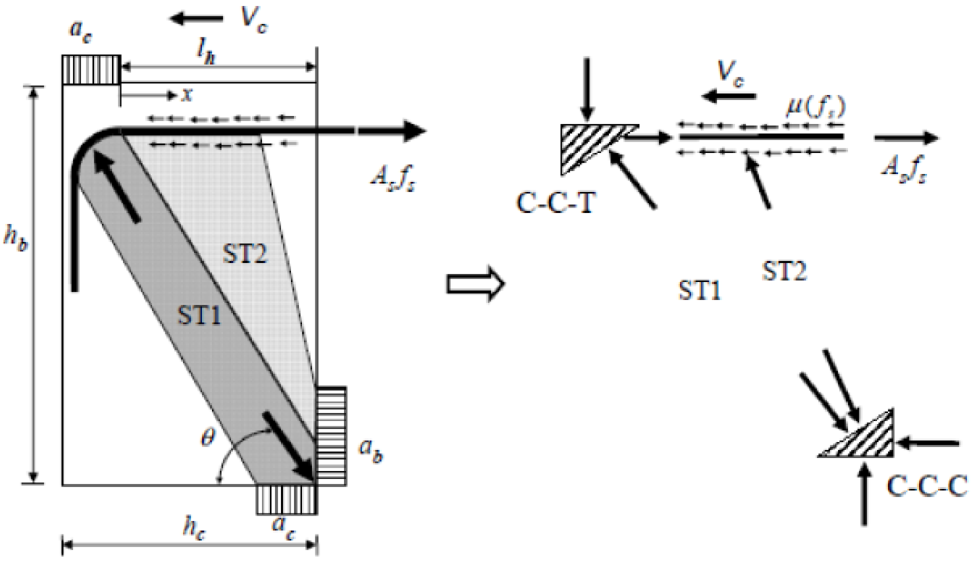

Figure 6-11 Two inclined struts in exterior joints [98]

- **Truss Mechanism**

A truss mechanism is recognized to provide shear resistance by transferring forces from the concrete to the reinforcement. Consequently, the capacity of a truss mechanism is primarily determined by the yielding strength of the reinforcement. However, unlike a strut mechanism, a truss mechanism is heavily influenced by the bond condition because the forces resisted by the truss mechanism are switched from concrete through bond force between concrete and reinforcement. A detailed force transfer mechanism for SFRC beam-column joint is presented in section 2.8.2

6.12.2 Types of Failure in Beam-Column Joints

The failure of a beam-column joint can occur due to either beam flexural failure or joint shear failure, both exhibiting distinct seismic behavior. When developing a structural frame to withstand seismic forces, the principle of strong column-weak beam theory is employed to assure that a beam reaches flexural yielding capacity before a joint and columns fail. Therefore, the occurrence of plastic hinges in a beam and subsequent flexural failure with moderate joint shear deterioration can be classified as a B type failure, which is considered satisfactory in terms of seismic performance. Considering BJ-type failure, the longitudinal reinforcement of the beam reaches its yielding strength, and shortly thereafter, the joint fails under shear due to a substantial decrease in shear capacity. On the other hand, the J-type failure, which displays brittle behavior and considerably less energy dissipation, is the least anticipated failure mode.

6.13 Application of Modified SST for SFRC Beam-Column Joint

6.13.1 Depth of compression zone in beam-column joint

The effective area of the diagonal strut is defined as

$$A_{str} = a_s b_s \tag{6-9}$$

Where, a_s and b_s is the depth and width of the diagonal strut. The depth of a diagonal strut, which relies on the end conditions created by the compression zones in beams and columns, can be calculated without a beam hinge forming at the column face as follows.

doi:10.6342/NTU202403952

$$a_s = \sqrt{a_b^2 + a_c^2} \tag{6-10}$$

Where, a_b and a_c represents the depth of compression zones in beams and columns.

After assuming beam hinge occurs at the face of the column, and neglecting a_b in computing a_s which is mathematically indicated by, $a_s = a_c$, where a_c is the depth of compression zone in column as shown in Figure 6-12. Therefore in columns, because of the participation of axial load and multiple layers of tensile reinforcement, the depth of flexural compression zone is calculated as given in Eq. (6-11). Where, h_c represents the depth of the column.

$$a_c = \left[0.25 + 0.85\left(\frac{N}{A_g f_c'}\right)\right] h_c \tag{6-11}$$

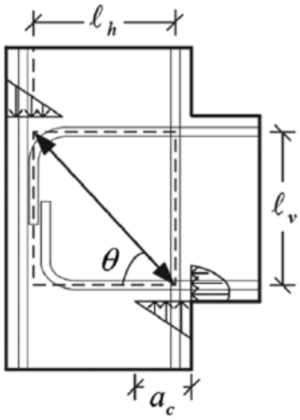

Figure 6-12 Illustration for Beam-Column [63]

6.13.2 Sample calculation for SFRC Beam-Column Joint based on Modified SST for SFRC

The beam-column joint LAHHV-SF tested by Chang (2017) [96] and failed in Joint (J-Type) is considered for the sample calculation.

<table>
<tr><td>Given
Parameters</td><td>Specimen ID: LAHHV-SF
$V_{u(demand)} = V_u = 5386.52\ kN$</td></tr>
<tr><td rowspan="2">Given Parameters</td><td>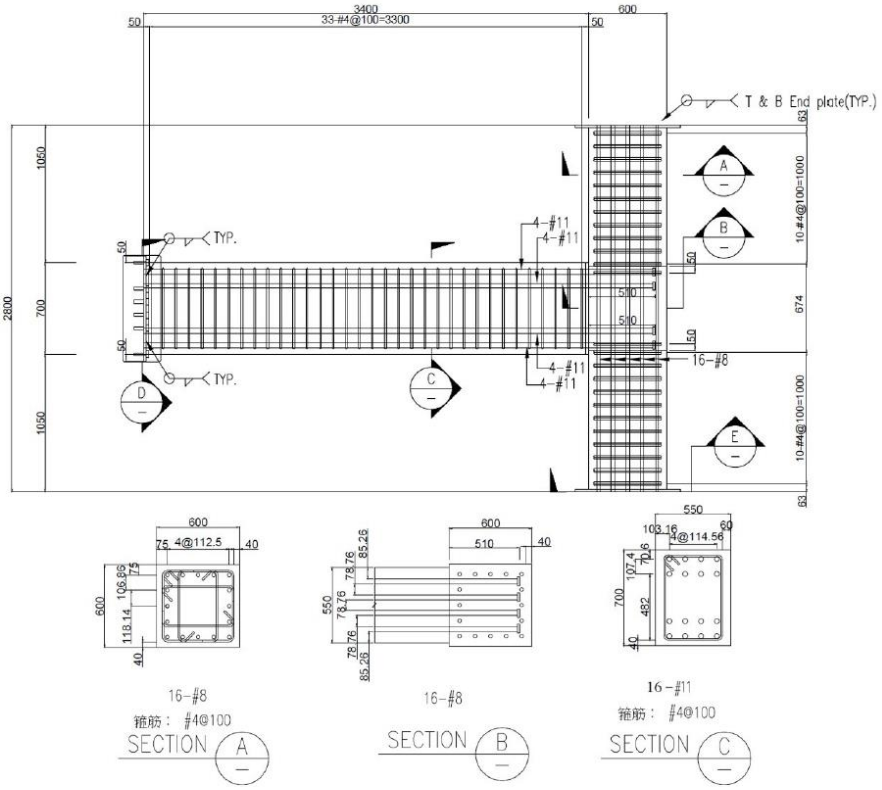
</td></tr>
<tr><td>Dimensions of Beam c/s = $400 \times 700mm$
Dimensions of column c/s = $600 \times 600mm$
Number of bars in horizontal Direction (Joint) = 0 nos.
Number of bars in vertical Direction (Joint) = 6 nos.
Area of Horizontal Bar (Joint) = 0 mm^2
Area of Horizontal Bar (Joint) = 284 mm^2
Area of Vertical Bar (Joint) = 509 mm^2
$f_y = 600\ MPa$
$f_c' = 68\ MPa$
$V_f = 0.015$ (Fraction)
$l_f = 30mm$
$d_f = 0.38mm$
$\alpha = 0.05$
$\lambda = 0.5$
$\tau_{eq} = 8MPa$
$\frac{N}{A_g f_c'} = 0.1$</td></tr>
</table>

doi:10.6342/NTU202403952

Solution

Step 1: Calculation of A_{str} and θ

$$a_c = \left[0.25 + 0.85\left(\frac{N}{A_g f_c'}\right)\right] h_c = [0.25 + 0.85(0.1)](600) = 201\,mm^2$$

$$A_{str} = a_s b_s = 201 \times 600 = 120600\,mm^2 \qquad \because a_c = a_s$$

$$\theta = \tan^{-1}\left(\frac{l_v}{l_h}\right) = \tan^{-1}\left(\frac{529.2}{444.6}\right) = 49.96°$$

Step 2: Properties of SFRC

$$\varepsilon_r = \frac{\varepsilon_h + \varepsilon_v - \varepsilon_d}{\left(0.1 S_f\right) + 1} = \frac{0.009}{\left(0.1 \times 8 \times 0.015 \times \frac{30}{0.38}\right) + 1} = 0.0046$$

$$\sigma_{cc} = \sigma_{mu}\left(1 - V_f\right) + \alpha \tau_{eq} V_f \left(\frac{l_f}{d_f}\right)$$

$$\therefore \sigma_{cc} = [4.61(1 - 0.015)] + \left[0.05 \times 8 \times 0.015 \times \frac{30}{0.38}\right] = 5.022\,MPa$$

$$\sigma_{pc} = \lambda \tau_{eq} V_f \left(\frac{l_f}{d_f}\right)$$

$$\therefore \sigma_{pc} = 0.5 \times 8 \times 0.015 \times \frac{30}{0.38} = 4.736\,MPa$$

$$f_{c1} = \sigma_{cc} + \frac{\sigma_{pc} - \sigma_{cc}}{0.007 - \epsilon_{cc}} \times (\epsilon_{\mathrm{r}} - \epsilon_{cc})$$

$$\therefore f_{c1} = 5.022 + \frac{4.736 - 5.022}{0.007 - 0.000162} \times (0.0046 - 0.000162)$$

$$= 4.836 MPa$$

Step 3: Yielding forces of the ties

$$F_{yh} = (l_s \times f_{c1} \times h_c \times sin\theta \times 10^{-3})$$

$$\therefore F_{yh} = (691.174 \times 4.836 \times 600 \times sin49.46° \times 10^{-3})$$

$$= 1535.567\,kN$$

$$F_{yv} = \left(A_{tv} f_{yv} \times 10^{-3}\right) + \left(l_s \times f_{c1} \times h_c \times cos\theta \times 10^{-3}\right)$$

$$\therefore F_{yv} = \left(6 \times 509 \times 600 \times 10^{-3}\right)$$

$$+ \left(691.174 \times 4.836 \times 600 \times cos49.96° \times 10^{-3}\right)$$

$$= 3122.485\ kN$$

Step 4: Force distribution

$$\gamma_h = \frac{2\ \tan\theta - 1}{3} = \frac{2\ \tan 49.96° - 1}{3} = 0.4602$$

$$\gamma_v = \frac{2\ \cot\theta - 1}{3} = \frac{2\ \cot 49.96° - 1}{3} = 0.2268$$

Step 5: Balanced amounts of tie forces

$$\overline{K_h} = \frac{1}{1 - 0.2(\gamma_h + \gamma_h^2)} = \frac{1}{1 - 0.2(0.460 + 0.460^2)} = 1.155$$

$$\overline{K_v} = \frac{1}{1 - 0.2(\gamma_v + \gamma_v^2)} = \frac{1}{1 - 0.2(0.227 + 0.227^2)} = 1.058$$

Step 6: Softening of concrete

$$\zeta = \left(1 + 0.07 S_f\right) \times min\left(\frac{5.8}{\sqrt{68}},\ 0.9\right) \times \frac{1}{\sqrt{1 + 400 \times 0.0046}} = 0.693$$

Where, $S_f = 0.015 \times \frac{30}{0.38} \times 8$

$$\overline{F_h} = \gamma_h \times \left(\overline{K_h} \zeta f_c' A_{str}\right) \times \cos\theta$$

$$\therefore \overline{F_h} = 0.4602 \times 1.155 \times 0.693 \times 69 \times 120600 \times cos49.96°$$

$$= 1943.75 kN$$

$$\bar{F}_v = \gamma_v \times \left(\overline{K_v} \zeta f_c' A_{str}\right) \times \sin\theta$$

$$\therefore \bar{F}_v = 0.2268 \times 1.058 \times 0.693 \times 69 \times 120600 \times sin49.96°$$

$$= 1044.955 kN$$

Step 7: Tie index

$$K_h = 1 + \left(\overline{K_h} - 1\right)\left(F_{yh}/\overline{F_h}\right)$$

$$\therefore K_h = 1 + (1.155 - 1)\left(\frac{1535.567}{1943.75}\right) = 1.122 < \overline{K_h}$$

take, $K_h = 1.122$

$$K_v = 1 + (\overline{K_v} - 1)\left(F_{yv}/\overline{F}_v\right)$$

$$\therefore K_v = 1 + (1.058 - 1)\left(\frac{3122.485}{1044.955}\right) = 1.176 > \overline{K_v}$$

take, $K_v = 1.058$

Step 8: **Compressive strength of the strut**

$$C_{d,n} = (K_h + K_v - 1)\zeta f_c' A_{str}$$

$$\therefore C_{d,n} = (1.122 + 1.058 - 1) \times 0.693 \times 68 \times 120600 \times 10^{-3}$$

$$= 6706.122 \text{ kN}$$

$$\boldsymbol{V_{ucal} = 6706.122 \times cos 49.96° = 4314.197\text{kN}}$$

Strength Ratio

$$\frac{V_u(orV_{u(demand)})}{V_{ucal}} = \frac{5386.52}{4314.197} = 1.248$$

Results for Condition 1 (Based on Table 4-6):

$$\boldsymbol{V_{ucal} = 7548 \times cos 49.96° = 4855.796\text{kN}}$$

Results for Condition 2 (Based on Table 4-6):

$$\boldsymbol{V_{ucal} = 6272.3 \times cos 49.96° = 4035.528\text{kN}}$$

6.14 Summary for Application of Modified SST for SFRC Beam-Column Joint

This section discusses the application of a Softened Strut-and-Tie (SST) model for Steel Fiber Reinforced Concrete (SFRC) beam-column joints. It outlines the force transfer mechanisms in beam-column joints, including strut and truss mechanisms, and explains the shear resistance provided by concrete, transverse reinforcement, and steel fibers (Section 2.8.2).

The proposed SST for SFRC is applied to SFRC beam-column joints, with a detailed sample calculation provided for a specimen that failed in joint shear. The calculation process includes determining the effective area of the diagonal strut, calculating SFRC properties, yielding forces of ties, force distribution, and concrete softening. The model's prediction for the beam-column joint failure in J-Type is compared with experimental results. Additionally, the calculated results for Condition 1 and Condition 2 from Table 4-6 are presented under sample calculation. The value of ζ (Condition 3) does not exhibit sensitivity to varying values of τ_{eq}, as it does not account for the influence of fiber addition. SFRC indicated more gradual softening process due to its enhanced ductility and ability to retain residual strength and toughness even after substantial cracking, unlike traditional reinforced concrete. Therefore, the equation of ζ (Condition 3) could be further refined to extend its applicability to SFRC. Considering the effect of Condition 3 on the calculated results for isolated strut panels, deep beams, and beam-column joints, this study recommends the use of Eq. (4-25) for ζ, as proposed by Hung (2020), which is applicable for both NSC and HSC, and accounts for the effects of τ_{eq}, V_f, and $\left(\frac{l_f}{d_f}\right)$.

doi:10.6342/NTU202403952

Chapter 7 Conclusions & Recommendations for Future Research

7.1 Conclusions

The overall objective of this research is to propose shear and compressive strength analysis procedure for steel fiber reinforced concrete (SFRC) D-region elements. Two distinct shear analysis procedures namely, Modified Compression Field Theory (MCFT) and Softened Strut-and-Tie (SST) Model were modified in this research to consider the effect of fiber addition.

The presence of fibers enhances the bridging effect over cracks, resistance to spalling, leading to improved shear and tensile performance in SFRC panel specimens compared to conventionally reinforced concrete panels. This improvement is attributed to the strain-hardening behavior of the fibers.

The key observations are for the two modified theories are summarized as follows.

1. **Modified Compression Field Theory for SFRC**

    - The data for 6 panels subjected to shear loading were analyzed in this research with 3 RC panels and 3 SFRC panels. For the Modification of MCFT, the experimental stress-strain behavior of SFRC panels was analyzed, which indicated the strain hardening behavior. Based on these observations, the tension model for calculating the tensile stress in concrete was incorporated with some other minor modifications to account for the effect when the reinforcement is provided in horizontal direction only.
    - The outlined analysis approach enhances the applicability of MCFT in predicting the shear stress-strain characteristics of SFRC panels by integrating

doi:10.6342/NTU202403952

the strain-hardening contribution of the fibers. The parameters α, λ, and τ_{eq} acquired from the tension model impact the sensitivity of the prediction.

- The suggested analysis approach was verified through a comparison of the predicted results with experimental data from 30 SFRC panels. This approach accurately predicted both the shear strength and the failure pattern, demonstrating its effectiveness.

2. Softened Strut-and-Tie (SST) Model for SFRC

- The experimental results for 43 isolated strut square and rectangular panels with different fiber volume fraction, reinforcement layout, and yield strength of the reinforcement. The test result shows that when adding steel fiber in concrete, specimens with brittle splitting failure could change its failure mode to concrete crushing. Both cracking strength and ultimate strength increase with the presence of steel fiber. Compared to non-fibrous specimens with transverse reinforcement, panels with steel fiber can increase cracking strength and ultimate strength up to 40% and 30%, respectively.
- To extend the applicability of the SST to consider the effect of fiber addition, the effect of fiber addition were added in the yielding forces F_y of the tie by incorporating the appropriate material constitutive laws for SFRC.
- Based on the analysis of strain gauge data, the average strain values for $\varepsilon_h, \varepsilon_v$ and ε_d were proposed for SFRC respectively as 0.003, -0.003, and -0.003.
- A new equation to calculate the principal tensile strain in SFRC that is $\varepsilon_{r(SFRC)}$ is proposed, considering the effect of fiber volume fraction (V_f), fiber aspect ratio l_f/d_f and equivalent bond strength τ_{eq}.

doi:10.6342/NTU202403952

- The accuracy of the presented analysis procedure was verified by analyzing various RC and SFRC isolated strut panel specimens. The compressive strength calculated using the modified SST demonstrated a close concurrence with the values obtained from the experiments, regardless of the layout of the reinforcement in the panel.
- Furthermore, the Modified SST was applied to calculate the shear strength of D-region elements (deep beams and beam-column joints) and compared with the experimental shear strength data obtained from the literature.

In conclusion, the study demonstrates the reliable tool for evaluating the shear and compression capacity of steel fiber-reinforced concrete elements.

7.2 Recommendations for Future Research

1) Using SFRC is becoming progressively more important to handle realistic engineering problems. Based on MCFT and SST, the proposed study can assist researchers and structural engineers in developing computer algorithms for predicting shear strength, fully utilizing the strain-hardening characteristics of SFRC in structural applications.

2) MCFT for SFRC can be expanded for estimating the shear strength of D-Region elements.

3) The modified SST presented in this study has been applied to and verified with exterior beam-column joints with low axial loads. Nevertheless, its use can be expanded for predicting the shear capacity of internal SFRC joints, which usually have high axial loads. Additionally, the modified SST can be extended to predict the strength of shear walls.

doi:10.6342/NTU202403952

REFERENCE

[1] ACI Committee 363, High-Strength Concrete (ACI 363R), American Concrete Institute, Farmington Hills, MI 48331, 2005.

[2] S. Chasioti, Hybrid Steel Fibre Reinforced Concrete in Shear: From the Material to the Structural Level, (2017) 353. https://hdl.handle.net/1807/80894.

[3] T.T.C. Hsu, Y.L. Mo, Unified Theory of Concrete Structures, John Wiley & Sons, Ltd, 2010.

[4] J. Schlaich, K. Schäfer, M. Jennewein, Toward a Consistent Design of Structural Concrete, 1987. https://doi.org/10.15554/pcij.05011987.74.150.

[5] A.E. Naaman, H. Najm, Bond-Slip Mechanisms of Steel Fibers in Concrete, ACI Materials Journal. 88 (1991) 135–145. https://doi.org/10.14359/1896.

[6] Y. Kwak, M.O. Eberhard, W. Kim, J. Kim, Shear Strength of Steel Fiber-Reinforced Concrete Beams without Stirrups, ACI Structural Journal. 99 (2002) 530–538.

[7] J. Susetyo, P. Gauvreau, F.J. Vecchio, Effectiveness of Steel Fiber as Minimum Shear Reinforcement, ACI Structural Journal. 108 (2011) 488–496.

[8] S.K. Wagh, A. Vianthi, W.-C. Liao, Experimental and MCFT-Based Study on Steel Fiber-Reinforced Concrete Subjected to In-Plane Shear Forces, International Journal of Concrete Structures and Materials. 17 (2023) 1–13. https://doi.org/10.1186/s40069-023-00586-4.

[9] S.C. Lee, J.Y. Cho, F.J. Vecchio, Diverse Embedment Model for Steel Fiber-Reinforced Concrete in Tension: Model Development, ACI Materials Journal. 110

(2011) 516–525. https://doi.org/10.14359/51685787.

[10] W.-C. Liao, W. Perceka, E.-J. Liu, Compressive Stress-Strain Relationship of High Strength Steel Fiber Reinforced Concrete, Journal of Advanced Concrete Technology. 13 (2015) 379–392. https://doi.org/10.3151/jact.13.379.

[11] W. Perceka, W.C. Liao, Y. De Wang, High Strength Concrete Columns under Axial Compression Load: Hybrid Confinement Efficiency of High Strength Transverse Reinforcement and Steel Fibers, Materials. 9 (2016). https://doi.org/10.3390/ma9040264.

[12] D.K. Sahoo, R.K. Gautam, B. Singh, P. Bhargava, Strength and deformation characteristics of bottle-shaped struts, Magazine of Concrete Research. 60 (2008) 137–144. https://doi.org/10.1680/macr.2008.60.2.137.

[13] R. Narayanan, I.Y.S. Darwish, Fiber Concrete Deep Beams in Shear, ACI Structural Journal. 85 (1988) 141–149. https://doi.org/10.14359/2698.

[14] F.J. Vecchio, M.P. Collins, The Modified Compression-Field Theory for Reinforced Concrete Elements Subjected to Shear, ACI Journal. 83 (1986) 219–231.

[15] V. Sadeghian, F. Vecchio, SP-328 — 3 The modified compression field theory: Then and now, ACI Special Publication SP-328, 2018.

[16] S.-J. Hwang, H.-J. Lee, Analytical Model for Predicting Shear Strengths of Exterior Reinforced Concrete Beam-Column Joints for Seismic Resistance, ACI Structural Journal. 96 (1999) 846–858.

[17] S.-J. Hwang, W.-Y. Lu, H.-J. Lee, Shear Strength Prediction for Deep Beams, ACI Structural Journal. 97 (2000) 367–376. https://doi.org/10.14359/9624.

doi:10.6342/NTU202403952

[18] S.-J. Hwang, H.-J. Lee, Analytical Model for Predicting Shear Strengths of Interior Reinforced Concrete Beam-Column Joints for Seismic Resistance, ACI Structural Journal. 97 (2000) 35–44.

[19] S.-J. Hwang, W.-Y. Lu, H.-J. Lee, Shear Strength Prediction for Reinforced Concrete Corbels, ACI Structural Journal. 97 (2000) 543–552.

[20] S.-J. Hwang, W.-H. Fang, H.-J. Lee, H. Yu, Analytical Model for Predicting Shear Strength of Squat Walls, Journal of Structural Engineering. 127 (2001) 43–50.

[21] S. Mogili, J.S. Kuang, S.-J. Hwang, Predicting Shear Strength of Reinforced Concrete Knee Joints in Closing and Opening Actions, Journal of Structural Engineering. 146 (2020). https://doi.org/10.1061/(asce)st.1943-541x.0002633.

[22] S. Mogili, S.-J. Hwang, Softened Strut-and-Tie Model for Shear and Flexural Strengths of Reinforced Concrete Pile Caps, Journal of Structural Engineering. 147 (2021). https://doi.org/10.1061/(asce)st.1943-541x.0003141.

[23] D.A. Fanella, A.E. Naaman, Stress-Strain Properties of Fiber Reinforced Mortar in Compression., ACI Journal. 82 (1985) 475–483. https://doi.org/10.14359/10359.

[24] A.E. Naaman, J.R. Homrich, Properties of High-Strength Fiber Reinforced Concrete, ACI Special Publications. 87 (1985).

[25] L.S. Hsu, C.T.T. Hsu, Stress-strain behavior of steel-fiber high-strength concrete under compression, ACI Structural Journal. 91 (1994) 448–457. https://doi.org/10.14359/4152.

[26] J. Thomas, A. Ramaswamy, Mechanical Properties of Steel Fiber-Reinforced Concrete, JOURNAL OF MATERIALS IN CIVIL ENGINEERING. 19 (2007) 385–392. https://doi.org/10.1061/(ASCE)0899-1561(2007)19.

[27] P.S. Song, S. Hwang, Mechanical properties of high-strength steel fiber-reinforced concrete, Construction and Building Materials. 18 (2004) 669–673. https://doi.org/10.1016/j.conbuildmat.2004.04.027.

[28] F.F. Wafa, S.A. Ashour, Mechanical Properties of high-strength fiber reinforced concrete, ACI Materials Journal. 89 (1992) 449–455.

[29] Ş. Yazici, G. Inan, V. Tabak, Effect of aspect ratio and volume fraction of steel fiber on the mechanical properties of SFRC, Construction and Building Materials. 21 (2007) 1250–1253. https://doi.org/10.1016/j.conbuildmat.2006.05.025.

[30] M.P. Collins, D. Mitchell, Prestressed Concrete Structures, 1991.

[31] R. Evans, M. Marathe, Microcracking and Stress-Strain Curves for Concrete in Tension, Materials and Structures. 1 (1968) 61–64.

[32] W.C. Liao, S.H. Chao, S.Y. Park, A.E. Naaman, Self-Consolidating High Performance Fiber Reinforced Concrete (SCHPFRC) - Preliminary Investigation UMCEE 06-02, 2006.

[33] A.E. Naaman, High Performance Fiber Reinforced Cement Composites: Classification and Application, CBM-CI International Workshop, Pakistan. (2003).

[34] A.P. Fantilli, H. Mihashi, P. Vallini, Multiple cracking and strain hardening in fiber-reinforced concrete under uniaxial tension, Cement and Concrete Research. 39 (2009) 1217–1229. https://doi.org/10.1016/j.cemconres.2009.08.020.

[35] A.S. Ezeldin, P.N. Balaguru, Bond behavior of normal and high-strength fiber reinforced concrete, ACI Materials Journal. 86 (1989) 515–524. https://doi.org/10.14359/2141.

[36] M.H. Harajli, M. Hout, W. Jalkh, Local bond stress-slip behavior of reinforcing

bars embedded in lightweight aggregate concrete, ACI Materials Journal. 92 (1995) 343–354. https://doi.org/10.12989/cac.2015.16.3.449.

[37] S. Hota, A.E. Naaman, Bond stress-slip response of reinforcing bars embedded in FRC matrices under monotonic and cyclic loading, ACI Structural Journal. 94 (1997) 525–537. https://doi.org/10.14359/502.

[38] J.R. Robinson, Essais a l’effort Trenchant de Pouters a Ame Mince en Beton Arme, Paris, 1961.

[39] A. Belarbi, T.T.C. Hsu, Constitutive Laws of Softened Concrete in Biaxial Tension-Compression, ACI Structural Journal Journal. 92 (1995) 562–573. https://doi.org/10.14359/907.

[40] L.-X. “Bob” Zhang, T.T.C. Hsu, Behavior and Analysis of 100 MPa Concrete Membrane Elements, Journal of Structural Engineering. 124 (1998) 24–34. https://doi.org/10.1016/s0026-0576(00)81718-3.

[41] M.Y. Mansour, T.T.C. Hsu, Y.-L. Mo, Constitutive Relations of Cracked Reinforced Concrete with Steel Fibers, American Concrete Institute, ACI Special Publication. (2009) 101–121. https://doi.org/10.14359/51663292.

[42] H.J. Lee, A Study of Shear Strength of Reinforced Concrete Beam-Column Joints for Earthquake Resistance, National Taiwan University of Science and Technology, Taipei, Taiwan, 2000.

[43] J.M. Alwan, A.E. Naaman, W. Hansen, Pull-out work of steel fibers from cementitious composites: Analytical investigation, Cement and Concrete Composites. 13 (1991) 247–255. https://doi.org/10.1016/0958-9465(91)90030-L.

[44] A.E. Naaman, High Performance Fiber Reinforced Cement Composites “Concrete

Structures for the future," IABSE Symposium. (1987) 371–376.

[45] A.E. Naaman, H.W. Reinhardt, Characterization of High Performance Fiber Reinforced Cement Composites, in: 2nd International Workshop on HPFRCC, High Performance Fiber Reinforced Cement Composites: HPFRCC 2, RILEM, London, 1996: pp. 1–24.

[46] D.J. Kim, S. El-Tawil, A. Naaman, Correlation between Single Fiber Pullout and Tensile Response of FRC Composites with High Strength Steel Fibers, High Performance Reinforced Cement Composites (HPFRCC5). (2007) 67–76.

[47] B.W. Xu, J.W. Ju, H.S. Shi, Progressive Micromechanical Modeling for Pullout Energy of Hooked-end Steel Fiber in Cement-based Composites, International Journal of Damage Mechanics. 20 (2011) 922–938. https://doi.org/10.1177/1056789510385260.

[48] V.C. Li, Y. Wang, S. Backer, Effect of inclining angle, bundling and surface treatment on synthetic fibre pull-out from a cement matrix, Composites. 21 (1990) 132–140.

[49] V.C. Li, R. Ward, A.M. Hamza, Steel and synthetic fibers as shear reinforcement, ACI Materials Journal. 89 (1992) 499–508. https://doi.org/10.14359/1822.

[50] J.M. Alwan, A.E. Naaman, P. Guerrero, Effect of Mechanical Clamping on The Pull Out Response of Hooked Steel Fibers Embedded in Cementitious Matrices, Concrete Science and Engineering. 1 (1999) 15–25.

[51] Z.Y. Dong, Q. Bin Li, Interfacial pullout model for hooked fiber in cementitious materials, Engineering Mechanics. 21 (2004) 102–107.

[52] S.H. Cho, Y. Il Kim, Effects of Steel Fibers on Short Beams Loaded in Shear, ACI

Structural Journal. 100 (2003) 765–774. https://doi.org/10.14359/12843.

[53] S.A. Ashour, G.S. Hasanain, F.F. Wafa, Shear Behavior of High-Strength Fiber Reinforced Concrete Beams, ACI Structural Journal. 89 (1992) 176–184.

[54] F. Minelli, G.A. Plizzari, On the effectiveness of steel fibers as shear reinforcement, ACI Structural Journal. 110 (2013) 379–389. https://doi.org/10.14359/51685596.

[55] H.H. Dinh, Shear behavior of steel fiber reinforced concrete beams Without stirrup reinforcement, The University of Michigan, 2009.

[56] H. Nilson, A, D. Darwin, W. Dolan, C, Design of Concrete Structures, 14th ed., McGraw-Hill, NY, USA, 2010.

[57] M.D. Brown, C.L. Sankovich, O. Bayrak, J.O. Jirsa, Behavior and Efficiency of Bottle-Shaped Struts, ACI Structural Journal. 103 (2006) 348–355.

[58] D.K. Sahoo, B. Singh, P. Bhargava, Investigation of Dispersion of Compression in Bottle-Shaped Struts, ACI Structural Journal. 106 (2009) 178–186.

[59] D.K. Sahoo, B. Singh, P. Bhargava, Minimum Reinforcement for Preventing Splitting Failure in Bottle-Shaped Struts, ACI Structural Journal. 108 (2011) 206–216. https://doi.org/10.14359/51664256.

[60] ACI Committee, Building Code Requirements for Structural Concrete and Commentary, American Concrete Institute, Farmington Hills, MI, 2002.

[61] M.P. Collins, D. Mitchell, P. Adebar, F.J. Vecchio, A General Shear Design Method, ACI Structural Journal. 93 (1996) 36–45.

[62] J.C. Walraven, Fundamental Analysis of Aggregate Interlock, Journal of Structural Division. 107 (1981) 2245–2270.

[63] S.-J. Hwang, R.-J. Tsai, W.-K. Lam, J.P. Moehle, Simplification of Softened Strut-and-Tie Model for Strength Prediction of Discontinuity Regions, ACI Structural Journal. 114 (2017) 1239–1248. https://doi.org/10.14359/51689787.

[64] S.-J. Hwang, H.-J. Lee, Strength Prediction for Discontinuity Regions by Softened Strut-and-Tie Model, Journal of Structural Engineering. 128 (2002) 1519–1526. https://doi.org/10.1061/(asce)0733-9445(2002)128:12(1519).

[65] K. Schäfer, Strut-and-Tie Models for Design of Structural Concrete, Tainan, Taiwan, 1996.

[66] M. Jennewein, K. Schäfer, Standardisierte Nachweise von häufigen D-Bereichen, Berlin, 1992.

[67] X.B. Pang, T.T.C. Hsu, Fixed angle softened truss model for reinforced concrete, ACI Structural Journal. 93 (1996) 197–207. https://doi.org/10.14359/1452.

[68] N. Shahin, A. Salah, D. Kalliontzis, Softened membrane model for shear of ultra-high-performance concrete (SMM-UHPC), Engineering Structures. 308 (2024) 117956. https://doi.org/10.1016/j.engstruct.2024.117956.

[69] T. Zsutty, Shear strength prediction for separate ctegories of siple beam tests, ACI Journal. 68 (1971) 138–143. https://doi.org/10.14359/11300.

[70] M. Khuntia, B. Stojadinovic, S.C. Goel, Shear strength of normal and high-strength fiber reinforced concrete beams without stirrups, ACI Structural Journal. 96 (1999) 282–289. https://doi.org/10.14359/620.

[71] T. Jiuru, C. Hu, K. Yang, Y. Yan, Seismic Behavior and Shear Strength of Framed Joint Using Steel-Fiber Reinforced Concrete, Journal of Structural Engineering. 118 (1992) 341–358.

[72] T.Y. Lim, P. Paramasivam, S.L. Lee, Analytical Model for Tensile Behavior of Steel-Fiber Concrete., ACI Materials Journal. 84 (1987) 286–298. https://doi.org/10.14359/1454.

[73] M.P. Collins, Towards a rational Theory for RC Members in Shear, in: ASCE, 1978: pp. 649–666.

[74] D. Mitchell, M.P. Collins, Diagonal Compression Field Theory - A Rational Model for Structural Concrete in Pure Torsion, ACI Journal. 71 (1974) 396–408.

[75] J. Susetyo, Fibre Reinforcement for Shrinkage Crack Control in Prestressed , Precast Segmental Bridges, University of Toronto, 2009.

[76] F. Vecchio, The Response of Reinforced Concrete to In-Plane Shear and Normal Stresses, University of Toronto, 1982.

[77] A.E. Naaman, A Statistical Theory of Strength for Fiber Reinforced Concrete, Massachusetts Institute of Technology, 1972.

[78] J.Y.L. Voo, S.J. Foster, Variable Engagement Model for Fibre Reinforced Concrete in Tension, 2003.

[79] S. Chao, W. Liao, T. Wongtanakitcharoen, A. Naaman, Large Scale Tensile Tests of High Performance Fiber Reinforced Large Scale Tensile Tests of High Performance Fiber, in: Fifth International RILEM Workshop on High Performance Fiber Reinforced Cement Composites (HPFRCC5), 2007.

[80] J.W. Luo, F.J. Vecchio, Behavior of steel fiber-reinforced concrete under reversed cyclic shear, ACI Structural Journal. 113 (2016) 75–84. https://doi.org/10.14359/51687940.

[81] D. Carnovale, F.J. Vecchio, Effect of fiber material and loading history on shear

behavior of fiber-reinforced concrete, ACI Structural Journal. 111 (2014) 1235–1244. https://doi.org/10.14359/51686809.

[82] W.C. Liao, P.S. Chen, C.W. Hung, S.K. Wagh, An innovative test method for tensile strength of concrete by applying the strut-and-tie methodology, Materials. 13 (2020) 1–20. https://doi.org/10.3390/ma13122776.

[83] Y. Guyon, Prestressed concrete, 1953. https://doi.org/10.4324/9780203404386_chapter_16.

[84] C.-W. Hung, The Effect of Steel Fiber on Bottle-Shaped Strut-and-Tie Behavior of High Srength Concrete, National Tawian University. (in Chinese), 2020. https://doi.org/10.6342/NTU202002509.

[85] C.-C. Kuo, Experimental Investigation on Isolated Strut Behavior of High Strength Steel Fiber Reinforced Concrete Panels, National Taiwan University. (in Chinese), 2019. https://doi.org/10.6342/NTU201902816.

[86] F.J. Vecchio, M.P. Collins, Compression Response of Cracked Reinforced Concrete, Journal of Structural Engin. 119 (1993) 3590–3610. https://doi.org/10.1360/csb1994-39-15-1380.

[87] W.C. Liao, W. Perceka, L.C. Yu, Systematic mix procedures for highly flowable-strain hardening fiber reinforced concrete (HF-SHFRC) by using tensile strain hardening responses as performance criteria, Science of Advanced Materials. 9 (2017) 1157–1168. https://doi.org/10.1166/sam.2017.3097.

[88] W. Perceka, W.C. Liao, Shear Strength Model for Steel Fiber-Reinforced Concrete Columns, ACI Structural Journal. 120 (2023) 35–47. https://doi.org/10.14359/51739084.

[89] K.-N. Chi, TTK's Products and Structural RC Members Testing, 2014.

[90] W.-C. Chen, Shear Behavior of High Strength Steel Fiber Reinforced Concrete Deep Beams, National Taiwan University. (in Chinese), 2018. https://doi.org/10.6342/NTU201802974.

[91] American Committee 318, Building Code Requirements for Structural Concrete (ACI 318-19) and Commentary, American Concrete Institute, Farmington Hills, MI, Farmington Hills, MI 48331, 2019.

[92] J. Liu, B.I. Mihaylov, A comparative study of models for shear strength of reinforced concrete deep beams, Engineering Structures. 112 (2016) 81–89. https://doi.org/10.1016/j.engstruct.2016.01.012.

[93] Long, Nguyen-Minh, R. Marián, New formula for the estimation of shear resistance of fibre reinforced beams, Canadian Journal of Civil Engineering. 38 (2011) 23–35. https://doi.org/10.1139/L10-107.

[94] L. Vandewalle, Recommendations of RILEM TC162- TDF: Test and design methods for steel-fibre-reinforced-concrete: σ-ε design method, Materials and Structures. 33 (2000) 75–81.

[95] A.E. Naaman, Fiber Reinforced Cement and Concrete Composites, Techno Press 3000, Sarasota, FL, USA, 2018.

[96] K.-Y. Chang, Shear Strength and Cyclic Behavior of High Strength Steel Fiber Reinforced Concrete Exterior Beam-Column Joints, National Taiwan University. (in Chinese), 2017. https://doi.org/10.6342/NTU201703794.

[97] H.-F. Wong, Shear strength & seismic performance of non-seismically designed reinforced concrete beam-column joints, The Hong Kong University of Science

doi:10.6342/NTU202403952

and Technology, 2005.

[98] S. Park, K.M. Mosalam, Shear Strength Models of Exterior Beam-Column Joints without Transverse Reinforcement, 2009. http://peer.berkeley.edu/publications/peer_reports/reports_2009/web_PEER9106_PARK_Mosalam.pdf.

[99] M.S.V. Sagi, C. Lakavath, S. Suriya Prakash, Effect of steel fibers on the shear behavior of Self-Compacting reinforced concrete deep Beams: An experimental investigation and analytical model, Engineering Structures. 269 (2022) 1–14. https://doi.org/10.1016/j.engstruct.2022.114802.

Appendix A Verification of Proposed MCFT with an experimental data set for panels under in-plane shear

Reference	**Specimen ID**	**Loading Type**	**f'_c (MPa)**	**ρ_{sx} (%)**	**f_{yx} (MPa)**	**E_s (GPa)**	**s_m (mm)**	**Fibre Layout**	**Fiber Type**	**V_f (%)**	**l_f (mm)**	**d_f (mm)**	**v_{uexp} (MPa)**	**v_{umodel} (MPa)**	**v_{uexp}/v_{umodel}**
[75]	C1F1V1	Monotonic	51.4	3.31	552	225	114.4	Single	RC80/50-BN	0.5	50	0.62	3.53	4.01	0.88
	C1F1V2	Monotonic	53.4	3.31	552	225	54.7	Single	RC80/50-BN	1.0	50	0.62	5.17	4.99	1.04
	C1F1V3	Monotonic	49.7	3.31	552	225	57.2	Single	RC80/50-BN	1.5	50	0.62	5.37	5.34	1.01
	C1F2V3	Monotonic	59.7	3.31	552	225	38.1	Single	RC80/30-BP	1.5	30	0.38	6.68	6.62	1.01
	C1F3V3	Monotonic	45.5	3.31	552	225	57.2	Single	RC65/35-BN	1.5	35	0.55	5.59	5.05	1.11
	C2F1V3	Monotonic	79.0	3.31	552	225	36.0	Single	RC80/50-BN	1.5	50	0.62	6.90	6.36	1.09
	C2F2V3	Monotonic	76.5	3.31	552	225	46.6	Single	RC80/30-BP	1.5	30	0.38	6.31	6.19	1.02
	C2F3V3	Monotonic	62.0	3.31	552	225	40.6	Single	RC65/35-BN	1.5	35	0.55	5.57	5.37	1.04
[80]	F1V1MS	Monotonic	55.9	3.31	457.8	184.7	148.8	Single	RC80/30-BP	0.5	30	0.38	3.34	3.55	0.94
	F1V2MS	Monotonic	58.1	3.31	457.8	184.7	54.8	Single	RC80/30-BP	1.0	30	0.38	4.65	3.01	1.55
	F1V3MS	Monotonic	50.9	3.31	457.8	184.7	96.9	Single	RC80/30-BP	1.5	30	0.38	4.93	4.82	1.02
	F2V2MS	Monotonic	52.1	3.31	457.8	184.7	74.0	Single	ZP305	1.0	30	0.55	3.96	3.46	1.15
	F1V1RC	Reversed Cyclic	56.1	3.31	457.8	184.7	126.0	Single	RC80/30-BP	0.5	30	0.38	3.13	3.42	0.92
	F1V2RC	Reversed Cyclic	58.1	3.31	457.8	184.7	81.4	Single	RC80/30-BP	1.0	30	0.38	4.41	2.80	1.58
	F1V3RC	Reversed Cyclic	53.1	3.31	457.8	184.7	90.0	Single	RC80/30-BP	1.5	30	0.38	4.72	4.83	0.98
	F2V2RC	Reversed Cyclic	52.9	3.31	457.8	184.7	115.0	Single	ZP305	1.0	30	0.55	3.47	2.70	1.29
[2]	H1.5PSM	Monotonic	41.56	3.31	520	200	64	Hybrid	RC80/30-BP OL13/.20	0.75 0.75	30 13	0.38 0.21	6.15	6.23	0.98
	H1.5PSC	Reversed Cyclic	55.48	3.31	520	200	63	Hybrid	RC80/30-BP OL13/.20	0.75 0.75	30 13	0.38 0.21	5.75	7.03	0.82
	SL1.5PSC	Reversed Cyclic	61.13	3.31	520	200	67	Single	RC80/30-BP	1.5	30	0.38	5.29	5.65	0.94
	SS1.5PSC	Reversed Cyclic	50.46	3.31	520	200	103	Single	OL13/.20	1.5	13	0.21	4.81	4.60	1.05

Reference	**Specimen ID**	**Loading Type**	**f'_c (MPa)**	**ρ_{sx} (%)**	**f_{yx} (MPa)**	**E_s (GPa)**	**s_m (mm)**	**Fibre Layout**	**Fiber Type**	**V_f (%)**	**l_f (mm)**	**d_f (mm)**	**v_{uexp} (MPa)**	**v_{umodel} (MPa)**	**v_{uexp}/v_{umodel}**
[2]	H1.0PSM	Monotonic	51.34	3.31	520	200	68	Hybrid	RC80/30-BP	0.5	30	0.38	5.02	6.05	0.83
									OL13/.20	0.5	13	0.21			
	H1.0PSC	Reversed Cyclic	51.34	3.31	520	200	71	Hybrid	RC80/30-BP	0.5	30	0.38	4.82	5.94	0.81
									OL13/.20	0.5	13	0.21			
	SL1.0PSC	Reversed Cyclic	57.53	3.31	520	200	74	Single	RC80/30-BP	1.0	30	0.38	4.58	4.55	1.01
	SS1.0PSC	Reversed Cyclic	54.12	3.31	520	200	71	Single	OL13/.20	1.0	13	0.21	4.34	3.97	1.09
	H1.5PSM-Pre-damaged	Monotonic	71.69	3.31	520	200	68	Hybrid	RC80/30-BP	0.75	30	0.38	6.59	7.68	0.86
									OL13/.20	0.75	13	0.21			
	H1.5PSC-Pre-damaged	Reversed Cyclic	71.69	3.31	520	200	71	Hybrid	RC80/30-BP	0.75	30	0.38	5.76	7.68	0.75
									OL13/.20	0.75	13	0.21			
	H0.75PSM	Monotonic	60.97	3.31	520	200	71	Hybrid	RC80/30-BP	0.375	30	0.38	5.27	6.39	0.83
									OL13/.20	0.375	13	0.21			
	H2.0PSM	Monotonic	58.16	3.31	520	200	56	Hybrid	RC80/30-BP	1.0	30	0.38	6.63	5.56	1.19
									OL13/.20	1.0	13	0.21			
[81]	DC-P2	Monotonic	62.1	3.31	466.4	193	43	Single	RC80/30-BP	1.0	30	0.38	5.97	5.12	1.17
	DC-P4	Reversed Cyclic	64.0	3.31	466.4	193	71	Single	RC80/30-BP	1.0	30	0.38	4.47	4.61	0.97
	DC-P3	Monotonic	50.9	3.31	466.4	193	72	Single	MAC Matrix	2.0	54	0.81	3.87	4.49	0.86
	DC-P5	Reversed Cyclic	54.3	3.31	466.4	193	59	Single	MAC Matrix	2.0	54	0.81	3.43	4.73	0.72

Appendix B Verification of the SST model with an experimental data sets for Panels under Compression

Reference	**Specimen ID**	**Experimental Load (P_u)**	**l**	**b**	**t**	**f_c'**	**f_y**	**A_{sh}**	**A_{sv}**	**V_f**	**l_f**	**d_f**	**A_{str}**	**P_{ucal}**
		kN	**mm**	**mm**	**mm**	**MPa**	**MPa**	**mm^2**	**mm^2**	**fraction**	**mm**	**mm**	**mm^2**	**kN**
This Study (Square)	S0-TM1	1649.040	450	450	100	55.500	868	129	71	0	0	0	21213.203	917.4881
	S0-TM2	1611.180	450	450	100	55.500	868	129	71	0	0	0	21213.203	1127.714
	S0-TL1	1348.130	450	450	100	55.500	868	129	71	0	0	0	21213.203	861.5928
	S0-TL2	1702.850	450	450	100	55.500	868	129	71	0	0	0	21213.203	951.0573
	S0-TS1	1572.320	450	450	100	55.500	481	129	71	0	0	0	21213.203	931.0978
	S0-TS2	1411.900	450	450	100	55.500	481	129	71	0	0	0	21213.203	779.1752
	S075-TM1	1774.590	450	450	100	43.500	868	129	71	0.0075	30	0.38	21213.203	1289.459
	S075-TM2	1679.930	450	450	100	43.500	868	129	71	0.0075	30	0.38	21213.203	1295.153
	S075-TL1	1528.480	450	450	100	43.500	868	129	71	0.0075	30	0.38	21213.203	1287.407
	S075-TL2	1478.660	450	450	100	43.500	868	129	71	0.0075	30	0.38	21213.203	1213.337
	S075-TS1	1339.163	450	450	100	43.500	481	129	71	0.0075	30	0.38	21213.203	1430.996
	S075-TS2	1449.760	450	450	100	43.500	481	129	71	0.0075	30	0.38	21213.203	1329.042
This Study (Rectangular)	R0-DL1	2838.724	350	300	150	81.900	841	129	71	0	0	0	21213.203	1125.35
	R0-DL2	2641.102	350	300	150	82.700	841	129	71	0	0	0	21213.203	1187.751

Reference	**Specimen ID**	**Experimental Load (P_u)**	l	b	t	f_c'	f_{yh}	A_{sh}	A_{sv}	V_f	l_f	d_f	A_{str}	P_{ucal}
		kN	**mm**	**mm**	**mm**	**MPa**	**MPa**	**mm^2**	**mm^2**	**fraction**	**mm**	**mm**	**mm^2**	**kN**
This Study (Rectangular)	R0-CL1	3065.678	200	300	150	84.200	841	129	71	0	0	0	21213.203	729.9871
	R0-CL2	2756.082	200	300	150	68.600	841	129	71	0	0	0	21213.203	802.5716
	R0-DH1	2841.099	350	300	150	81.800	848	200	71	0	0	0	21213.203	1229.478
	R0-DH2	2884.884	350	300	150	81.800	848	200	71	0	0	0	21213.203	1229.478
	R075-DL1	3021.465	350	300	150	79.228	841	129	71	0.0075	30	0.38	21213.203	2229.776
	R075-DL2	3049.283	350	300	150	75.936	841	129	71	0.0075	30	0.38	21213.203	2115.757
	R075-CL1	3664.258	200	300	150	78.908	841	129	71	0.0075	30	0.38	21213.203	1421.259
	R075-CL2	3378.531	200	300	150	81.126	841	129	71	0.0075	30	0.38	21213.203	1287.567
	R075-DH1	3010.656	350	300	150	76.609	848	200	71	0.0075	30	0.38	21213.203	1848.162
	R075-DH2	3640.745	350	300	150	78.908	848	200	71	0.0075	30	0.38	21213.203	1934.655
	R150-DL1	3257.755	350	300	150	69.170	841	129	71	0.015	30	0.38	21213.203	2361.785
	R150-DL2	2761.233	350	300	150	62.306	841	129	71	0.015	30	0.38	21213.203	2442.751
	R150-CL1	3260.619	200	300	150	69.565	841	129	71	0.015	30	0.38	21213.203	1675.73
	R150-CL2	3517.491	200	300	150	61.978	841	129	71	0.015	30	0.38	21213.203	1452.296

Reference	**Specimen ID**	**Experimental Load (P_u)**	l	b	t	f_c'	f_{yh}	A_{sh}	A_{sv}	V_f	l_f	d_f	A_{str}	P_{ucal}
		kN	**mm**	**mm**	**mm**	**MPa**	**MPa**	**mm^2**	**mm^2**	**fraction**	**mm**	**mm**	**mm^2**	**kN**
This Study **(Rectangular)**	R150-DH1	2988.729	350	300	150	68.094	848	200	71	0.015	30	0.38	21213.203	2273.714
	R150-DH2	3334.598	350	300	150	69.170	848	200	71	0.015	30	0.38	21213.203	2398.317
Sahoo et al. **(2011)** [59]	N-0.2	357.600	150	150	100	25.400	423	28.27	28.27	0	0	0	7071.06	273.2046
	N-0.4	387.800	150	150	100	26.100	423	28.27	28.27	0	0	0	7071.06	280.7338
	N-0.6	416.300	150	150	100	26.100	423	28.27	28.27	0	0	0	7071.06	280.7338
	N-0.8	411.600	150	150	100	24.000	423	28.27	28.27	0	0	0	7071.06	258.1461
	N-1.0	386.200	150	150	100	24.000	423	28.27	28.27	0	0	0	7071.06	258.1461
	M-0.2	586.200	150	150	100	62.000	423	28.27	28.27	0	0	0	7071.06	543.3206
	M-0.4	724.600	150	150	100	56.000	423	28.27	28.27	0	0	0	7071.06	516.6613
	M-0.6	783.300	150	150	100	63.300	423	28.27	28.27	0	0	0	7071.06	548.9243
	M-0.8	971.200	150	150	100	57.800	423	28.27	28.27	0	0	0	7071.06	524.803
	M-1.0	974.500	150	150	100	57.800	423	28.27	28.27	0	0	0	7071.06	524.803
	H-0.2	847.500	150	150	100	85.700	423	28.27	28.27	0	0	0	7071.06	636.3111
	H-0.4	960.900	150	150	100	83.200	423	28.27	28.27	0	0	0	7071.06	628.4377

Reference	**Specimen ID**	**Experimental Load (P_u)**	l	b	t	f_c'	f_{yh}	A_{sh}	A_{sv}	V_f	l_f	d_f	A_{str}	P_{ucal}
		kN	**mm**	**mm**	**mm**	**MPa**	**MPa**	**mm^2**	**mm^2**	**fraction**	**mm**	**mm**	**mm^2**	**kN**
Sahoo et al. **(2011)** [59]	H-0.6	947.100	150	150	100	83.200	423	28.27	28.27	0	0	0	7071.06	628.4377
	H-0.8	1169.800	150	150	100	83.100	423	28.27	28.27	0	0	0	7071.06	628.0636
	H-1.0	1031.500	150	150	100	83.100	423	28.27	28.27	0	0	0	7071.06	628.0636
	H-1.4	1228.100	150	150	100	74.300	423	28.27	28.27	0	0	0	7071.06	594.2066
Sahoo et al. **(2008)** [12]	PR-1	869.700	300	300	100	28.620	423	78.53	78.53	0	0	0	14142	615.6731
	PR-2	928.300	300	300	100	27.730	423	78.53	78.53	0	0	0	14142	596.5274
	PR-3	1114.000	300	300	100	33.980	423	78.53	78.53	0	0	0	14142	730.9774
	FR-1	978.600	300	300	100	27.460	423	78.53	78.53	0.01	25	0.82	14142	691.5737
	FR-2	1041.000	300	300	100	38.580	423	78.53	78.53	0.01	25	0.82	14142	971.6283
	FR-3	1141.200	300	300	100	39.110	423	78.53	78.53	0.01	25	0.82	14142	984.9763

doi:10.6342/NTU202403952

Appendix C Verification of the SST model with an experimental data sets for RC and SFRC Deep Beams

Reference	**Specimen ID**	***t***	***h***	***a/d***	***a***	**f_c'**	**ρ_l**	**f_{yl}**	**Steel Fibers**			**failure mode**	**V_u**	**1**	**2**	**3**	**4**	**5**
		mm	**mm**		**mm**	**MPa**	**(%)**	**MPa**	**V_f (%)**	**Fiber Type**	**l_f/d_f**		**kN**	**kN**	**kN**	**kN**	**kN**	**kN**
Cho & Kim [52]	F30-0.0-13	120	200	1.43	239.5	34.4	1.32	399	0	–	0	Shear	73	51	60	34	63	51
	F30-0.5-13	120	200	1.43	239.5	25.7	1.32	399	0.5	H	60	Shear	60	67	75	35	73	59
	F60-0.0-13	120	200	1.43	239.5	54.3	1.32	399	0	–	0	Shear	65	61	75	43	79	65
	F70-0.0-19	120	200	1.43	239.5	65.3	2.82	456	0	–	0	Shear	117	99	86	47	87	91
	F70-0.5-19	120	200	1.43	239.5	70.5	2.82	456	0.5	H	60	Shear	178	122	111	58	109	127
	F70-1.0-19	120	200	1.43	239.5	67.3	2.82	456	1	H	60	Shear	169	137	131	66	126	155
	F70-1.5-19	120	200	1.43	239.5	67.3	2.82	456	1.5	H	60	Shear	186	154	153	76	145.	183
	F80-0.0-16	120	200	1.43	239.5	74.1	2	422	0	–	0	Shear	146	85	89	50	93	84
	F80-0.5-16	120	200	1.43	239.5	82.4	2	422	0.5	H	60	Shear	157	109	116	63	117	120
	F80-0.0-19	120	200	1.43	239.5	85.2	2.82	456	0	–	0	Shear	108	108	97	54	99	99
	F80-0.5-19	120	200	1.43	239.5	86.1	2.82	456	0.5	H	60	Shear	153	129	120	65	119	136
Sagi et al. [99]	DB-F0-200	180	500	1.13	500.0	44.5	1.57	535	0	–	0	DS	406	357	348	196	286	365
	DB-SF50-200	180	500	1.13	500.0	42	1.57	535	0.5	H	50	DS	570	423	431	215	340	449
	DB-SF100-200	180	500	1.13	500.0	43.7	1.57	535	1	H	50	DS	607	486	530	244	408	543
	DB-SF150-200	180	500	1.13	500.0	47.6	1.57	535	1.5	H	50	DS	620	552	636	280	482	647
	DB-S0.3-200	180	500	1.13	500.0	42.3	1.57	535	0	–	0	DS	485	352	339	191	279	407
	DB-F0-100	180	500	1.13	500.0	44.5	1.57	535	0	–	0	DS	364	357	348	196	286	319
	DB-SF100-100	180	500	1.13	500.0	43.7	1.57	535	1	H	50	DS	542	486	530	244	481	481
	DB-SF150-100	180	500	1.13	500.0	47.6	1.57	535	1.5	H	50	DS	622	552	636	280	482	572
	DB-S0.3-100	180	500	1.13	500.0	42.3	1.57	535	0	–	0	DS	444	352	339	191	279	448
Wei-Cheng Chen [90]	D32-S075-TU	160	700	1	551.6	79.3	1.85	700	0.75	H	79	Strut Failure	796	818	852	415	587	732
	D32-S075-T300	160	700	1	551.6	79.3	1.85	700	0.75	H	79	Strut Failure	843	818	852	415	587	760
	D32-S075-T150	160	700	1	551.6	79.3	1.85	700	0.75	H	79	Strut Failure	874	818	852	415	587	817
	D32-S150-TU	140	700	1	551.6	82.3	2.12	700	1.5	H	79	Strut Failure	879	901	998	448	663	927
	D32-S150-T300	140	700	1	551.6	82.3	2.12	700	1.5	H	79	Strut Failure	916	901	998.9	448.5	663.6	955.5
	D32-S150-T150	140	700	1	551.6	82.3	2.12	700	1.5	H	79	Strut Failure	1042	901	998.9	448.5	663.6	959.8

doi:10.6342/NTU202403952

Reference	Specimen ID	t	h	a/d	a	f_c'	ρ_l	f_{yl}	Steel Fibers			failure mode	V_u	1	2	3	4	5
		mm	mm		mm	MPa	(%)	MPa	V_f (%)	Fiber Type	l_f/d_f		kN	kN	kN	kN	kN	kN
Kai-Ning Chi [89]	S32-S000-HU	160	700	1	600	69.75	0.85	700	0	–	0	Splitting Failure	474	452.93	575.27	335.13	431.94	427.89
	S32-S000-H100	160	700	1	600	68.08	0.85	700	0	–	0	Strut Failure	626.8	447.54	568.51	331.10	426.74	501.05
	S32-S000-TU	160	700	1	600	69.75	0.85	700	0	–	0	Strut Failure	638	452.93	575.27	335.13	431.94	431.38
Minh & Rovnak [93]	RB1	150	250	1.2	264	52.2	0.3	550	0	–	0	Shear	120	76.57	140.50	83.05	128.45	82.77
	RB2	150	250	1.2	264	52.2	0.3	550	0	–	0	Shear	122	76.57	140.50	83.05	128.45	82.77
	RB3	150	250	1.2	264	52.2	0.3	550	0	–	0	Shear	115	76.57	140.50	83.05	128.45	82.77
	RB4	150	250	1.2	264	52.2	0.3	550	0	–	0	Shear	112	76.57	140.50	83.05	128.45	82.77
	FRB13	150	250	1.2	264	55.8	0.3	550	0.8	H	60	Shear	144	131.54	214.52	108.05	173.47	133.38
	FRB14	150	250	1.2	264	55.8	0.3	550	0.8	H	60	Shear	144	131.54	214.52	108.05	173.47	133.38
	FRB15	150	250	1.2	264	55.8	0.3	550	0.8	H	60	Shear	145	131.54	214.52	108.05	173.47	133.38
	FRB16	150	250	1.2	264	55.8	0.3	550	0.8	H	60	Shear	148	131.54	214.52	108.05	173.47	133.38
	FRB17	150	250	1.2	264	54.6	0.3	550	1.2	SH	60	Shear	149	152.74	247.61	117.86	192.27	123.33
	FRB25	150	250	1.2	264	54.9	0.3	550	1.2	SH	60	Shear	148	153.03	248.00	118.18	192.63	125.25
	FRB26	150	250	1.2	264	54.9	0.3	550	1.2	SH	60	Shear	147	153.03	248.00	118.18	192.63	125.25
	FRB27	150	250	1.2	264	54.9	0.3	550	1.2	SH	60	Shear	150	153.03	248.00	118.18	192.63	125.25
	FRB28	150	250	1.2	264	54.9	0.3	550	1.2	SH	60	Shear	150	153.03	248.00	118.18	192.63	125.25

***Note:**

DS: Diagonal Splitting

SH: Mixture of straight and hooked end steel fibers

H: Hooked end steel fibers